Summer 9-1-2014

Effect of Design Parameters and Intercalation Induced Stresses in Lithium Ion Batteries

Sumitava De
Washington University in St. Louis

WASHINGTON UNIVERSITY IN ST. LOUIS
School of Engineering and Applied Science
Department of Energy, Environmental and Chemical Engineering

Dissertation Examination Committee:
Venkat R. Subramanian, Chair
Richard Axelbaum
Parag Banerjee
Pratim Biswas
Babu Chalamala
Palghat Ramachandran
Godfrey Sikha

Effect of Design Parameters and Intercalation Induced Stresses in Lithium Ion Batteries

by

Sumitava De

A dissertation presented to the
Graduate School of Arts and Sciences
of Washington University in St. Louis
partial fulfillment of the
requirements for the degree of

DOCTOR OF PHILOSOPHY

August 2014
Saint Louis, Missouri

Table of Contents

List of figures

List of tables

Acknowledgments

I would like to express my sincere gratitude and appreciation to everyone who helped me throughout these years and made this dissertation possible. I am especially grateful to my advisor, Dr. Venkat Subramanian for giving me the opportunity to be a part of his research group and for his guidance, wisdom and patient support, which helped me develop myself as a critical thinker and nurtured my passion for research. I have benefited immensely from various discussions and interactions with him and I thank him for his encouragement and advice and for supporting my abilities throughout my stay here.

I would like to thank my committee members Dr. Pratim Biswas, Dr. Richard Axelbaum, Dr. Parag Banerjee, Dr. Godfrey Sikha and Dr. Babu Chalamala for their valuable suggestions, critical comments and support during different stages of work throughout my PhD. I would like to specially thank Dr. Godfrey Sikha and Dr. Joseph Gordon for being my mentors during my internship at Applied Materials Inc. and for guiding me through my first exposure to corporate culture.

I acknowledge the financial support provided by National Reconnaissance Office and United States Department of Energy Arpa-E and Washington University in St. Louis for performing various tasks in this work.

I am grateful to all the members and alumni of the M.A.P.L.E. group and my colleagues at the EECE department. A special thanks to Venkat Ramadesigan, Paul Northrop, Bharat Suthar, Matt Lawder, Miklos Lengyel, Craig Jacobsen, Jake Meyer, Ray Henson, Dhruv Mitroo, Mike Walker and all my other friends in the EECE Department. Their outstanding work ethics motivated me to

move forward in all my endeavors. I would like to thank all the department staff for their administrative assistance.

My very special thanks to my parents and my relatives whom I owe everything I am today. Without their support, this work would not have been possible. I am extremely grateful and express my deepest gratitude and love to them.

Sumitava De

Washington University in St. Louis
June 2014

ABSTRACT OF THE DISSERTATION

Effect of design parameters and intercalation induced stresses in lithium ion batteries

by

Sumitava De

Doctor of Philosophy in Energy, Environmental and Chemical Engineering

Washington University in St. Louis, 2014

Dr. Venkat R. Subramanian, Chair

Electrochemical power sources, especially lithium ion batteries have become major players in various industrial sectors, with applications ranging from low power/energy demands to high power/energy requirements. But there are some significant issues existing for lithium ion systems which include underutilization, stress-induced material damage, capacity fade, and the potential for thermal runaway. Therefore, better design, operation and control of lithium ion batteries are essential to meet the growing demands of energy storage. Physics based modeling and simulation methods provide the best and most accurate approach for addressing such issues for lithium ion battery systems. This work tries to understand and address some of these issues, by development of physics based models and efficient simulation of such models for battery design and real time control purposes.

This thesis will introduce a model-based procedure for simultaneous optimization of design parameters for porous electrodes that are commonly used in lithium ion systems. The approach simultaneously optimizes the battery design variables of electrode porosities and thickness for maximization of the energy drawn for an applied current, cut-off voltage, and total time of discharge. The results show reasonable improvement in the specific energy drawn from the lithium ion battery when the design parameters are simultaneously optimized.

The second part of this dissertation will develop a 2-dimensional transient numerical model used to simulate the electrochemical lithium insertion in a silicon nanowire (Si NW) electrode. The model geometry is a cylindrical Si NW electrode anchored to a copper current collector (Cu CC) substrate. The model solves for diffusion of lithium in Si NW, stress generation in the Si NW due to chemical and elastic strain, stress generation in the Cu CC due to elastic strain, and volume expansion in the Si NW and Cu CC geometries. The evolution of stress components, i.e., radial, axial and tangential stresses in different regions in the Si NW are studied in details.

Lithium-ion batteries are typically modeled using porous electrode theory coupled with various transport and reaction mechanisms with an appropriate discretization or approximation for the solid phase diffusion within the electrode particle. One of the major difficulties in simulating Li-ion battery models is the need for simulating solid-phase diffusion in the second radial dimension r within the particle. It increases the complexity of the model as well as the computation time/cost to a great extent. This is particularly true for the inclusion of pressure induced diffusion inside particles experiencing volume change. Therefore, to address such issues, part of the work will involve development of efficient methods for particle/solid phase reformulation – (1) parabolic profile approach and (2) a mixed order finite difference method. These models will be used for approximating/representing solid-phase concentration variations within the active material. Efficiency in simulation of particle level models can be of great advantage when these are coupled with macro-homogenous cell sandwich level battery models.

Chapter 1

Introduction

1.1 Electrochemical energy storage

Energy is an important issue for mankind. In recent years, there has been a resurgence of interest in developing new clean and renewable energy systems primarily due to concerns about human's environmental footprint, such as that due to carbon dioxide, and concerns about security and rapid global development. Significant development has been made in renewable energy technologies like wind, solar, etc. With these, comes the need for developing state of the art energy storage devices.

Electrochemical energy storage devices such as lithium ion batteries, redox flow batteries, fuel cells, electrochemical capacitors have been identified as the leading EES technologies as a result of their scalability and versatility. Fig 1-1[1] shows the power and energy density features of the above mentioned devices. Capacitors are more suitable for high power applications because of their high power densities and sub-second response times. Batteries and fuel cells/redox flow batteries have large energy densities which make them suitable for large scale energy storage like electrical grids.

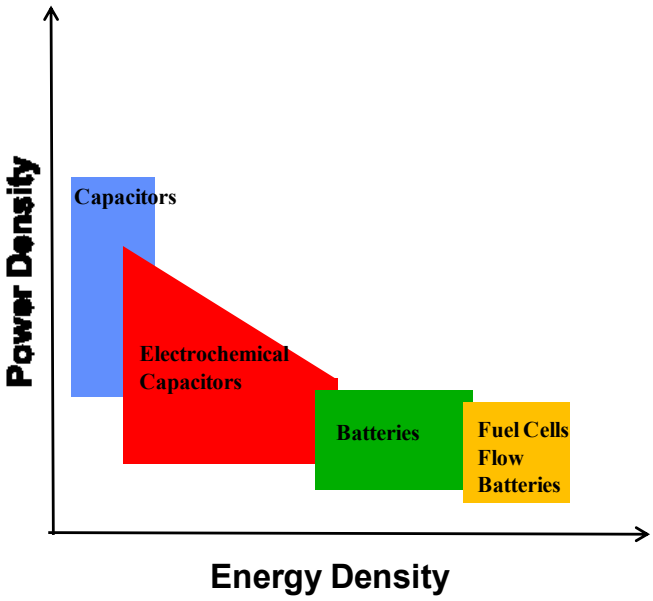

Fig. 1-1. Energy and power densities of various EES systems

1.2 Lithium-ion battery

Due to their high theoretical and practical energy density, lithium-ion batteries are attractive power sources for portable consumer electronic applications, Plug-in Hybrid Electric Vehicles (PHEVs) and Electric Vehicles (EVs). Lithium-ion battery is a type of rechargeable battery which has four primary components namely a lithium metal oxide positive electrode (cathode), a graphite/silicon negative electrode (anode), a porous polymer separator and an organic electrolyte. The separator separates the positive and negative electrodes while allowing ions to pass through. The anode, cathode and the separator are submerged in the electrolyte solution. In a lithium battery, Li ions migrate repeatedly between the anode and cathode. During charging, ions of lithium move through the electrolyte from the cathode to the anode while the electrons flow through the external circuit. The reverse phenomenon occurs while discharging. Fig. 1-2 [2] shows a pictorial representation of lithium-ion battery cell sandwich architecture and the phenomena taking place during its operation.

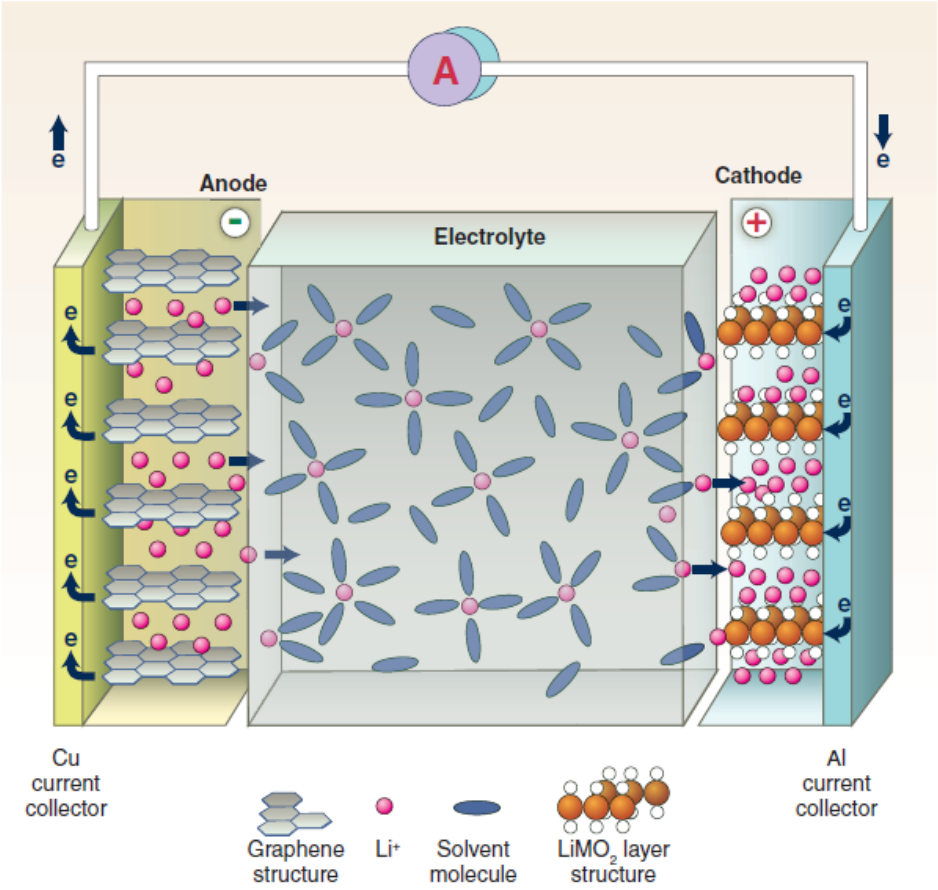

Fig. 1-2. A schematic representation of a lithium-ion battery

The intercalation/de-intercalation reaction is the most important reaction mechanism for Li-ion rechargeable batteries, and involves the insertion of Li ions into interstitial sites in the crystal without changing the basic crystal structure.

1.3 System engineering approach to address issues

Significant issues persist with existing lithium-ion battery technology including underutilization, stress-induced material damage, capacity fade, and the potential for thermal runaway [3]. Current issues with lithium-ion batteries can be broadly classified at three different levels i.e. market level, system level, and single cell sandwich. At the market level, factors such as cost, safety, and

life become most important as the consumers are the major target. At the system level, issues such as cell underutilization, capacity fade, thermal runaways, and lower energy density are most critical. These issues can be examined and understood more fundamentally at the cell sandwich level, by studying phenomena occurring at the electrodes, electrolyte, separator, and their interfaces more critically. These shortcomings are generally attributed to major issues associated with Solid-Electrolyte Interface (SEI)-layer growth, unwanted side reactions, mechanical degradation, loss of active materials, and the increase of various internal resistances such as ohmic and mass transfer resistance. Application of modeling, simulation, and systems engineering techniques is a viable option to address these issues at the cell sandwich level to enhance system level performance to improve commercial marketability.

Fundamental modeling approaches coupled with systems engineering techniques can provide a set of powerful tools for better design, creation, and operation of lithium-ion battery systems. The development of new materials (including choice of molecular constituents and material nano- and macro-scale structure), electrolytes, binders, and electrode architecture are likely to contribute towards improving the performance of batteries. For a given chemistry, better fundamental understanding along with systems engineering approach can be used to optimize the electrode architecture, operational strategies, cycle life, and device performance by maximizing the efficiency and minimizing the potential problems usually observed in batteries.

The schematic in Fig. 1-3 shows four systems engineering tasks and the interactions between these tasks. Ideally, the eventual goal of this approach applied to Li-ion batteries would develop a detailed multiscale and multiphysics model formulated so that its equations can be simulated in the most efficient manner and platform, which would be employed in robust optimal design or control.

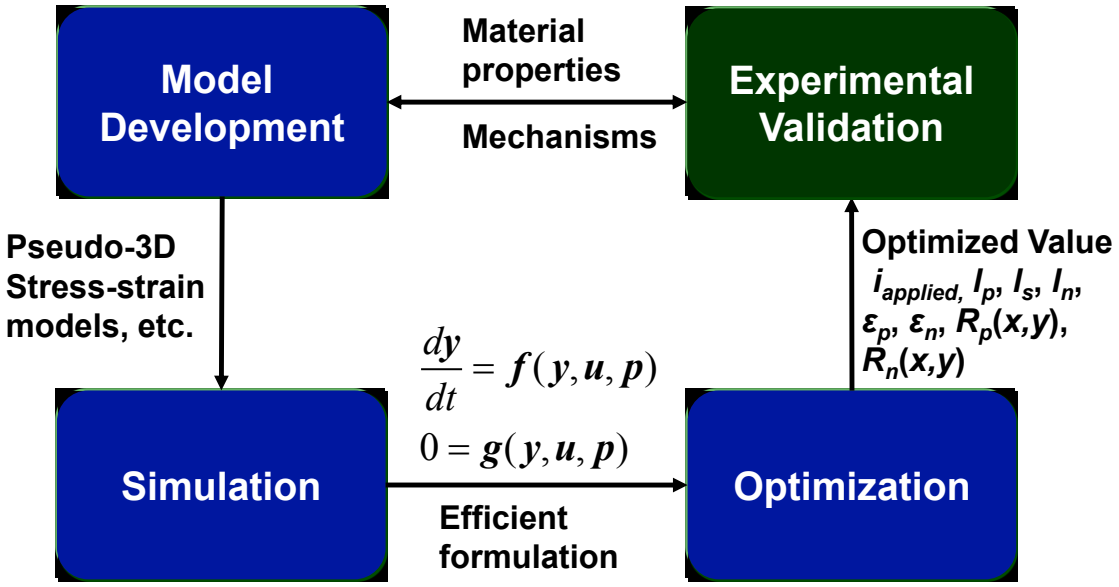

Fig. 1-3. Schematic of system engineering tasks and the interplay between them : In the figure, u, y and p are vectors of algebraic variables, differential variables and design parameters respectively

Fundamental model development coupled with other systems engineering approaches can address a wide range of issues in batteries such as:

1. Understanding degradation mechanisms in lithium-ion batteries

2. Capacity fade modeling

3. Improved life by changing operating conditions and material properties

4. Improved energy density/power density by manipulating design parameters and operating protocols

5. Model predictive control that incorporates real-time estimation of State-of-Charge (SOC) and State-of-Health (SOH).

1.4 Modeling of lithium-ion batteries

Model development is the core of the systems engineering approach for developing real time control strategies and achieving optimal design of batteries. Generally, the cost of developing a detailed multiscale/multiphysics model with high predictive capability is computationally very expensive, so model development efforts start with a simple model and then add complexity/additional physics until the model predictions are sufficiently accurate to address the objectives. Another important task after development of model is to experimentally validate it to ensure that the model predicts the experimental data to the required precision with a reasonable confidence. However, for a lithium-ion battery, most variables in the system are not directly measurable during charge-discharge cycles, and hence are not available for comparison, to verify the accuracy of the assumptions made in the derivation of the model. Also, model parameters that cannot be directly measured experimentally typically have to be obtained by comparing the experimental data with the model predictions.

Mathematical models for lithium-ion batteries vary widely in terms of complexity, computational efficiency, and accuracy of their predictions. Fig. 1-4[4] shows a comparison of the lithium ion battery models reported in literature with respect to their predictability and computational cost. As obvious, inclusion of additional physics in an existing battery model improves its predictions but also increases computational costs which are not useful for real time control and optimization purposes. Therefore, use of simplified or complicated battery models is driven by the particular needs of the application. Lithium ion battery models can be roughly classified into four groups: empirical models, electrochemical models, multiphysics models and molecular/atomic models.

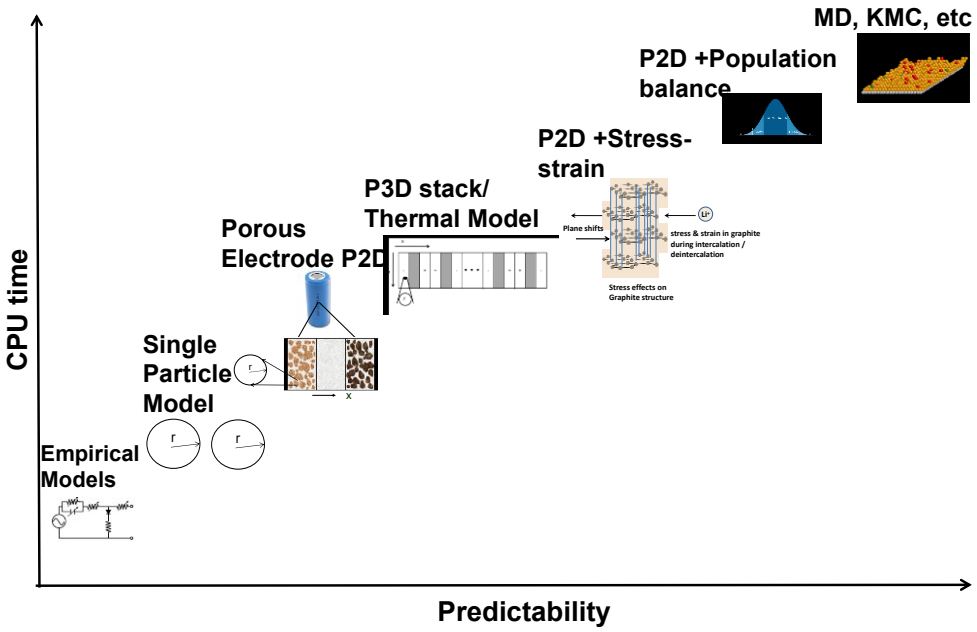

Fig. 1-4. Comparison of lithium-ion battery models (images taken from various sources on the internet and literature)

Empirical models – These models are computationally most efficient as past experimental data is used to predict future behavior of lithium-ion batteries. Empirical models consist of polynomial, exponential, power law, logarithmic, and trigonometric functions and they completely ignore physico-chemical principles. Such battery models are also useless for the design of new battery chemistries or materials. Moreover, as these models are developed by fitting experimental data for specific operating conditions, very low accuracy is expected when empirical models are used for a different set of operating conditions.

Electrochemical engineering models – Continuum scale models which couple chemical/electrochemical kinetics with transport phenomena to predict battery behavior fall under this category. They are more accurate in predictions compared to empirical models.

The single particle model (SPM), developed by Zhang et al. [5], approximates the anode and cathode of the cell sandwich each as a single particle with the same surface area as the electrode. In this model, diffusion and intercalation are considered within the particle i.e. it solves for mass and charge balance in solid phase. Concentration and potential effects in the solution phase between the particles are neglected. On the computational cost scale, this model is on the lower side but it is valid for limited conditions such as low rates, thin electrodes as a result of its assumptions.

Ohmic porous-electrode model [6-9] represents the next level of complexity in this category of lithium ion battery models. It incorporates solid and electrolyte phase potentials and current but neglects the spatial variations in concentration. Either linear, Tafel or exponential kinetics are chosen to represent electrochemical reactions in this model. Furthermore, mass and charge transport parameters like diffusivities, conductivities etc. are varied as functions of porosity of electrodes.

The pseudo two dimensional or P2D model [10] is by far the most widely used model in battery literature. It has been shown to be very accurate for a wide range of operating conditions and has been experimentally validated for high/low rates of charge and discharge. Doyle et al. [10] developed the P2D model based on concentrated solution theory capturing the internal behavior of a lithium-ion cell sandwich consisting of positive and negative porous electrodes, a separator, and current collectors. P2D model solves for both the electrolyte and solid-state mass and charge balances within the porous electrodes and the electrolyte concentration and electrolyte potential within the separator. This model, based on the principles of transport phenomena, electrochemistry, and thermodynamics is represented by coupled nonlinear partial differential

equations (PDEs) in x, r, and t that can take seconds to minutes to simulate. Although, this model provides excellent predictive capability, this has a greater computational cost.

Multiphysics models – Multiscale and multiphysics models are necessary to understand complicated physics occurring during lithium-ion battery operation especially for applications demanding high power/energy. Thermal models include temperature effects into the P2D model which adds complexity to the model but increases its predictability. To overcome the additional computational load, many researchers solve for a global energy balance by decoupling the thermal model from the electrochemical model [11-15]. One major limitation of this decoupling technique is the inability to monitor local current densities and state of charge which affect thermal gradients inside the cell. Global energy balance is only valid for uniform reaction distribution within the cell. Moreover, these models cannot be employed to understand effects on cell performance as a result of temperature changes. Some papers have presented 2D thermal-electrochemical coupled models for lithium-ion cells to understand the effects of local heat generation [16,17]. Recently, researchers have begun developing 3D thermal- electrochemical models for better understanding of the dynamic operation and control of lithium-ion batteries for large-scale applications. As these models are computationally expensive, several approximations are usually made, resulting in various shortcomings. Some models cannot monitor the thermal effect of electrochemical parameters [14,18], while other models require empirical input from experiments or other simulations [19,20]. A Multi-Scale Multi-Dimensional (MSMD) model [21] and a model derived from a grid of 1D electrochemical/thermal models [22] have also been implemented for 3D thermal simulation of batteries.

Lithium intercalation/de-intercalation into the electrode particles during charge/discharge of battery causes expansion/contraction of the active material and this develops stresses which can

result in fracture of particles finally leading to reduction in battery capacity due to loss of active material. Moreover, the pressure gradients inside the particles dictate concentration profiles. Therefore, multiphysics models are needed to be developed which capture the pressure induced diffusion and stress generation in active material particles in lithium-ion batteries. Detailed literature review of such models has been presented in a later chapter.

In general, porous materials rarely have uniform particle size and shape. During cycling, active material particles de-laminate form substrate or agglomerate to form larger sized particles. Therefore to capture effect of particle size distribution on battery performance, researchers have reported the development of continuum models in literature [23,24]. To capture the effect of morphology within battery active material, mesoscale models [25] have been developed which enable materials degradation due to spatially-varying and time-varying changes in the particle size and shape distribution to be explicitly addressed.

Molecular/Atomistic models –Such models are required to understand phenomena occurring at the lattice/molecular scale during operation of lithium-ion battery. The Kinetic Monte Carlo (KMC) method is a stochastic technique that has been employed to study diffusion of lithium between lattice sites within an electrode particle including the effect of crystal structures on mobility of ions etc. [26,27] . The growth of passive solid electrolyte interface (SEI) layer on the surface of anode particles have been studied extensively with KMC methods which has identified as one of the major causes behind capacity fade of batteries [28] .

Molecular dynamics (MD) techniques have been employed to gain insight into the mechanisms of SEI layer growth especially at the start of lithiation (like the first tens of picoseconds) [29]. MD methods have been extensively used for simulation of effective diffusivities [30] . Density functional theory (DFT) simulations have been also used for detailed study and understanding of

several phenomena occurring during battery operations such as structural changes in particles during repetitive cycling [31], stability of organic electrolytes crucial for SEI layer growth [32] etc.

1.5 Simulation of lithium-ion battery models

Battery models can be simulated using multiple numerical methods. Simple empirical models can be solved analytically. Non-linearities in such models can be handled with analytical series solutions using perturbation approaches [33]. Single particle (SPM) models can have analytical solutions for some special cases. Analytical solutions do not exist for models beyond single particle and ohmic resistance models. Finite difference method has been typically employed for solution of P2D model [10]. For example, a P2D model with polynomial approximation [34] for the solid phase diffusion, when discretized with 50 node points in the spatial direction for each variable, results in a system of 250 DAEs for each electrode and 100 DAEs for the separator. Thus, the total number of DAEs to be solved for the P2D model across the entire cell is 250 + 250 + 100 = 600 DAEs. Adding thermal effects to the model increase the number of DAEs to be solved. Stack models become extremely computationally heavy, as they introduce N times the number of equations coming from a cell sandwich where N corresponds to the number of cells in the stack.

In general, adding complicated physics to the lithium ion battery models increase their accuracy and predictability but increases the computational load which is not favorable for real time control and optimization purposes. Therefore, there is a need for developing faster computationally efficient but accurate models. Model reformulation and model reduction techniques have been reported in literature for efficient battery models. Methods such as proper orthogonal decomposition (POD), Galerkin based approaches, orthogonal collocation etc. have

all been employed for of fast efficient lithium-ion battery simulations [35-37]. These techniques will be discussed in details in a later chapter.

1.6 Optimization applied to lithium ion batteries

Optimization of design parameters is an essential step towards achieving better utilization and safer operation of batteries, especially for high power and energy demanding applications. Battery design parameters such as cell thickness and electrode porosity and operating profiles can be optimized using the same numerical algorithms, for objectives such as maximization of performance (e.g., energy density, life) or minimization of capacity fade and mechanical degradation. These optimization problems are solved subject to the model equations and any physical constraints. The optimal estimation of unmeasured states in lithium-ion batteries can also be formulated in terms of a constrained model-based optimization.

Design Parameters	Minimum Detail of Model Required
l_p (Thickness of cathode)	Pseudo 2D
l_n (Thickness of anode)	Pseudo 2D
ε_p (Porosity of cathode)	Pseudo 2D
ε_n (Porosity of anode)	Pseudo 2D
$\varepsilon_{f,p}$ (Porosity of cathode filler)	Pseudo 2D
$\varepsilon_{f,n}$ (Porosity of anode filler)	Pseudo 2D
l_s (Thickness of separator)	Pseudo 2D
R_p (Radii of cathode particle)	Pseudo 2D with stress-strain effects
R_n (Radii of anode particle)	Pseudo 2D with stress-strain effects
l_{cc} (Thickness of current collectors)	Pseudo 2D with thermal
H (Height of cell)	2D / 2D with thermal
Tab Positions	2D / 2D with thermal
Initial Electrolyte Concentration	Pseudo 2D

Table 1-1. List of possible design parameters for lithium ion batteries

All the parameters reported in Table 1-1 cannot be optimized independently and optimizing all parameters may not be significant towards the improvement of performance. Nevertheless, the table presents a list of all possible design parameters. Model based design has been reported in literature for some of the parameters and limited situations. . A detailed literature review of all battery architecture optimization studies attempted will be presented in a later chapter [38]. One consideration in battery optimization is the computational cost of simulating these types of

battery models. Therefore, as explained earlier it is necessary to develop efficient but accurate battery models.

1.7 Capacity fade for lithium-ion batteries

The capacity of lithium-ion battery decreases overtime with repetitive cycling. This is one of major drawbacks in lithium-ion battery systems which ultimately increase operational costs of such systems. There are several factors which can lead to capacity fade in lithium ion batteries. Some of the processes include lithium deposition due to overcharge conditions, electrolyte decomposition, dissolution of active material, sharp phase boundaries in phase changing active materials, passive SEI layer formation over electrode surfaces etc. [39]. Mechanical degradation of active material is another major cause of capacity fade as it causes breakup of particles, delamination etc. which finally lead to loss in capacity. Fracture and delamination of active material is caused by stress development in particles due to lithium intercalation/deintercalation. Fig. 1-5 [40] shows the buildup of stresses layer by layer of a spherical particle when lithium is inserted during charging. At the beginning of lithium insertion, the outer shell expands creating a strain differential between the lithium rich outer layers and the lithium deficient inner layers of the particle. This strain differential gives rise to stress within the particle.

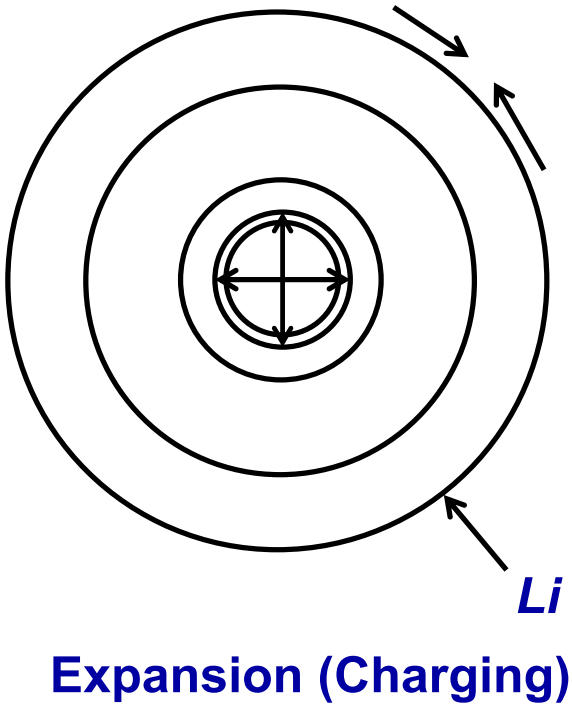

Fig. 1-5. Schematic of particle expansion during lithium insertion (charging)

Studies have shown that especially for high energy capacity materials like silicon, germanium etc., bulk electrodes are not the most feasible option as repeated cycling causes huge stress development leading to volume expansion which finally results in fracture and loss of active materials resulting in capacity loss. Fig. 1-6 shows a pictorial representation of bulk electrode materials before and after repeated cycling. Therefore use of nanostructured materials have been suggested for high energy density anodes for lithium ion batteries. In a thin film configuration, the substrate effect is felt throughout the film and therefore very high stresses are developed. As for a 1 D nanostructure like nanowire, the aspect ratio being very high, the substrate effects are only experienced close to the interface. Moreover, these structures provide other advantages like efficient electron transport, good current collector contact as they are directly grown on them and also aid in reducing dead weight as materials like binders are not used in such architecture.

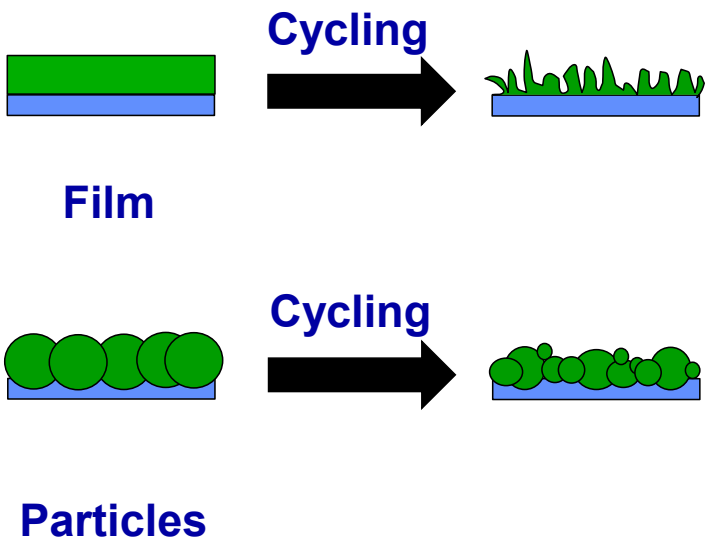

Fig. 1-6. Mechanical degradation of bulk electrode material after cycling

Extensive modeling and simulation studies are required to understand stress development in such nanostructures and decide on the best configuration for use as anodes in lithium ion batteries.

1.8 Research objectives

The objective of this dissertation is to develop modeling and simulation approaches to understand fundamental issues related to lithium ion batteries on one hand and use those approaches for system level studies like real time control during battery operation and optimal design of battery architecture. Chapter 2 will discuss about a method for simultaneous optimization of battery design parameters for improved performance. Chapter 3 shows the detailed development of a 2 D axisymmetric model to understand stress development due to lithium insertion during charging for a silicon nanowire. Efficient reformulation of solid phase pressure induced diffusion problem for fast computation enabling real time control and optimization studies is presented in chapter 4.

Chapter 2

Model-based simultaneous optimization of multiple design parameters for lithium-ion batteries for maximization of energy density

2.1 Introduction

Electrochemical power sources have been identified as major players in sectors like automobiles, power storage, military, and space applications. Lithium-ion batteries, in particular, have a wide range of applications ranging from low power/low energy applications such as implantable cardiovascular defibrillators (ICDs) to high power/high energy applications such as hybrid cars and power grids. This paper considers the simultaneous optimization of battery design parameters such as the thickness of the electrodes and porosity of the materials to maximize the specific energy of the battery to meet the needs of future applications.

Although mathematical modeling of lithium-ion batteries is still considered challenging, major contributions have been made in this field. Doyle et al. [10] developed a first-principles model based on concentrated solution theory for a lithium-ion sandwich consisting of a porous electrode, separator, and current collectors. This is the most widely used physics based model in the battery literature giving accurate predictions even for high rates of charge and discharge and has been used previously for optimization purposes [41-44].

Models for lithium-ion batteries were further developed [4,45-55], with several literature reviews available [4,53-55]. Transport phenomena models are most suitable for the design of batteries due to their ability to provide accurate predictions of the internal and external behavior at the system level. These models are based on porous electrode theory coupled with transport phenomena and electrochemical reaction engineering [10,45-53,56]. One consideration in battery optimization is the computational cost of simulating these types of battery models. Circuit-based empirical battery models are convenient due to their low computational costs but have the tendency to fail at many operating conditions and can produce inaccurate predictions [57,58]. These considerations have motivated the application of model reduction methods to porous electrode theory models. Proper orthogonal decomposition has been applied to the full numerical solution of a lithium-ion battery model to fit a reduced set of eigenvalues and nodes to obtain a lower order approximate solution [35]. An alternative approach is model reformulation of lithium-ion battery porous electrode theory models to increase the computational efficiency without losing accuracy. Previously, Subramanian et al. [36] reformulated the widely used isothermal pseudo-2D porous electrode model for galvanostatic boundary conditions. That model and approach provided for simulating battery models in milliseconds without sacrificing accuracy, but had difficulties when nonlinear properties and thermal effects were considered. Northrop et al. [37] presented a coordinate transformation combined with an orthogonal collocation based reformulation for the simulation of lithium-ion battery operation. This reformulation [37] is designed to be computationally efficient while maintaining the fidelity of the porous electrode theory model even for high rates of charge and discharge. Forman et. al. [59] developed a reduced order electrochemistry based battery model which has sufficient speed and fidelity to enable design, optimization and control. Newman and others have reported

methods to obtain optimal values of design parameters such as electrode thickness [8,9,41-44] . Newman [8] describes the use of a reaction zone model for fast electrode kinetics to optimize for electrode thickness and porosity. Although these studies have the advantage of having analytical solutions, they have some limitations and do not include all the physics of the original models. Newman and his co-workers report the use of Ragone plots for studies on the optimization of battery design parameters [41-44]. By changing one design parameter, such as the electrode thickness, at a time and keeping other parameters constant, Ragone plots for different configurations can be obtained. Hundreds of simulations are required when the applied current is varied to generate a single curve in a Ragone plot, which is tedious and has many computational constraints. Previous work by Ramadesigan et al. [9] optimized the porosity distribution by minimizing ohmic resistance of a porous electrode, as a proof of concept.

Golmon et al. [60] attempted a multiscale design optimization for improving electrochemical and mechanical performance of the battery by manipulating both micro- and macro-scale design variables such as local porosities, particle radii and electrode thickness to minimize internal stresses and maximize the capacity of the battery. A surrogate-based framework using global sensitivity analysis has been used to optimize electrode properties [61].

To our knowledge, simultaneous optimization of multiple battery design parameters using first-principles physics-based models have not been reported in the literature due to high computational expense coupled with the need to perform numerous simulations during the optimization. The objective of this study is to simultaneously optimize battery design parameters (i.e., electrode thickness, porosity of active materials) to maximize the specific energy obtained from the battery. A robust optimization routine is implemented that employs the reformulated model developed by Northrop et al. [37] in order to take advantage of its computational

efficiency. The continuous need for improving the performance of electrochemical power sources motivates the investigation of robust optimization of battery design and operating conditions.

2.2 Optimization and design considerations

The integral of the instantaneous power delivered over the time of discharge of the battery gives the specific energy E in J kg^{-1} [41]

$$E = \frac{1}{M}\int_0^{t_d} V i_{app}\, dt \tag{2.1}$$

which is dependent on the applied current (input) and potential (output, that change with time). Simulations were run ranging from 0.1 C to 6 C (relative to the base parameters) for a discharge cut-off potential of 2.8 V and the values of E were calculated and maximized. The mass per unit area of cell M in units of kg m^{-2} is defined by the following equation Eq. (2.2)

$$M = \rho_p l_p (1-\varepsilon_p-\varepsilon_{f,p}) + \rho_n l_n (1-\varepsilon_n-\varepsilon_{f,n}) + \rho_e (l_p\varepsilon_p + l_s + l_n\varepsilon_n) + \rho_f (l_p\varepsilon_{f,p} + l_n\varepsilon_{f,n}) \tag{2.2}$$

which includes composite electrodes and separator, but not current collectors or residual masses. As M is a function of the electrode thicknesses l_p and l_n and porosities ε_p and ε_n, specific energy depends on these design parameters. There is a scope for optimization of these design parameters to maximize the specific energy drawn from the battery for a desired value applied current and cut-off potential (in other words, for a specific application). Particle radius although being an important design parameter was neglected here. If this model was used for optimization of particle radius, it would have predicted the smallest particle radius to minimize diffusion limitations across the particle. Other problems related to small particle size exist like more

solvent reduction and oxidation, particularly on the first cycle and difficulty in achieving current efficiency of more than 0.9999 for 5000 deep discharge cycles. As our model is not designed to capture these phenomena, the exclusion of particle size from the optimized parameters list can still be justified. Generally, electrolyte is added in bulk as it just acts as an excess source for Li ions and a conducting medium for the ions from one electrode to other, hence, electrolyte concentration may not be a design variable. When optimization tests were run, it was found that for any concentration >0.5M, there was no significant limitation arising from concentration limitations. However, this can change for a different cell, chemistry or an electrolyte. The cross-sectional area of the cell could be included as an additional optimization parameter and would likely provide very interesting results. However, for simplicity we decided to limit our analysis it thickness and porosity of the electrodes. Optimization of width was beyond the scope, and the height and width of electrodes are kept constant. This is done to keep the number of optimized variables manageable.

A general formulation for the optimization of a system is

$$\begin{aligned} &\min_{z(x),u(x),p} \Phi \\ &s.t. \quad \frac{dz}{dx} = f(z(x),y(x),u(x),p), \; f(z(0)) = 0, \quad g(z(1)) = 0 \\ &g(z(x),y(x),u(x),p) = 0, \\ &u_L \le u(x) \le u_U, \qquad y_L \le y(x) \le y_U, \qquad z_L \le z(x) \le z_U \end{aligned} \tag{2.3}$$

where Φ is the dependent variable being optimized, z(x) is the vector of differential state variables, y(x) is the vector of algebraic variables, u(x) is the vector of control variables, and p is the vector of parameters. The control vector parameterization (CVP) [62] is a widely applied method employed in this study, due to its ease of implementation. This parameterization approximates the infinite-dimensional optimal control problem (3) by a finite-dimensional

optimization. Different optimization formulations are possible depending on how the gradient of the resulting nonlinear program is calculated; the computational efficiency of CVP can be increased by incorporating parameter sensitivities. While there have been advances in recent years in the field of dynamic and global optimization [63], these algorithms are still too computationally expensive to be used for applications such as electrochemical systems, which are usually highly stiff in nature with highly nonlinear kinetics requiring adaptive time-stepping, stiff solvers, etc. It is not expected that the simultaneous simulation-optimization approach [62], which fixes the time or independent variable discretization *a priori* will be computationally efficient for most lithium-ion battery applications.

The adopted procedure employs an efficient mathematical reformulation of the pseudo-2D battery model [36,37] that is much more computationally efficient than using a full-order finite-difference model and is a viable candidate to be used for the optimization of electrode design parameters. This model ignores stress and capacity fade mechanisms. It neglects micro-structural effects and the pseudo continuum model is assumed to be valid at the range of design parameters.

The model simulation with base parameters was performed for the specified cut-off voltage to obtain the base discharge time, which was later used to implement a time constraint in the optimization procedure. Numerical algorithms for optimization can get stuck in local optima, which can be nontrivial to troubleshoot when the number of optimization parameters is large. This problem can at least be partly addressed using a sequential step-by-step approach. The steps below show the procedure of advancing from one parameter to four parameter optimization by using the optimized results from previous step as the initial conditions in the next step which facilitate rapid convergence and achievement of global maxima. The model was simulated with

the optimized parameters to compare the electrochemical behavior with the base case. This entire optimization protocol is shown graphically in Fig. 2-1, and can be summarized in the following steps:

1. Choose a battery model that can predict the optimization objective and is sensitive to the manipulated variables (e.g., a P2D model)
2. Develop a reformulation or reduce the order of the model for efficient simulation. This model should be valid in the range of manipulated variables for optimization.
3. Simulate model obtained in step (2) with the base parameters to obtain the time constraint for optimization.
4. Maximize specific energy by optimizing the first chosen parameter i.e. l_p providing the base parameter value as the initial guess.
5. Simulate model obtained in step (2) with the optimized parameter to check whether the time constraint is satisfied or not and to compare the electrochemical performance with the base parameters.
6. Using the solution from step (4) for l_p and base value for porosity ε_p , as the initial guesses maximize specific energy by optimizing the two parameters simultaneously.
7. Repeat step (5) with the optimized parameters.
8. Add the other variables to be optimized one by one following steps similar to (6) and (7) and finally reach optimal performance with multiple optimized parameters.

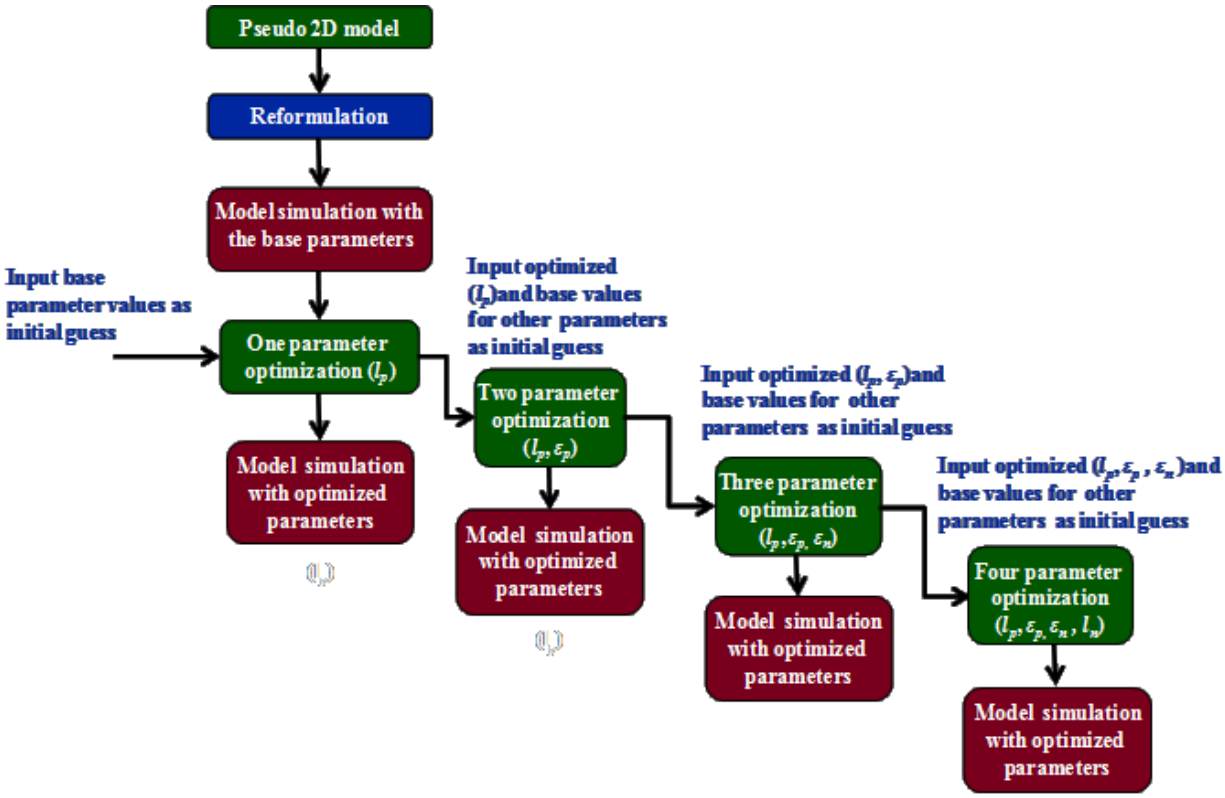

Fig. 2-1. Steps for evaluation of the importance of and simultaneous optimization of electrode design variables

Although not described in detail in many textbooks, such approaches that optimize the most sensitive parameters first and then move on to less sensitive parameters are commonly applied in practice as a way to accelerate convergence. Our objective for using this procedure, however, was different. We were interested in knowing whether the potential benefits of optimizing the thickness of a positive electrode would be limited if the porosities were fixed. The model was simulated with the optimized parameters to compare the electrochemical behavior with the base case. The parameters were optimized within respective bounds to ensure against model failure due to prediction of physically unacceptable optimized parameter values. Note that battery models often fail due to difficulties finding consistent initial conditions, which were handled by using robust initialization procedures described elsewhere [64]. The model is likely to break

down for very small particle radius or very large particle radius, poor conductivity of solid phase material, and other extreme situations, but validity of the continuum model is the beyond the scope of this paper. Simulation was performed with the reformulated model [37] using the *dsolve* solver in Maple®, multivariable optimization with Maple's *globalsolve* function (Global Optimization Toolbox), and *fmincon* in Matlab®. The protocol in Figure 1 consistently converged to the same optima found using the more computationally expensive software platforms. The optimization involved optimizing for a fixed rate (say 2 C) with the nonlinear constraint so that the performance was not compromised at lower rates (1 C).

Simulations were first run for different values of applied current and a specific cut-off potential with the base parameters for the thickness and porosities of electrodes to determine the total discharge time t_{d0} for the battery. The applied currents were varied from 0.1 C to 6 C rates. The value for a 1 C rate was found using the applied current for which the total time of discharge was 1 hour for the base parameters. Table 2-1 shows the applied discharge currents for which optimization was performed as well as the total discharge time for each rate.

Applied Current Density (A/m^2)	**Discharge Time (s)**
2.89875	36,478
14.49375	7274
28.9875	3600
43.48125	2189
57.975	1318
72.46875	852
86.9625	592
115.95	329
144.9375	204
173.925	136

Table 2-1. Applied discharge currents and total discharge times

The obtained energy decreases gradually with increase in i_{app}, the applied current density, which is expected because mass transport and kinetic limitations increase the internal resistance of the cell.

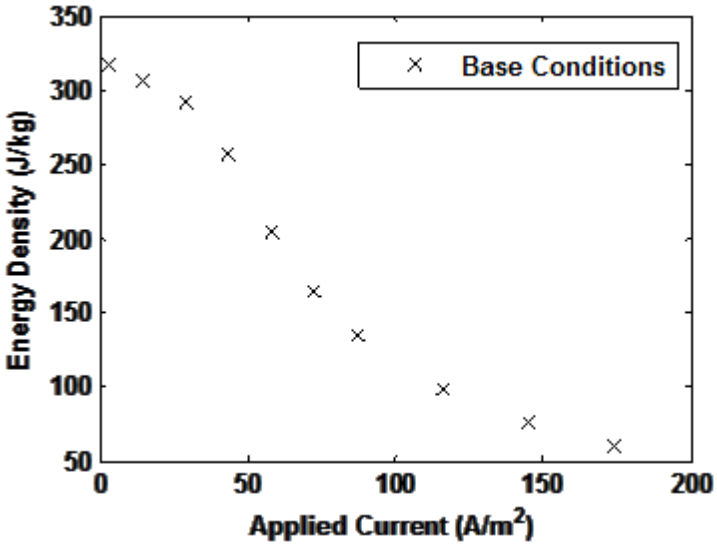

Fig. 2-2. Energy density drawn from battery vs. applied current for the base case

Fig. 2-2 presents the variation of specific energy with changing i_{app} when simulated using the base parameters listed in Table 2-2. The optimization of the electrode design parameters was performed in such a manner that the total discharge time t_d determined from simulation with the optimized parameters was not less than 99% of the original discharge time obtained with the base parameters (i.e. $0.99t_{d0} \le t_d \le t_{d0}$) for a specific applied current and fixed cut-off potential of 2.8 V. If this nonlinear constraint is not specified, a higher total energy density could be obtained but the battery may not last long enough for a given application (i.e. for a specific cycle, the battery will get depleted at a shorter time which is not useful for the application).

Definition of parameters	Base values
Thickness of cathode (l_p)	80 μm
Thickness of anode (l_n)	88 μm
Porosity of cathode (ε_p)	0.385
Porosity of anode (ε_n)	0.485

Table 2-2. Base battery design parameters

2.3 One –parameter optimization

The first optimized design parameter was the thickness of the positive electrode (i.e. cathode). Although the thickness of the positive electrode, l_p, was directly optimized, the ratio of the thicknesses of electrodes was fixed as l_n/l_p=1.1 to ensure that the battery was cathode-limited. The cathode to anode thickness ratio was kept fixed but the anode thickness varied according to it for the optimization protocol. Lower and upper bounds for l_p were set as 40 and 90 microns. The aim can be stated as: maximize the energy density, *E,* such that the partial differential equations governing the battery model are satisfied with optimized parameter values within their respective bounds along with the constrained conditions for l_n, while ensuring that the battery lasts for a specified minimum duration for a given rate of discharge. Mathematically, this can be represented as follows:

$$
\begin{aligned}
&\max\ E(l_p) = \frac{1}{M}\int_0^{t_d} V i_{app}\, dt \\
&\text{subject to the constraints} \\
&\frac{dy}{dt} = f(y,u) \\
&g(y,u) = 0 \\
&40\ \mu m \le l_p \le 90\ \mu m \\
&0.99 t_{d0} \le t_d \le t_{d0} \\
&l_n = 1.1 l_p
\end{aligned}
\qquad (2.4)
$$

where the differential and algebraic equations were derived from the partial differential equations for the battery model.

Fig. 2-3 compares specific energy densities drawn from the battery for the 1-parameter optimization vs. the base case, which are very similar due to the tight constraint on the discharge time.

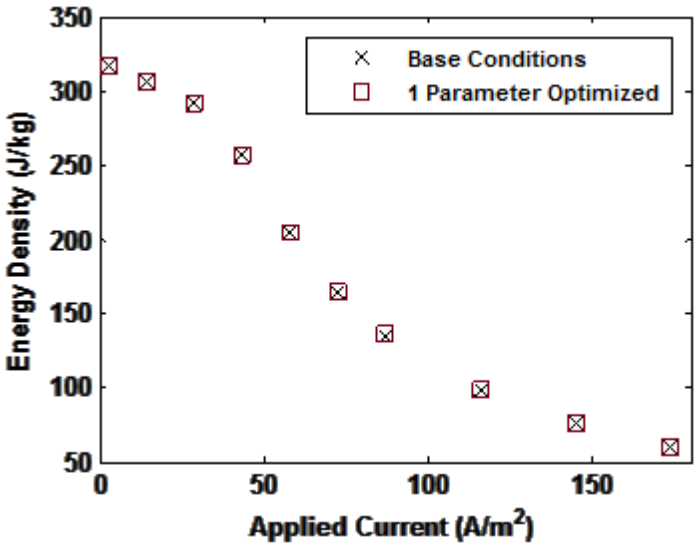

Fig. 2-3. Energy density drawn from battery vs. applied current for the base case and the one-parameter optimization case

As mentioned earlier, an increase in applied current density results in a decrease in the specific energy for both the base parameters and one parameter optimization cases but no considerable improvement is observed for the optimized case from the base case. Any reduction in the electrode thickness will reduce the mass per unit area of the cell, but also reduces the capacity, ensuring that the battery does not meet the minimum discharge time requirements, while increasing the thickness results in increasing the capacity but results in underutilization. This limits our ability to optimize l_p for the battery with strict discharge time constraint to give

optimized parameters which make physical sense. Due to this reason, the specific energy obtained from the cell with optimized cathode thickness does not increase much compared to those from the base parameters. The optimal electrode thickness would be different from the base case if the discharge time constraint was relaxed and a considerable improvement in the specific energy drawn from the cell would be observed. This result shows simultaneous optimization of two or more parameters is necessary if an increase in energy drawn is desired without loss in capacity and fulfilling discharge time requirements for specific applications.

2.4 Two-parameter optimization

Here the thickness (l_p) and porosity (ε_p) of the cathode were the design parameters optimized to maximize the energy density. The optimization was again performed by considering a fixed electrode thickness ratio of 1.1. Lower and upper bounds for ε_p were maintained at 0.29 to 0.5, respectively, while the bounds for l_p were retained as in the previous case. The optimization statement is given below.

$$
\begin{aligned}
&\max\ E(l_p, \varepsilon_p) = \frac{1}{M}\int_0^{t_d} Vi_{app}\,dt \\
&\text{subject to the constraints} \\
&\frac{dy}{dt} = f(y,u) \\
&g(y,u) = 0 \\
&[40\ \mu m, 0.29]^T \le [l_p, \varepsilon_p]^T \le [90\ \mu m, 0.5]^T \\
&0.99 t_{d0} \le t_d \le t_{d0} \\
&l_n = 1.1 l_p
\end{aligned}
\tag{2.5}
$$

Fig. 2-4 compares the specific energy profiles for this case with the one parameter optimized and base parameter cases.

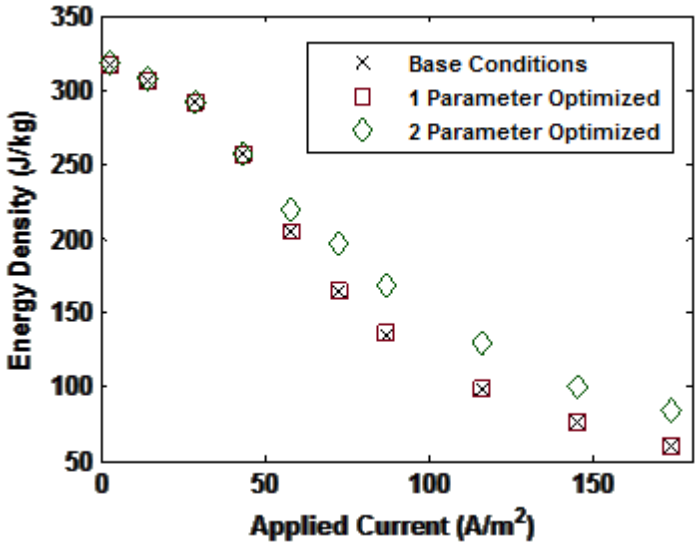

Fig. 2-4. Energy density drawn from battery vs. applied current for the base case and the two and one-parameter optimization cases

The strict constraint for minimum discharge time was maintained during the optimization protocol. A significant improvement in the specific energy was obtained compared to both the base and one-parameter optimization cases thus proving the importance of simultaneous optimization of design parameters. The improvement is not considerable for lower current densities but is significant for the higher values of current density. Quantitatively, there is almost a 25% increase in energy density compared to the base case for an applied current density, i_{app}, of 86.9625 A m^{-2}. The enhanced performance compared to the base case for some values of i_{app} is due to improved behavior of the internal variables which will be discussed in the later sections. For operation at higher current densities, more transport limitations are faced compared to lower currents. Therefore, optimization of cathode design parameters, improves the performance of the kinetic and transport variables which in turn provides the enhanced performance of the cell by increasing the energy drawn significantly. By inspection of the optimal (l_p, ε_p) for each value of the applied current, it was observed that allowing the porosity to be adjusted freed the electrode

thickness to be adjusted much more significantly while satisfying the constraints. The behavior of the optimized parameters will be discussed in detail in the coming sections. Nevertheless, this study proved the importance of simultaneous design parameter optimization for improvement of cell behavior.

2.5 Three-parameter optimization

The parameters optimized were the electrode thickness, porosity of the cathode, and porosity of the anode (ε_n). The upper and lower bounds on the porosity of the anode were 0.36 and 0.61, respectively. The bounds for the cathode parameters were identical to those mentioned for the previously discussed cases. The constraint for minimum discharge time requirements is still valid for the scheme. The optimization protocol is given below.

$$
\begin{aligned}
&\max\ E(l_p, \varepsilon_p, \varepsilon_n) = \frac{1}{M}\int_0^{t_d} V i_{app}\, dt \\
&\frac{dy}{dt} = f(y,u) \\
&g(y,u) = 0 \\
&[40\ \mu m, 0.29, 0.36]^T \le [l_p, \varepsilon_p, \varepsilon_n]^T \le [90\ \mu m, 0.5, 0.61]^T \\
&0.99 t_{d0} \le t_d \le t_{d0} \\
&l_n = 1.1 l_p
\end{aligned}
\tag{2.6}
$$

Fig. 2-5 compares the specific energy drawn from the cell for the 3 parameter optimization case with the previously discussed optimization protocols and base parameters.

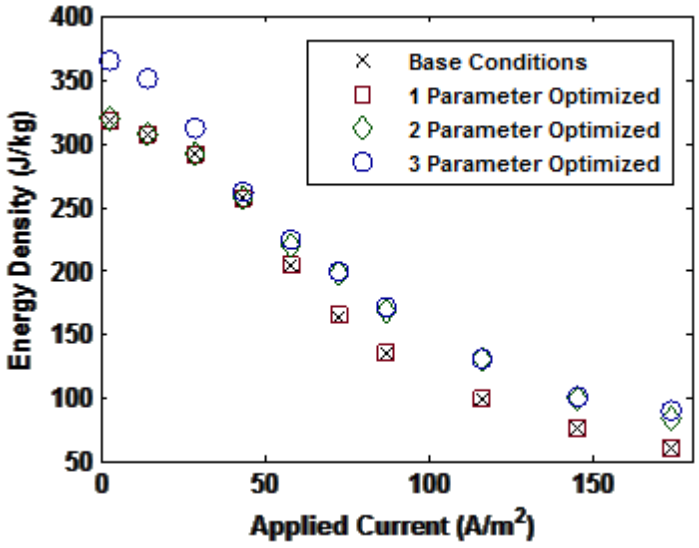

Fig. 2-5. Energy density drawn from battery vs. applied current for the base case and the three, two and one-parameter optimization cases

Three parameter optimization achieved higher specific energy compared to one parameter optimization and base parameter cases, but for low values of the applied current density, the 3-parameter optimization results have much higher energy density than the 2-parameter optimization (see Fig. 2-5). For high values of applied current density (e.g., for i_{app} = 86.9625 A m^{-2} and beyond), optimization of the anode porosity provided a small increase in energy density over optimization of the cathode porosity and cathode thickness. This is because the parameters were optimized with the discharge time constraint which does not allow them to go beyond a certain limit. As soon as the anode porosity was made to be an optimized parameter within specified physically acceptable bounds, it allowed the cathode porosity and cathode thickness to be adjusted accordingly to give high specific energy, especially at the low current density cases while still maintaining the conditions for discharge time constraint. This is because it lowers the porosities for the electrodes which enhances the kinetic and transport behavior at low rates rather than high rates which are discussed in detail later. These results also tell us that at all applied

current densities 3 parameter optimization is not necessary to get the best performance from the cell. As shown here, optimization of cathode parameters are enough to get more specific energy for high current densities. This analysis is true for the chemistry chosen, and might vary for other chemistry or designs.

2.5 Four-parameter optimization

In this case all the four electrode design parameters (thickness and porosity for both the electrodes) were selected for optimization simultaneously. For this optimization protocol, the anode thickness was optimized just like the other parameters, with upper and lower bounds of 32 microns and 108 microns respectively. The electrode thickness ratio of 1.1 maintained for each of the previously discussed optimization schemes was therefore neglected. The strict discharge time constraint was still applied to the protocol. Previously the optimization protocols always maintained that the anode thickness was always greater than the cathode thickness. This case was simulated to allow the anode thickness to drop below the cathode thickness. The other parameters retained the same upper and lower bounds as in the previous routines.

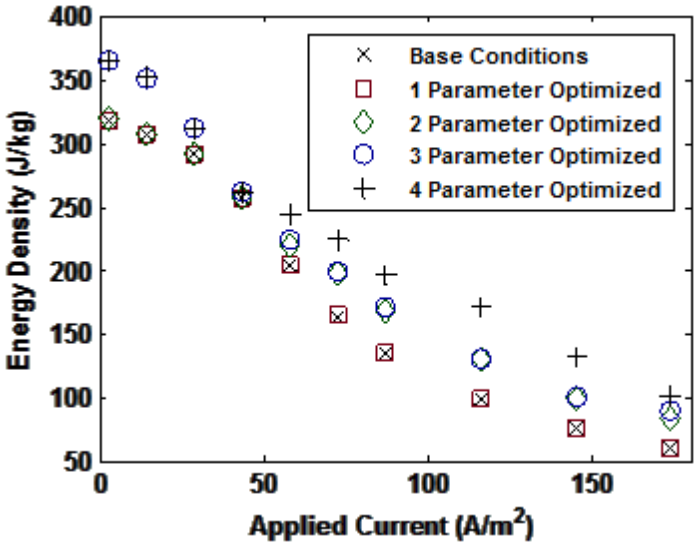

Fig. 2-6. Energy density drawn from battery vs. applied current for the base case and the four, three, two and one-parameter optimization cases

It should be noted that the four parameter estimation is shown only for demonstration purposes. Typically, lithium ion batteries are manufactured such that the anode capacity is greater than cathode capacity, due to cost. Moreover, the maintenance of the cathode to anode thickness is necessary to match the capacities on both positive and negative sides of the cell. For this reason, the fixed ratio of the electrode thicknesses used for the other optimization cases is considered more meaningful for real world applications. Fig. 2-6 is intended to show the comparison of energy drawn for four parameter optimization compared to all the other previously mentioned cases of simulation. As expected four parameters optimized simultaneously is the best option from the point of view of maximization of energy, but not practically relevant because of the relatively inexpensive anode materials compared to cathode materials. Examining the plot, it is visible that for higher applied current values the results from four parameter optimization case show significant improvement compared to 3 parameter optimization case. Previously it was seen that the 3 parameter optimization did not improve the drawn specific energy compared to

the 2 parameter optimization case at higher values of applied current. As mentioned earlier these results are just for demonstration purposes and they may not be of practical significance as the anode thickness was optimized simultaneously with the other variables without maintaining the electrode thickness constraint.

2.6 Electrochemical behavior

One of the main advantages of using physics-based models is the ability to understand the physical behavior associated with an optimal battery design. Empirical models are often valid only across a small range of scenarios. When empirical models are used for optimization, they usually converge to meaningless solutions and the internal non-measurable variables cannot be analyzed. The design parameters from the results from empirical model-based optimization may not make sense when given as input and simulated with physics-based models. The below simulations were performed with the optimized parameters obtained from all the cases for all the values of discharge current.

2.7 Internal behavior

Simulations performed with the optimized parameters for all cases show improved electrochemical and transport behavior, which increases the specific energy. We compare the electrochemical behavior at higher rates (e.g.2C rate) as improved performance is more visible at high rates. Fig. 2-7 shows the surface solid-phase concentration at the interfaces for a 2 C rate of discharge.

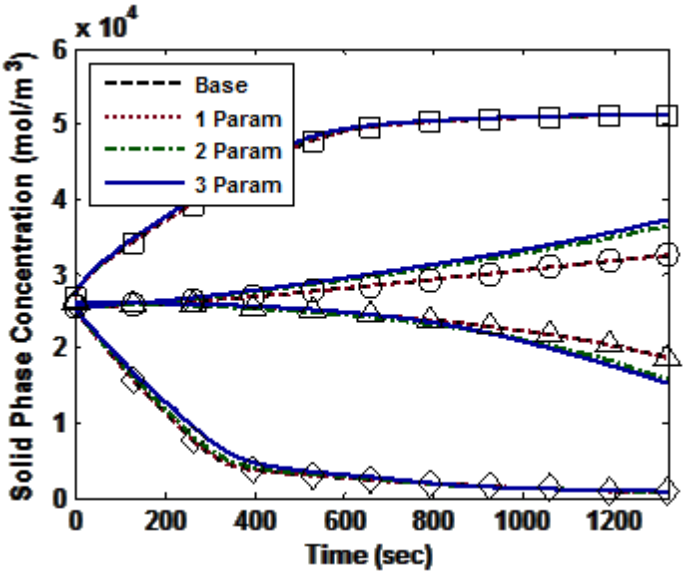

Fig. 2-7. Solid-phase surface concentration throughout discharge for a 2 C rate

In all cases, the capacity in the electrodes is nearly fully utilized in the region near the separator, as indicated by the rapid increase (for the cathode) and decrease (in the anode) of the surface concentration at the beginning of discharge which tapers off near the end (□ & ◊). However, less capacity is used near the current collectors for all cases (○ & Δ) due to the mass transfer resistance of the porous electrodes. The optimization minimized this resistance and allows a greater portion of the electrodes to be utilized, as shown in the solid line of Figure 7a. It is clear from the plots that there is an enhancement in the utilization of the active material in the electrodes to improve performance with the simultaneous optimization of multiple design parameters. For 1 parameter optimization there is no significant performance enhancement but the 3 parameter optimization clearly improves the utilization marked with improved cell performance and increased specific energy. Fig. 2-8 shows the variation of electrolyte concentration within the cell at different regions, the cathode, the separator and the anode during discharge for different optimization scenarios for 2C discharge rate.

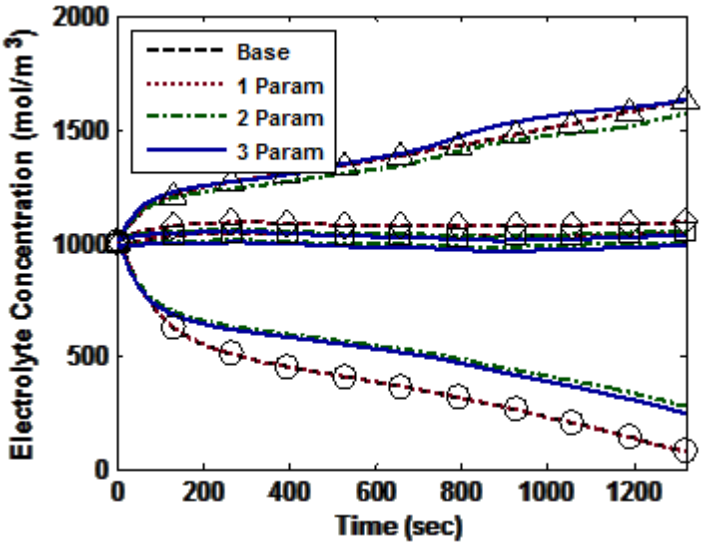

Fig. 2-8. Electrolyte concentration throughout discharge for a 2 C rate

We see that the electrolyte concentration for the two parameter optimization is closer to the equilibrium (initial) concentration of 1000 mol m^{-3} compared to the other cases. If the specific system cannot withstand or handle a high drain in the liquid phase or very low electrolyte concentrations in the anode region, the two parameter optimization results should be used ignoring the three parameter optimization results. On the other hand, if the system can withstand the magnitude of starvation of electrolyte, the three parameter optimization results can be used to get the maximum energy density. Thus, based on variations of the intrinsic variables, we can decide on the number of design parameters to be optimized or the type of results that we can use for that specific system. This is not possible when doing a trial and error based design, or model based design based on empirical models, and is one of the advantages of using a physics based model for optimal design.

2.8 Optimized parameters

Variation of the optimized parameters vs. applied current density for all of the optimization protocols were plotted and compared with the base values, which is represented as a straight line in the plots given in Figs. 2-9 to 2-12 .Figure 2-9 shows the variation of optimal cathode thickness for specified applied current densities, while Figs. 2-10 and 2-11 show the optimal cathode and anode porosity variations. Fig. 2-12 represents the optimal anode thickness l_n variation for specified applied current densities which is only valid for 4 parameter optimization case. Data for optimized values for cathode thickness l_p is available for all four cases of optimization while cathode porosity can be plotted only for 2,3 and 4 parameter optimization cases and anode porosity for 3 and 4 parameter optimization cases only. In general, but not always, applications with higher discharge rates require higher porosities and smaller electrode thicknesses. This design reduces mass transfer resistances within the cell, which can be a limiting factor at higher rates. At low discharge rates, the cell capacity is limiting, so lower porosities and greater thicknesses are preferred. The strict discharge time constraint in the optimization protocol helps control all the factors affecting the kinetic and transport behavior of the cell correctly so as to obtain optimized design parameters which are suitable for specific applications and make physical sense. Looking at the variation of the optimized cathode thickness, for 1 parameter optimization there is not much change in optimized values compared with the base values which is reflected in the negligible improvement of specific energy for this optimization protocol from the base parameter case. For the 2 parameter optimization case, the cathode thickness does not vary considerably from the base values at low current densities, but for higher current densities the optimized values decrease from the base value.

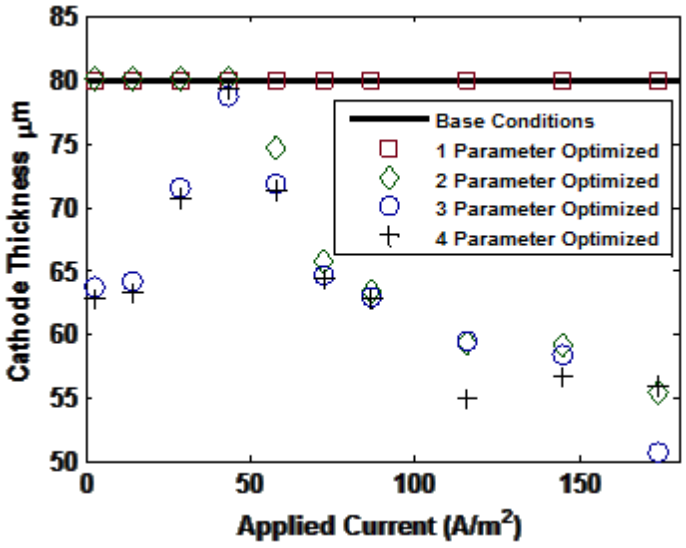

Fig. 2-9. Variation in the optimal cathode thickness (l_p) with applied current for all optimization cases

The cathode porosity variation for 2 parameter optimization shows that for low current densities the optimized values do not deviate considerably from the base values. For the lowest current density value it starts at a higher magnitude compared to the base value and decreases until it becomes almost equal to it for i_{app}=43.48125 A m^{-2}. After that they increase from the base value as the current density increases. Therefore, the improvement in specific energy obtained is considerable for higher current densities as the optimized parameters obtained from the two parameter optimization facilitate enhanced transport and kinetic behavior. For the 3 parameter optimization case, the optimized values for cathode thickness is less than the base values at low current densities but it increases and at i_{app}=43.48125 A m^{-2} it becomes almost equal to the base parameter value. After that it again decreases considerably from the base value. The optimized cathode porosity variation for the three parameter optimization follows a similar trend.

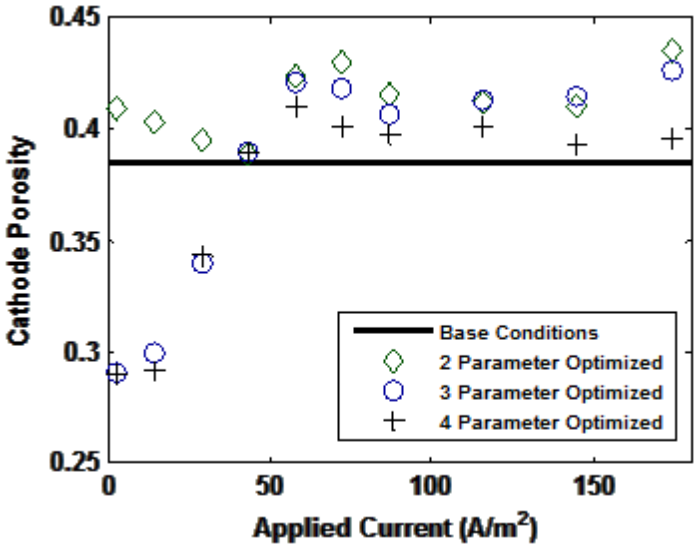

Fig. 2-10. Variation in the optimal cathode porosity (ε_p) with applied current for all optimization cases

It nearly hits the lower bound for low current densities but then climbs gradually as it approaches the base value at similar value of i_{app} mentioned previously. With the increase in current density the optimized cathode porosities continue to increase beyond the base value. It is observed that, at high current densities, the optimized cathode porosity and thickness do not vary much from the 2 parameter optimization case to the 3 parameter optimization protocol. This causes the negligible improvement observed in the specific energy for high i_{app} values between the two protocols. The variation in optimized anode porosity with current density approaches the lower bound at low applied current densities but increases and at higher current densities but does not appear to follow any particular trend. It should be noted that the anode porosity was optimized along with the cathode parameters and the cell is cathode limited.

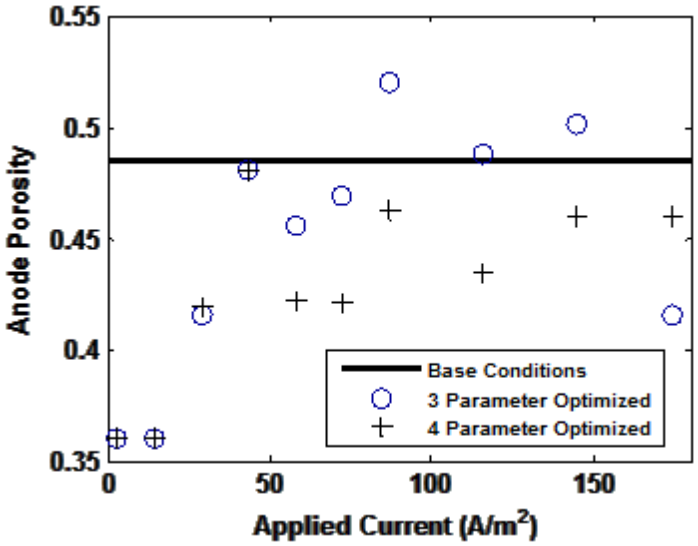

Fig. 2-11. Variation in the optimal anode porosity (ε_n) with applied current for all optimization cases

For increasing specific energy, lower values of electrode thickness and porosity look to be more desirable but the parameters are optimized in such a fashion that the strict minimum discharge time constraint is satisfied all times to give physically and practically meaningful optimized design parameters. This probably justifies the irregular variation of some of the optimized parameters.

For four parameter optimization case, the variation of the optimized cathode thickness shows a trend similar to the 3 parameter optimization protocol. The optimized cathode porosity variation for 4 parameter optimization is again of similar trend as seen for the 3 parameter optimization case. For lower values of current densities, both 3 and 4 parameter optimization cases predict somewhat similar values for optimized cathode porosities but at higher currents slightly lower values are predicted which are very close to the base value.

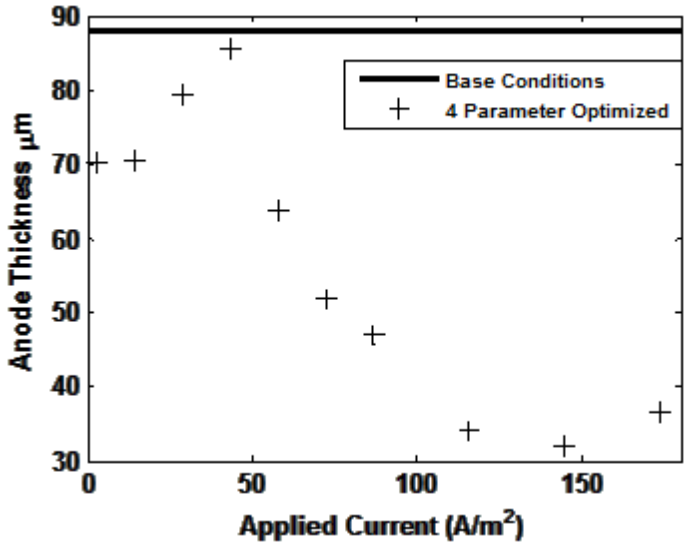

Fig. 2-12. Variation in the optimal anode thickness (l_n) with applied current for all optimization cases

The optimized anode porosity profile shows similar irregular trends as the 3 parameter optimization case especially for the higher current densities. But for most current values, the optimized anode porosity gives lower values compared to those shown for 3 parameter optimization case except for i_{app}=173.925 A m^{-2}. The optimized anode thickness profile is only available for the four parameter optimization case. As mentioned earlier, the criterion for electrode thickness ratio was not maintained for this protocol. For all values of applied current, the optimized anode thickness values are below the base parameter values. For other cases of optimization, the electrode thickness ratio criterion maintained the anode thickness to be greater than the cathode thickness. It should be kept in mind that the optimized parameter values for the 4 parameter optimization case, do not make any practical sense as the anode thickness was optimized simultaneously with the other variables without considering cost or possible discrepancies like unbalance of capacity on positive and negative sides of the sandwich etc. which are accounted for when using the electrode thickness constraint used in the other

optimization schemes. These results are just for demonstration purposes and although they show increase in specific energy they should not be considered for design purposes.

2.9 Optimality of optimized parameters

There is a need to verify that the optimized electrode design parameters obtained are indeed optimal i.e. maximum specific energy is obtained when the electrode architecture is designed accordingly. To perform this check, the reformulated battery model was run with values of one of the optimized parameters ranging from lower bound to upper bound while the others were held at optimal conditions or at base conditions. From each simulation, the maximized specific energy obtained was plotted against the varied design parameter for all performed protocols of optimization. For example, optimized cathode thickness was plotted on the x-axis and maximized energy density on the y-axis, with cathode and anode porosities held at their optimal values for three parameter optimization. Such plots will show the optimal solutions as peaks. The optimization protocols discussed in the paper follow a strict time constraint. The simulations for all values of varied optimized parameter does not satisfy this constraint and therefore maximized specific energy obtained has been set to zero for these cases. The x mark on the plots represents the optimal values of the varied selected parameter obtained from the optimization schemes.

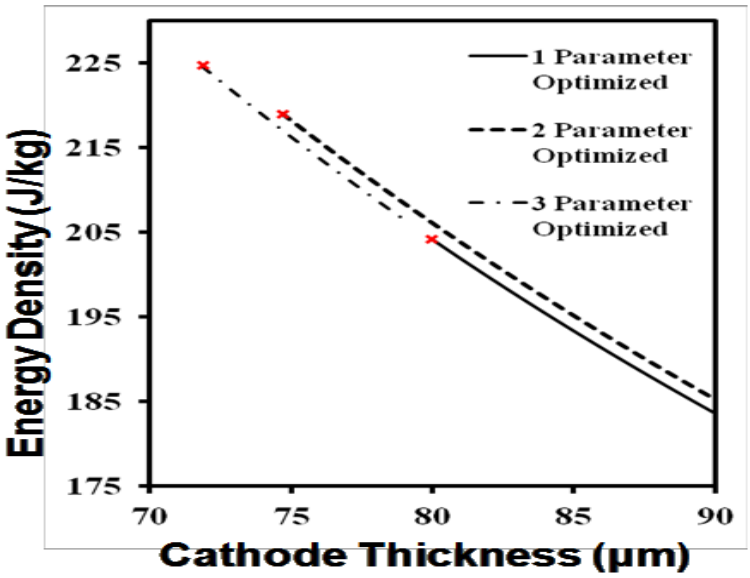

Fig. 2-13. Energy density drawn from the battery vs. varying cathode thickness (l_p)

Fig. 2-13 shows the plots of maximized energy density with variable cathode thickness for the different protocols of optimization at 2 C discharge rate. As expected, the optimal solutions are at the peaks of the plots. Another interesting observation is that after the optimal peak with decreasing magnitude of cathode thickness, the specific energy continues to decrease. This is the effect of thicker electrodes.

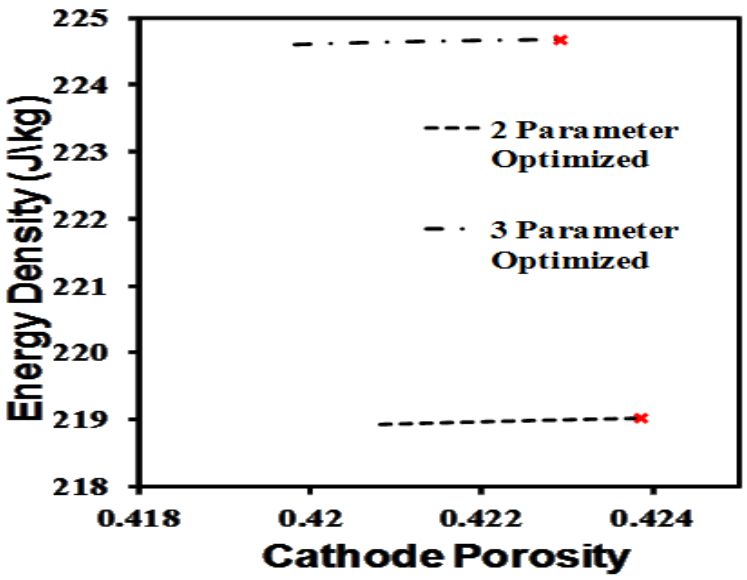

Fig. 2-14. Energy density drawn from the battery vs. varying cathode porosity (ε_p)

Fig. 2-14 show similar plots for variable cathode porosity at 2 C discharge rate. For all the plots, the optimal values represent the peaks of the profiles. This trend verifies that the optimization protocols indeed give optimal values of design parameters for which the corresponding values of drawn specific energy are maxima.

List of symbols

E = specific energy density of the cell (Watt hour kg^{-1})

V = potential drop across the cell (Volt)

i_{app} = applied current density (Ampere m^{-2})

t = time (seconds)

M = mass per unit area (kg m^{-2})

ρ_n = density of negative electrode (kg m^{-3})

l_n = thickness of negative electrode (m)

ρ_p = density of positive electrode (kg m^{-3})

l_p = thickness of positive electrode (m)

ε_n = porosity of negative electrode

ε_p = porosity of positive electrode

$\varepsilon_{f,n}$ = volume fraction of filler in negative electrode

$\varepsilon_{f,p}$ = volume fraction of filler in positive electrode

ρ_e = density of electrolyte (kg m^{-3})

l_s = thickness of separator (m)

t_{d0} = total discharge time obtained by model simulation with base parameters (s)

t_d = total discharge time obtained by model simulation with optimized parameters (s)

Chapter 3

Mathematical model for lithium intercalation for silicon electrode

3.1 Introduction

Silicon electrode is pursued as a potential negative electrode for lithium-ion batteries owing to its high gravimetric (mAh/g) and volumetric capacity (mAh/L) compared to the existing state of the art graphite electrode [65]. One of the critical challenges in the commercialization of Si electrode is to minimize particle fracture developed during lithiation and delithiation of the Si electrode [66,67]. Recent experimental studies have demonstrated the use of nano-size Si structures as electrodes. These electrode structures exhibited minimal particle fracture and also enabled repeated cycling [68-70]. While different mechanisms have been proposed for this behavior, a detailed physics based analysis combining the electrochemical and structural aspects of lithium insertion in such nanostructures have not been undertaken. A variety of detailed phenomenological models exists in the literature for lithium intercalation in porous electrodes, which treat the transport of electrolyte due to diffusion and migration, reaction kinetics at interfaces, and transport of Li and electrons in solid phase [10,47,48,51,71-73]. The general modeling framework presented in these papers cannot be directly used to simulate advanced high capacity electrodes, specifically the alloy type electrodes such as Si, Sn etc., because (a) the stresses developed during lithium insertion/deinsertion and (b) volume change associated with

lithium insertion/deinsertion are not considered. So to accurately model such type of high capacity electrodes which undergo substantial volume changes, particle level expansion/contraction and electrode level displacement along with buildup of stresses have to be captured. Early research by Prussin [74] demonstrated that the diffusion induced stresses generated by concentration distributions are of similar nature to the thermal stresses developed in elastic medium. Modeling of diffusion induced stresses was also studied in detail by other researchers for different geometries such as hollow cylinders, plates etc.[75-78] . Similar approaches were extended to battery electrode chemistries on a particle level to calculate intercalation induced stresses assuming no volume changes. Zhang et. al. [79] presented a numerical model to calculate diffusion induced stresses for spherical and ellipsoidal shaped $LiMn_2O_4$ single particle. Also, the work by Cheng and Verbrugge [80,81] derived analytical expressions (assuming negligible pressure induced diffusion and no volume change) to calculate stresses that arise from concentration gradients for a spherical particle. This modeling framework was also incorporated into a porous electrode framework [82]. All the above referenced models in addition to other published work [83-85] were developed assuming dilute solution theory for diffusion within particle, with no moving boundaries (negligible volume change) and for low expansion materials.

Christensen et. al. [40] presented a more rigorous mathematical framework based on concentrated solution theory, which incorporates volume expansion and stress build up in a single spherical particle electrode and case studies for lithiation in a spherical carbon particle (8% volume expansion) were discussed. The same framework was also used to calculate the stresses in $LiMn_2O_4$ single spherical particle electrode [86] and was also later extended to porous electrodes [87] containing graphitic mesophase-carbon-microbead (MCMB) anode and lithium

manganese oxide spinel cathode. The author also emphasizes the importance of thermodynamic factor, pressure driven diffusion and extent of volume change in determining the cell potential profiles and initiation of fracture. However most of the above mentioned work was based on electrodes which undergo volume change in the order of 10%. To model large volume expansion in electrodes, Chandrasekaran et. al. [88] modeled a single particle Si electrode under galvanostatic and potentiodynamic control of lithiation of Si to $Li_{3.75}Si$ associated with a 270% volume change. In a later paper [89], the same approach was extended to a porous electrode to describe how particle level expansion affects the porosity of the electrode. The authors ignored stress calculations based on the assumption that the nano sized particles would not build appreciable concentration gradients to generate diffusion induced stresses. Gao et. al. [90] modeled stress buildup due to concentration gradients for a 1-d (radial) cylindrical geometry for a nano sized Si electrode for a dilute solid solution with constant density. The authors also discuss the strong coupling between stress enhanced diffusion and diffusion induced stresses for electrodes associated with large volume expansion. In this paper (Part I), we present a model to describe diffusion and stress build up in a 2-d silicon nanowire (Si NW) geometry anchored to a Cu substrate under galvanostatic conditions. The model in general follows the framework described in reference [40] but applied to Si electrode with a maximum lithiation to $Li_{3.75}Si$ associated with a 270% volume change.

3.2. Model assumptions

The geometry of the Si NW anchored to the Cu CC substrate is shown in Fig. 3-1 (left); the initial unexpanded radius and the length of the Si NW are R_{NW}=50 nm and H_{NW} = 10 μm respectively. The model geometry consists of a 2-d axisymmetric cut from the overall geometry

as shown in Fig. 3-1 (right), wherein the dependence of the variables in the θ direction was ignored.

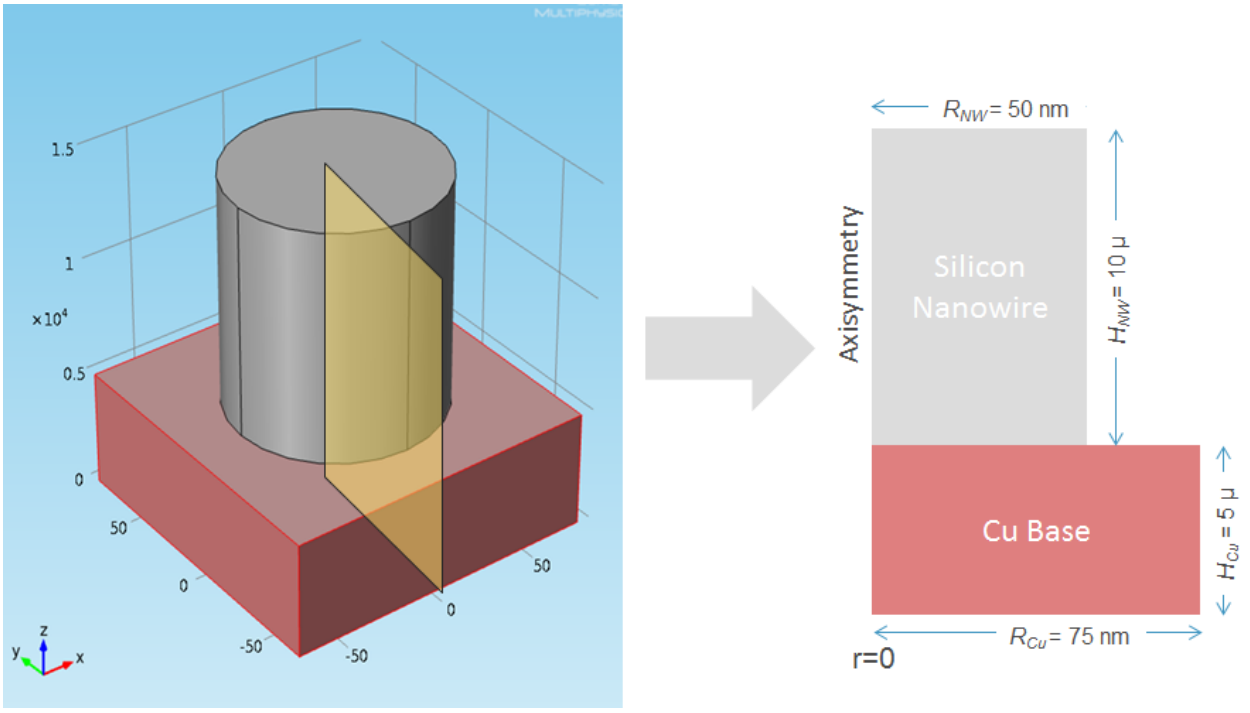

Fig. 3-1 Schematic of the Si NW anchored to the Cu-CC substrate (left). 2-d axisymmetric slice of Si NW anchored to Cu-CC base substrate used as the geometry for the 2-d model (right).

Other key assumptions in the model were

1. The charge storage mechanism in the Si electrode is modeled by considering the electrochemical reaction of Li at the surface of the Si NW followed by transport of Li into the Si NW. The lithiated Si mixture is represented as a solid solution, therefore phase transitions are ignored.

2. The transport of the host silicon is solely due to the convective flux, whereas the transport of lithium is due to the combined effect of gradients in concentration and pressure, and convective flux.

3. Lithium diffusion into Cu CC substrate is ignored and therefore the Si NW/Cu CC interface acts as a Li blocking interface.

4. Stress strain relationship was assumed to obey Hooke's law (linear) in the entire lithiation regime. For particles of nanometer radii, the stress generated due to insertion is typically less than the yield stress limit for onset of plasticity, therefore the system is assumed to stay elastic throughout lithiation.

5. For galvanostatic studies, the total current to the Si NW was maintained constant; the current density at the surface of the Si NW was taken to be constant spatially, however it changes with time in accordance with the increase in surface area related to volume expansion.

6. Isothermal conditions were assumed during lithiation of the Si NW.

3.3 Model equations

The electrochemical equilibrium reaction between Li and Si is written in the form

$$zLi^{+} + ze^{-} + \frac{1}{\Delta x} Si \leftrightharpoons \qquad (3.1)$$

The above reaction can be thought of a single electron transfer reaction ($Li^{+} + e^{-} \leftrightharpoons$, followed by lithium alloying with $Si_{\frac{1}{\Delta x}}$, where z is the intercalation fraction of LiS, and Δx is the maximum number of moles of Li that can reversibly alloy with Si. The binary species chosen are the empty (Li free) host lattice and the lithiated host lattice. Note, the host lattice in this work is $\frac{1}{\Delta x} Si$ and the lithiated host is $LiSi_{\frac{1}{\Delta x}}$ and will be denoted hereafter as S and LiS respectively. The value of Δx was measured to be $22/5$ at high temperatures in an earlier work [91]. In our

work, the value of Δx is taken as $15/4$ which was measured at room temperature by different groups [92-94].

In the Si-NW electrode, the flux of LiS is obtained through the generalized Maxwell-Stefan equation [95]. Considering ideal solution, ignoring thermal and external forced diffusion effects in the generalized Maxwell-Stefan relation and rearranging for the flux of species N_{LiS} we obtain

$$N_{LiS} = x_{LiS}\left(N_{LiS} + N_S\right) - c_T D_{LiS,S}\left[\alpha_{LiS}\nabla x_{LiS} + \frac{x_{LiS}}{RT}\left(V_{LiS} - \frac{M_{LiS}}{\rho}\right)\nabla p\right] \tag{3.2}$$

where N_{LiS}, N_S and x_{LiS}, x_{Si} are the molar fluxes and mole fractions of the respective species, M_{Li} and V_{LiS} are the molar mass and molar volume of LiS, c_T is the total concentration, i.e. $c_T = c_{LiS} + c_S$, α_{LiS} is the thermodynamic factor and ρ is the density of the material

$$\rho = c_T \sum x_i M_i \tag{3.3}$$

The flux of S is considered purely to be convective, and the lattice velocity is defined through the molar averaged velocity, i.e. $v^{\diamond} = x_{LiS}v_{LiS} + x_S v_S$. The total molar flux is related to the molar average velocity as

$$N_{LiS} + N_S = c_T v^{\diamond} \tag{3.4}$$

The partial molar volume of species LiS, V_{LiS} is given as a function of the molar volume of the host material V_S and the expansion factor ξ, where ξ is defined as the percentage volume change expressed in fraction.

$$V_{LiS} = V_S\left(1+\frac{\xi}{z_{max}}\right) \tag{3.5}$$

The mass balance for the species LiS is written as

$$\frac{\partial c_T x_{LiS}}{\partial t} + \nabla \cdot N_{LiS} = 0 \tag{3.6}$$

The total concentration c_T and the pressure p will be described after discussion of the diffusion induced stresses.

At the outer boundary of the Si-NW, a constant current flux condition was used as the boundary condition, while at the center an axial symmetry condition was used. In actual electrodes, the kinetics and the mass transfer of the species in solution could determine the actual current distribution, however in this study, we have restricted our simulations for the case of uniform current distribution along the nanowire.

$$\begin{cases} -n \cdot N_{LiS}\big|_{r=R_{NW}(t),z} = & \dfrac{-s_i i_{app}}{F} \\ -n \cdot N_{LiS}\big|_{r,z=H_{NW}(t)} = & \dfrac{-s_i i_{app}}{F} \end{cases} \tag{3.7}$$

$$-n \cdot N_{LiS}\big|_{r=0,z} = 0 \tag{3.8}$$

The Eulerian strain for the case of small deformation can be described in the tensor notation as

$$\epsilon \quad \left(\mathbf{u}\nabla_{\mathbf{x}}\right)^{\mathrm{T}}\right) \tag{3.9}$$

For large deformation analysis, the strains have to be calculated using the non-linear form for the Eulerian strain as

$$\epsilon \quad + \nabla_{\mathbf{x}}\mathbf{u} - \mathbf{u}\nabla_{\mathbf{x}} \cdot \left(\mathbf{u}\nabla_{\mathbf{x}}\right)^{\mathrm{T}} \Big) \tag{3.10}$$

where $\mathbf{u}$ is the displacement vector calculated from the current and the initial configuration of the volume element . For finite deformation, the strain tensor for the 2D axial symmetry case, in the cylindrical co-ordinates is written as

$$\epsilon \quad \begin{bmatrix} \epsilon & \epsilon & \epsilon \\ \epsilon & \epsilon & \epsilon \\ \epsilon & \epsilon & \epsilon \end{bmatrix} \begin{bmatrix} \frac{\partial u}{\partial r} + \frac{1}{2}\left[\left(\frac{\partial u}{\partial r}\right)^2 + \left(\frac{\partial w}{\partial r}\right)^2\right] & 0 & \frac{1}{2}\left(\frac{\partial u}{\partial z} + \frac{\partial w}{\partial r} + \frac{\partial u}{\partial r}\frac{\partial u}{\partial z} + \frac{\partial w}{\partial r}\frac{\partial w}{\partial z}\right) \\ 0 & \frac{u}{r} + \frac{1}{2}\left(\frac{u}{r}\right)^2 & 0 \\ 0 & 0 & \frac{\partial w}{\partial z} + \frac{1}{2}\left[\left(\frac{\partial u}{\partial z}\right)^2 + \left(\frac{\partial w}{\partial z}\right)^2\right] \end{bmatrix} \tag{3.11}$$

where u, v, w are the displacements with respect to the initial configuration in the r, θ, and z directions respectively. The displacement v in the θ direction is zero based on the axi-symmetry assumption; subsequently ϵ and ϵ are also zero. The symmetric stress tensor describes the stress components in the material and contains three normal stress $\sigma_{rr}, \sigma_{\theta\theta}, \sigma_{zz}$ and the three symmetric shear stresses, i.e. $\tau_{r\theta}, \tau_{\theta z}, \tau_{rz}$ and the components are given as

$$\tau = \begin{bmatrix} \sigma_{rr} & \tau_{r\theta} & \tau_{rz} \\ \tau_{\theta r} & \sigma_{\theta\theta} & \tau_{\theta z} \\ \tau_{zr} & \tau_{z\theta} & \sigma_{zz} \end{bmatrix} \begin{Bmatrix} \tau_{rz} = & \tau_{zr} \\ \tau_{r\theta} = & \tau_{\theta r} \\ \tau_{rz} = & \tau_{zr} \end{Bmatrix} \tag{3.12}$$

The elastic stresses are correlated to the strains using the elastic moduli matrix, which is a fourth order tensor, but because of the symmetry and isotropic assumptions, the number of independent parameters in this matrix is reduced to 2, i.e. the Lame parameters, λ and μ. The stress-strain relationship therefore reduces to

$$\tau = \lambda \mathbf{tr}\left(\epsilon \qquad\qquad \epsilon \right. \tag{3.13}$$

The Lame parameters could be related to the more commonly used material properties, Young's Modulus (E) and Poisson's ratio (ν) through the relations

$$E = \frac{(3\lambda + 2\mu)\mu}{\lambda + \mu}, \nu = \frac{\lambda}{2(\lambda + \mu)} \tag{3.14}$$

In this system, the insertion of Li into the Si host introduces a significant volume change, atypical of common insertion electrodes such as $LiMn_2O_4$, $LiCoO_2$, $LiTi_5O_{12}$ etc. where the total volume change is typically less than 10% and therefore ignored in most models. To include the volume change formalism into the modeling framework, the total strain in the electrode is defined as the summation of the two components, chemical strain (stress free) and elastic component $\epsilon \quad \epsilon \quad \epsilon$; and the chemical strain is expressed as a function of the partial molar volumes and mole fractions of the species LiS and S, (note $x_{LiS} + x_s = 1$):

$$\epsilon \qquad \left(\frac{V_{LiS}}{V_S} - 1 \right)(\mathrm{I}) \tag{3.15}$$

Consequently, the elastic strain can be written as the difference between the total strain and the chemical strain, which can be plugged back into Eq. (3.12) to obtain the stress-strain relationship for electrodes undergoing elastic and chemical strains.

$$\epsilon \quad \epsilon \quad \epsilon \tag{3.16}$$

The total concentration c_T as described in Eq. (3.6) is written as a function of composition and pressure, which is related to the trace of the stress tensor

$$c_T = \xi\left(x_{LiS}, x_S\right)\psi\left(tr\left(\tau\right)\right) \tag{3.17}$$

The function ξ is purely composition dependent and can be defined as a function of partial molar volumes of the individual species. The function ψ is evaluated similar to the work of Christensen et. al. [40] using the definition of a compressibility factor in terms of differential volume element and mean normal pressure. Subsequently, Eq. (3.17) is expressed as

$$c_T = \left(x_{LiS}V_{LiS} + x_s V_S\right)^{-1}\exp\left[-\frac{1}{3K}tr\left(\tau\right)\right] \tag{3.18}$$

where K is the bulk modulus of the material. The pressure defined in Eq. (3.2) is the thermodynamic pressure, which is assumed to be equivalent to the mean normal pressure, and is expressed as

$$p = -\frac{1}{3}tr\left(\tau\right) \tag{3.19}$$

Finally, the equilibrium force balance equation in the 2-d axi-symmetry geometry is expressed as

$$\frac{\partial\sigma_{rr}}{\partial r} + \frac{\partial\tau_{rz}}{\partial z} + \frac{\sigma_{rr} - \sigma_{\theta\theta}}{r} = 0 \tag{3.20}$$

$$\frac{\partial\tau_{rz}}{\partial r} + \frac{\partial\sigma_{zz}}{\partial z} + \frac{\tau_{rz}}{r} = 0 \tag{3.21}$$

The individual velocity components of $v^{\Diamond}$ in Eq. (3.4) is calculated from the time derivatives of corresponding displacement fields.

$$v_r = \left.\frac{\partial u}{\partial t}\right|_{r,z} \tag{3.22}$$

$$v_z = \left.\frac{\partial w}{\partial t}\right|_{r,z} \tag{3.23}$$

Eqs. (3.20), (3.21), (3.6) and (3.18) were used to solve for the variables u, w, x_{LiS}, and c_T respectively in the Si-NW domain. The equilibrium force balance Eqs. (3.20) and (3.21) are also valid in the Cu-CC domain, with the exception that the total strain, ϵ is purely elastic and the chemical strain component is absent based on the assumption that lithium does transport into the Cu substrate.

The equilibrium force balance Eqs. (3.20) and (3.21) are also valid in the Cu-CC domain, with the exception that the total strain, ϵ is purely elastic and the chemical strain component is absent based on the assumption that lithium does transport into the Cu substrate. Therefore the displacement components u, w are the only variables to be solved for in the Cu-CC domain.

The force balance equation in the Si-NW was constrained to the following boundary conditions

$$\begin{cases} \sigma_{rr}\big|_{r=R_{NW}(t),z} & =0 \\ \sigma_{zz}\big|_{r,z=H_{NW}(t)} & =0 \end{cases} \tag{3.24}$$

The base of the Cu-CC substrate is subjected to fixed constraint boundary conditions

$$\begin{cases} u\big|_{r,z=0} = & 0 \\ w\big|_{r,z=0} = & 0 \end{cases} \tag{3.25}$$

The outer surface of the Si-NW, the top unanchored portion of the Cu-CC and the outer surface of the Cu-CC are assumed to be free surfaces i.e.

$$-n.\tau = 0 \tag{3.26}$$

3.4 Solving methodology & parameters

The equations are solved using COMSOL Multiphysics with the structural mechanics module to solve for the displacement components u, w (Eqs. 3.20 & 3.21) and a general PDE interface to solve for x_{LiS} (Eq. 3.6). The mass balance equations were re-written in terms of material derivatives for the ease of implementation in the material framework in COMSOL.

Since the dimensions of the Si NW change significantly upon lithiation, the initial mesh configuration has to be updated at each time step to accommodate for the updated geometry. In this model, the deformation of the mesh is determined by the displacement components (u , w) calculated from structural mechanics module. The technique for mesh movement is called an Arbitrary Lagrangian-Eulerian (ALE) method, which is an intermediate between the Lagrangian and Eulerian methods, and it allows moving boundaries without the need for the mesh movement to follow the material. For the 2-d model, the Si NW part of the geometry was mapped with 300 mode points along the axial direction, and 100 points along the radius, while the base Cu CC structure was mapped with 150 node points along the axial direction and 150 node points along the radius. In all, the geometry consisted of 52,500 quadrilateral, 1,300 line and 7 vertex elements. An absolute tolerance of 10^{-15} and 10^{-6} was used for the displacement variables (u ,

w) and x_{LiS} respectively, and a relative tolerance of 10^{-5} was used to establish convergence. Automatic time stepping (based on the solver) was used, and the computational run time taken for a complete charge (167 time steps) was 17281 s, using a 16 core Intel Xeon 2.27 GHz processor. The parameters used in the model are given in Table 3-1.

Parameter	Value	Units
Partial molar volume of *LiS*	13.11	ml mol^{-1}
Molar volume of *S*	3.214	ml mol^{-1}
Maximum number of moles of Li that can reversibly alloy per mole of Si	15/4	No units
Maximum insertion coefficient of Li in *LiS*,	1	No units
Diffusion coefficient of Li in Si	2e-12	$cm^2 s^{-1}$
Young's modulus of *LiS*	92.16	GPa
Poisson's ratio of *LiS*	0.27	No units
Young's modulus of Cu substrate	110	GPa
Poisson's ratio of Cu substrate	0.35	No units
Thermodynamic factor	1	No units
Expansion factor (measured at room temperature)	3.079	No units

Table 3-1. List of parameter values used in the simulation

3.5 Diffusion induced stresses

Fig. 3-2 shows the mole fraction distribution of *LiS* in the Si NW at the end of lithiation.

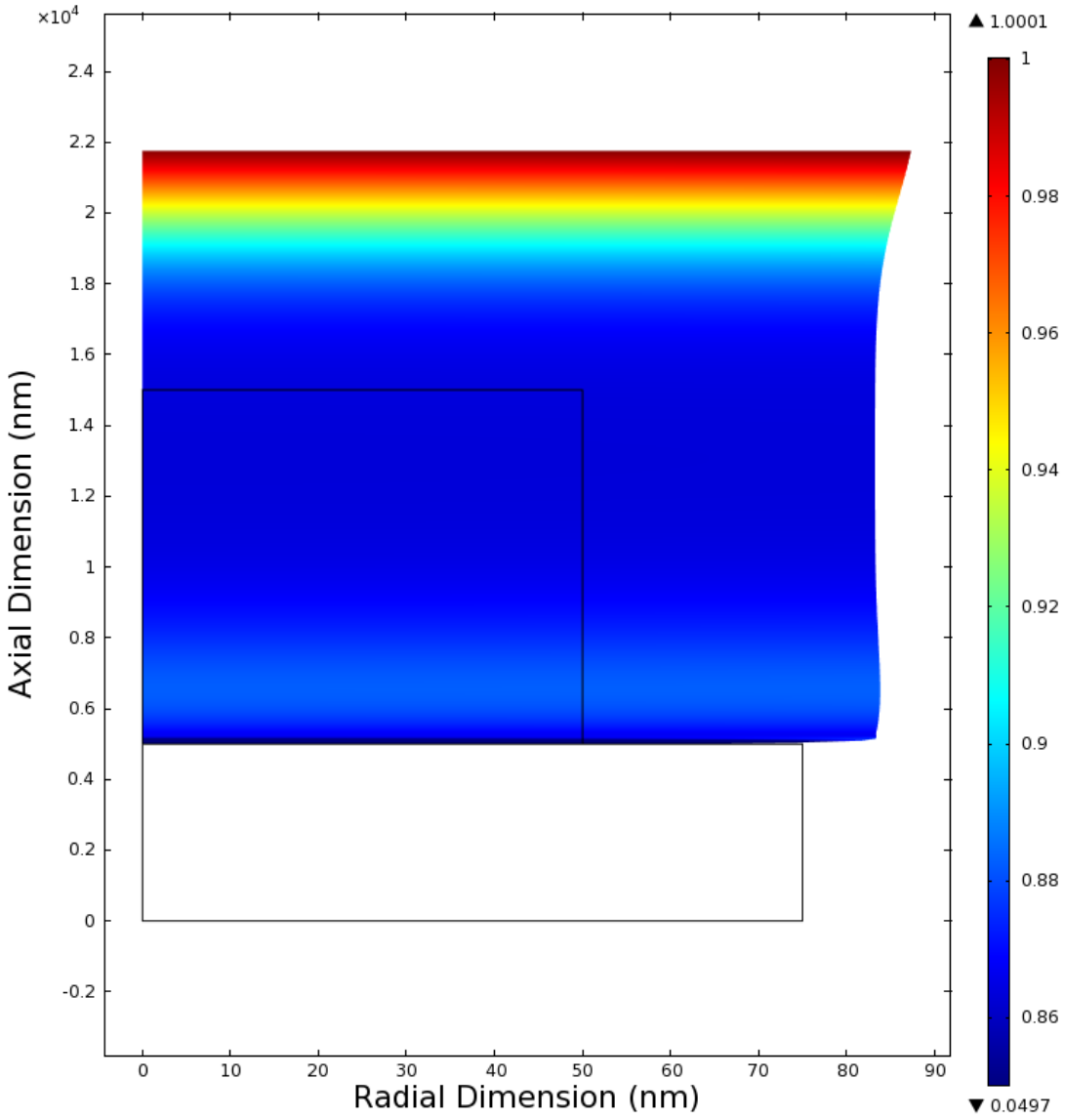

Fig. 3-2. Mole fraction profile of LiS, in the entire Si NW geometry

The lithiation rate in this simulation corresponds to a surface current density of 0.02 mA/cm^2 (initial) equivalent to a 1-h rate. The solid line in the plot marks the initial undeformed configuration of the Si NW anchored to the Cu CC substrate. In this study, the simulation was

terminated when the local mole fraction reached, x_{LiS}=1 anywhere within the electrode. As observed from the plot, the top surface of the Si NW is mass transfer limited and gets completely lithiated (x_{LiS}=1) while the bulk of the Si NW is still partially lithiated (x_{LiS} =0.86), which limits complete electrode utilization. The final deformed configuration of the Si NW shows the increase in the radial and axial dimensions of the Si NW due to the combination of chemical and elastic strains during lithiation. The top of the Si NW is expanded more, due to maximum lithiation in that region resulting in increased chemical strain, and regions very close to the Si NW/Cu CC interface (as shown in Fig. 3-3) are minimally expanded as the lithiation is limited due to the high stresses developed at the lithium blocking interface. Fig. 3-3 also shows the displacement of the Si NW/Cu CC interface from the initial configuration due to the interfacial stresses. Note, the Si NW region is pushed into the Cu CC region (z axis) by ~ 1 nm.

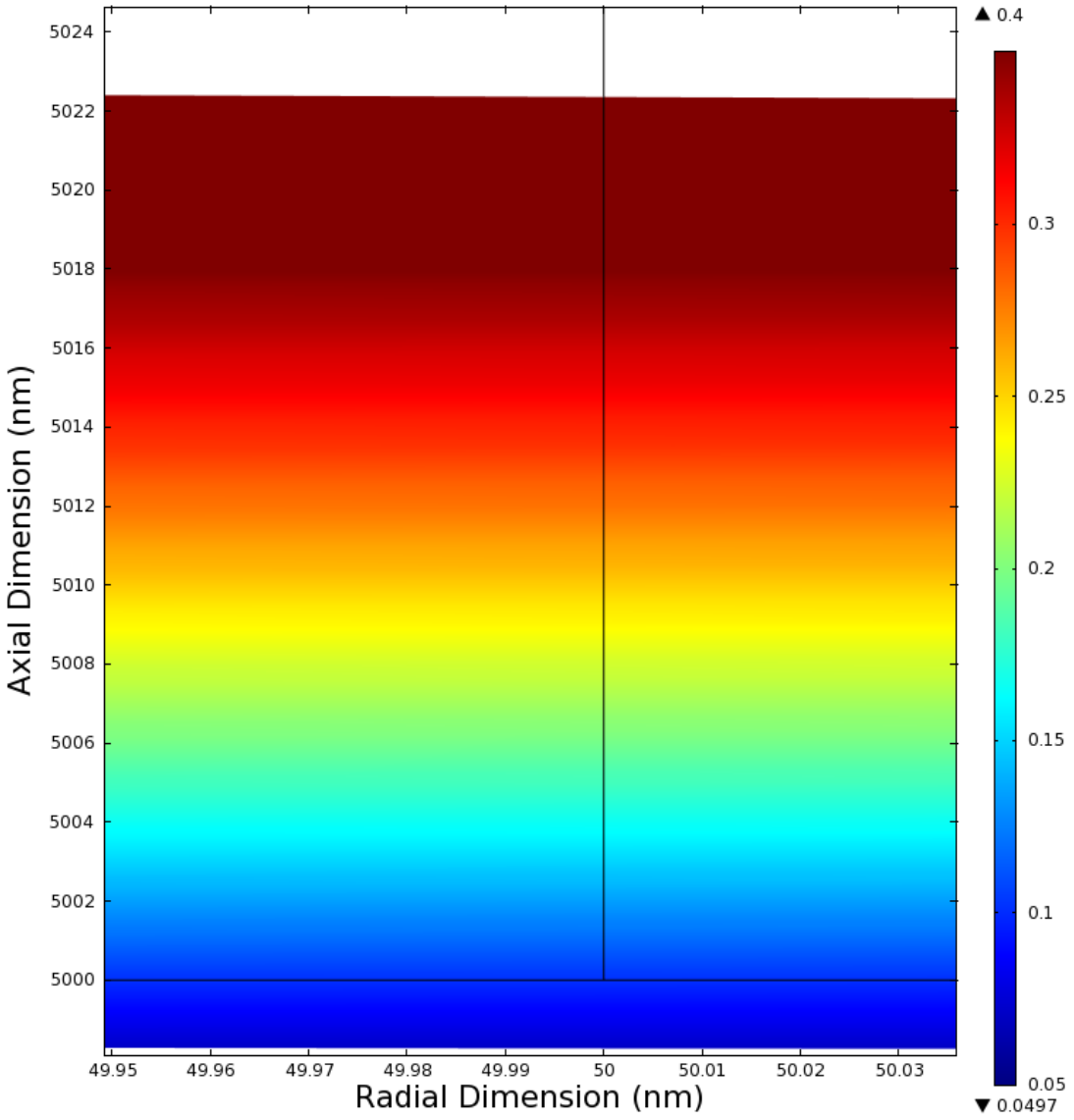

Fig. 3-3. Mole fraction profile of *LiS*, close to the Si NW/Cu CC interface

Fig. 3-4 shows a snap shot of the local volumetric strain distribution in the structure at the end of lithiation. The volumetric strain in the Si NW is non-uniform in the axial direction, especially at the top and the Si NW/Cu CC interface regions. In general, the local volumetric strain distribution in the Si NW domain correlates to the concentration distribution in Fig. 3-2, because the total volumetric strain, defined in Eq. (3.16) is predominantly determined by the chemical strain. In the Cu domain, the volumetric strains are purely elastic and mostly tensile, except at

regions close to the Si NW/Cu CC and away from the center where some regions are compressive.

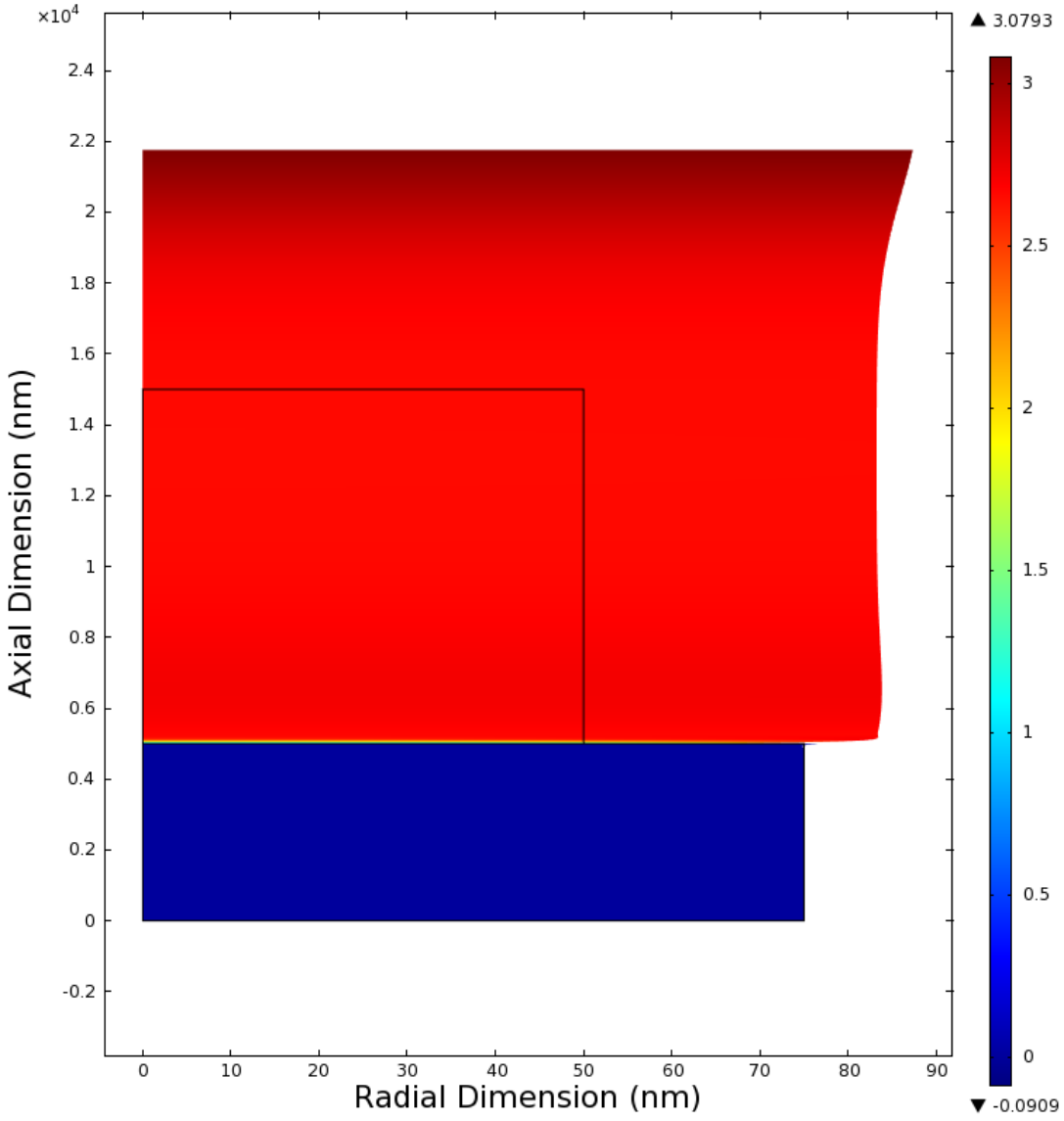

Fig. 3-4. Volumetric strain distribution in the Si NW/Cu CC at the end of lithiation

Fig. 3-5 compares the radial, tangential and axial stress components across the radius of the Si NW at different times during lithiation. The radial cut section in this plot is taken at half the initial height of the Si NW (z=H_{Cu}+H_{NW}/2) .

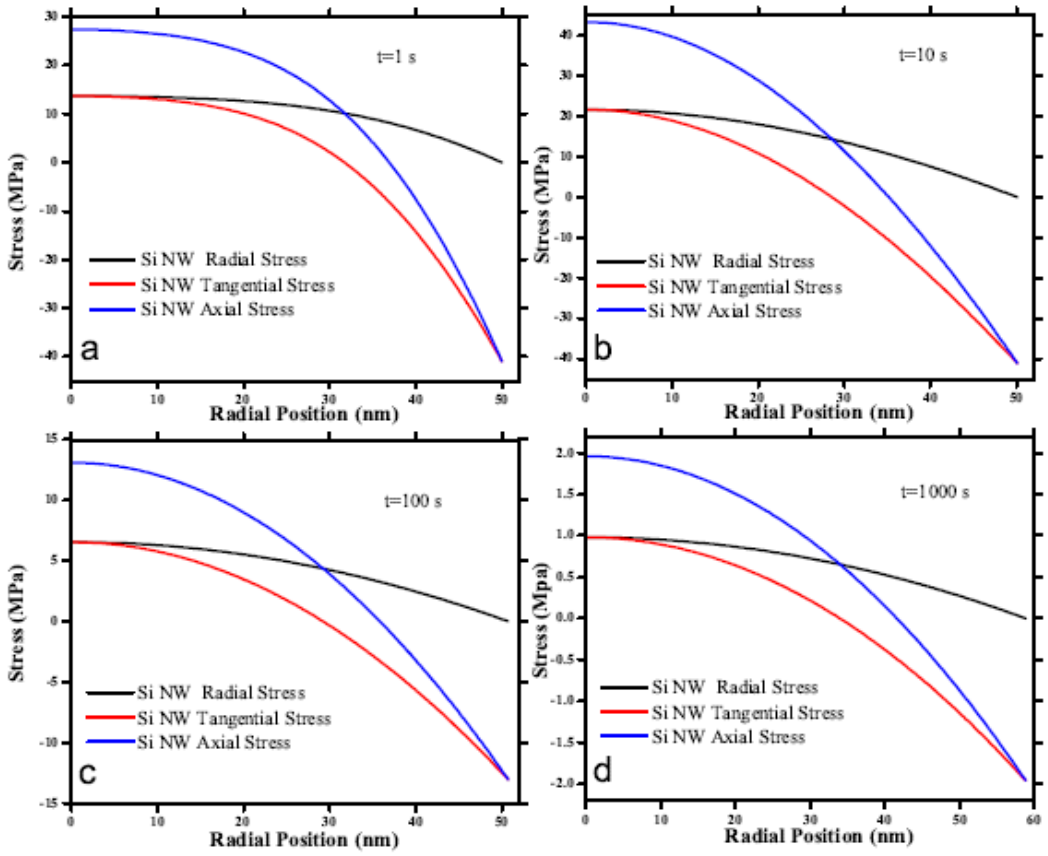

Fig. 3-5. Profiles of radial, tangential and axial stresses across the radius of Si NW at half of the height of Si NW at various times

Several features are observed in this plot; firstly the radial stress across the radius of the Si NW is always tensile, and is maximum at the center. This is because of the concentration build up at the surface which causes volumetric strain in the outer layers, which in turn radially pulls the inner layers to create the tensile stresses throughout the radius of the Si NW (as plotted in Fig. 3-5 a, b, c, & d). As a function of time, the maximum radial stresses (at the center of the Si NW) increases up to the first 10 s (~ 43 MPa observed at 10 s) and continuously decreases at longer times (~ 2 MPa observed at 1000 s). Also, the maximum tangential and the axial stresses follow a similar trend. This behavior is due to the competing effects of the chemical diffusion term and

the pressure induced term in Eq. (3.2) towards the overall flux of the species. At short times, the species flux is dominated by the chemical diffusion term, while at longer times, is dominated by pressure gradient term, resulting in reduced concentration gradients. Since the buildup of stresses is proportional to concentration gradients based on Eq. (3.16) and the force balance relations (Eqs. 3.20 & 3.21), the stresses decrease when the flux is dominated by the pressure gradients. Secondly, the tangential and the axial stresses are always compressive towards the outer surface and tensile towards the inner core. This behavior is due to the radial expansion of the outer surface which creates compressive strains in the tangential and the axial direction towards the outer surface, while the inner core is pulled outwards in all coordinates creating tensile stresses in the tangential and axial directions. Thirdly, at the center of the Si NW, the radial and the tangential stresses are equal, and the magnitude of the axial stress is twice the radial or tangential stress. This scenario is representative of a 1-d plane strain condition with infinitesimal deformation, where the condition $\sigma_{rr} = \sigma_{\theta\theta} = \sigma_{zz}/2$ is satisfied at the center (r=0) in cylindrical coordinates. This behavior suggests that far away from the Si NW/Cu CC interface, the stress behavior is similar to a 1-d plane strain condition.

Fig. 3-6 compares the radial, tangential and axial stress components close to the Si NW/Cu CC interface on the Si NW side.

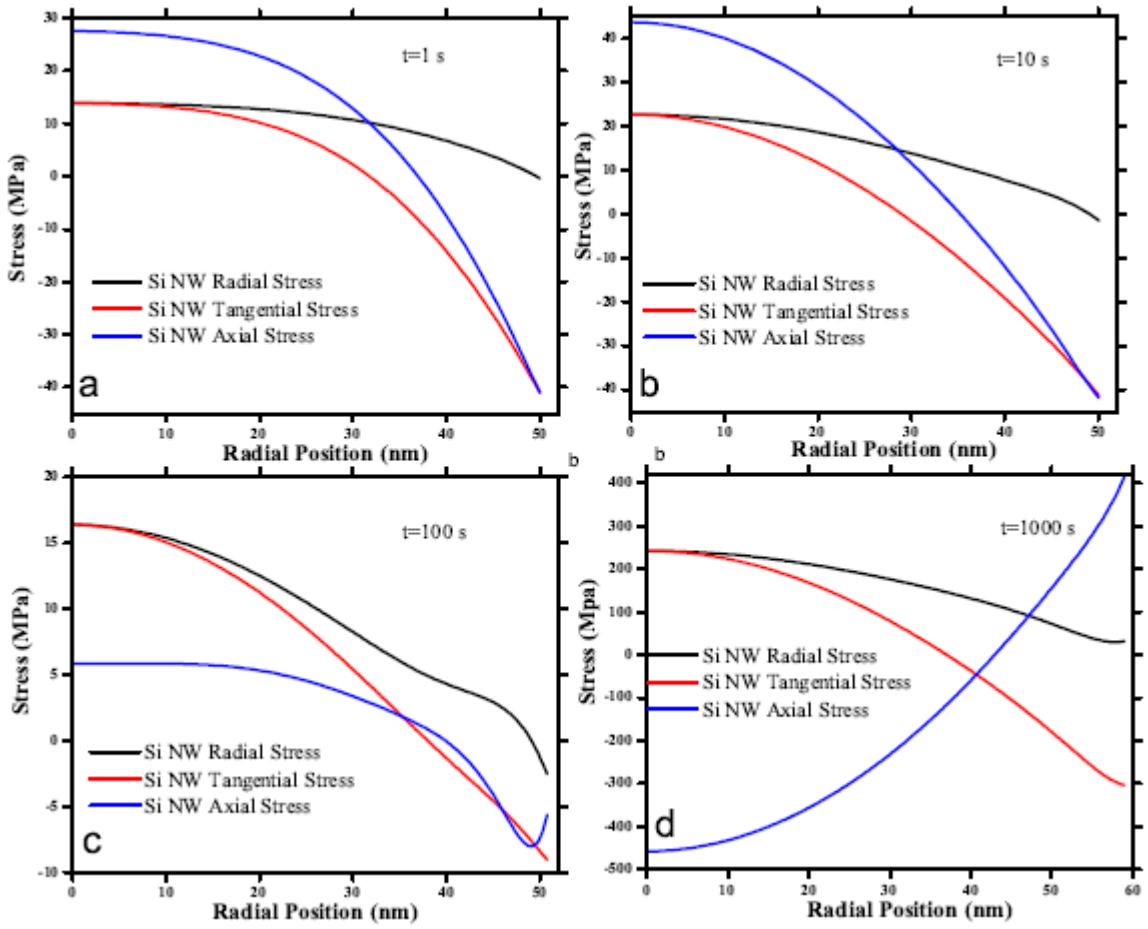

Fig. 3-6. Profiles of radial, tangential and axial stresses across the radius of Si NW, close to the Si NW/ Cu CC interface at various times

At short times, t=1 and t=10s, the stress profiles across the radius matched quantitatively with the stresses profiles across the radius in the center region of the Si NW(as discussed in the earlier section), while at longer times the presence of the constraint (substrate) significantly alters the stress profiles. At 100s, the radial and tangential stress profiles are similar to short time behavior, however the axial stress becomes less tensile at the center and at longer times (t=1000s) the axial stress reverses its general trend and becomes compressive in the inner part and tensile at the outer part. Furthermore, the magnitudes of all the stress components increase considerably and are in the range of 250 - 500 MPa. This is possibly because of the constant lithiation flux

(imposed by the boundary conditions) in the regions close to the interface, while simultaneously the interface is also being constrained by the Cu substrate resulting in the large tensile and compressive stress regions. These enormous stress components could potentially cause the Si NW structure to yield or fracture in these regions close to the interface.

Fig. 3-7 shows the evolution of maximum stress for each component with time during lithiation of the Si NW.

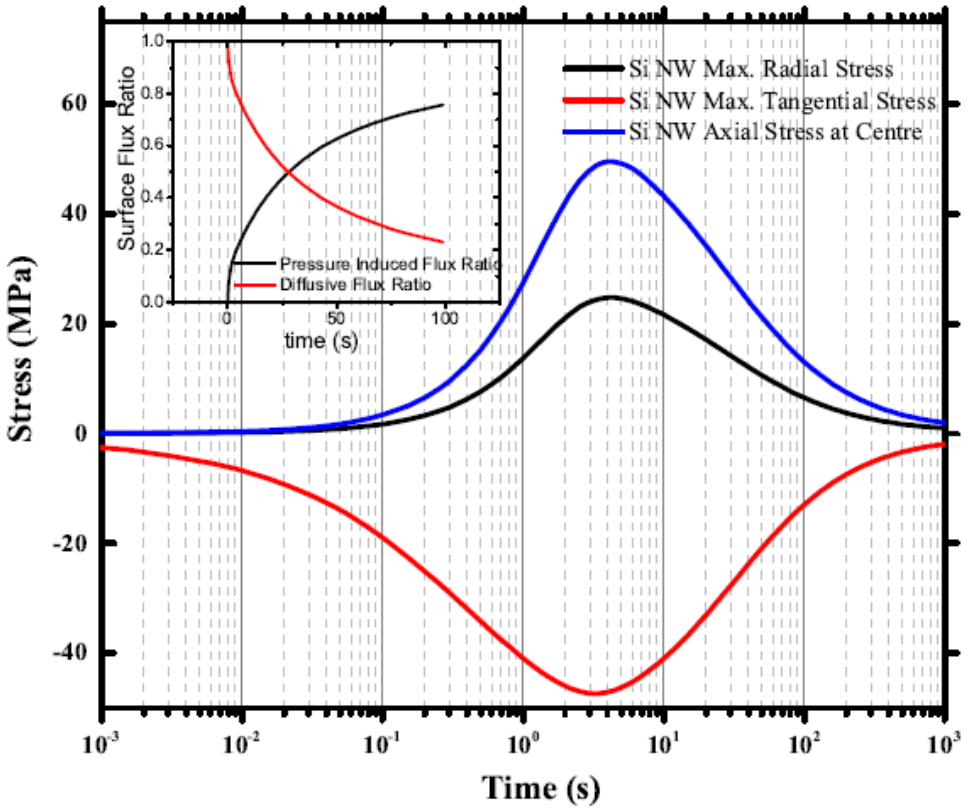

Fig. 3-7. Evolution of maximum radial stress, maximum tangential stress and maximum axial stress with time at half the height of the nanowire

In this plot, the z co-ordinate is halfway through the initial height of Si NW, i.e. $z=H_{Cu}+H_{NW}/2$ and the r co-ordinate is chosen corresponding to where the maximum value of stress in each component occurs. The maximum radial and axial stresses are tensile and always occur at the center ($r=0$) of the Si NW, while the maximum tangential stresses are compressive and occurs at

the outer surface of the Si NW, i.e. r=R_{NW} (t). For the parameters used in the simulation, the values for the stress components peak at ~ 4s and decreases subsequently. As explained in the earlier section, this behavior is due to the competing effects of the chemical diffusion term and the pressure induced term in Eq. (3.2) towards the overall flux of the species. The plot in the subset of Fig. 3-7 clearly shows the shift from the diffusion dominated transport at short times, to pressure driven transport at longer times.

3.6 Effect of lithiation rate

Figs. 3-8 and 3-9 show the effect of lithiation rate on the evolution of the maximum radial and tangential stresses with time. Here C rate corresponds to a 1-h rate equivalent to an initial current density of 0.02 mA/cm^2.

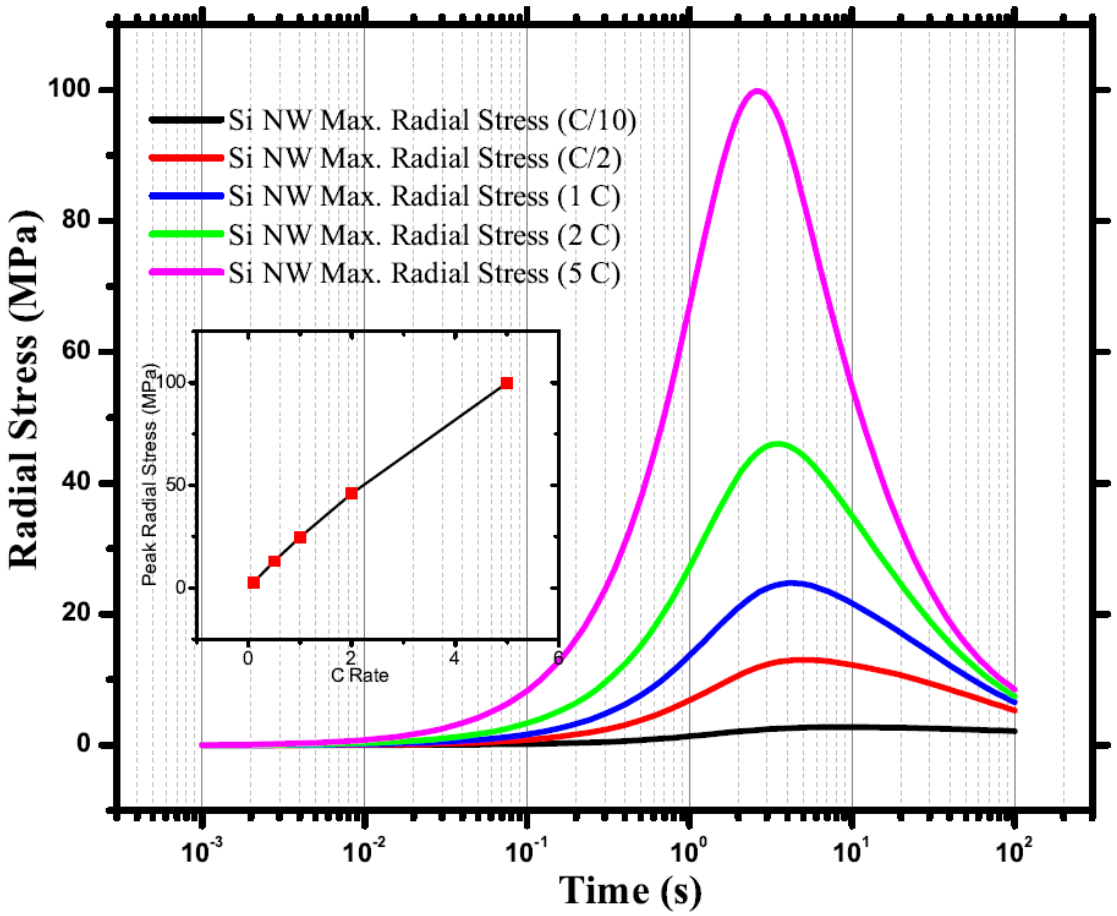

Fig. 3-8. Evolution of maximum radial stresses as a function of lithiation rates

The inset plots in Figs. 3-8 and 3-9 show a linear increase in maximum radial and tangential stresses with lithiation rate. Also at higher lithiation rates, the peak maximum stresses also occur at shorter times as seen from the shift in the peak towards the left. This behavior suggests possibility for mechanical fracture at very short times under high current conditions, typically seen in hybrid electric vehicle, fast charge or regenerative braking applications, despite the nanoscale dimensions of the electrode. The occurrence of peak maximum stresses at shorter times at higher lithiation rates, could also be explained through the interplay between the diffusive and the pressure induced flux. At higher rates, large concentration gradients (due to chemical diffusion) are established at shorter times, creating a large stress field at the surface.

Consequently, a larger pressure gradient is built up, which then dominates the species flux, compared to the chemical diffusion mode in the bulk of the Si NW.

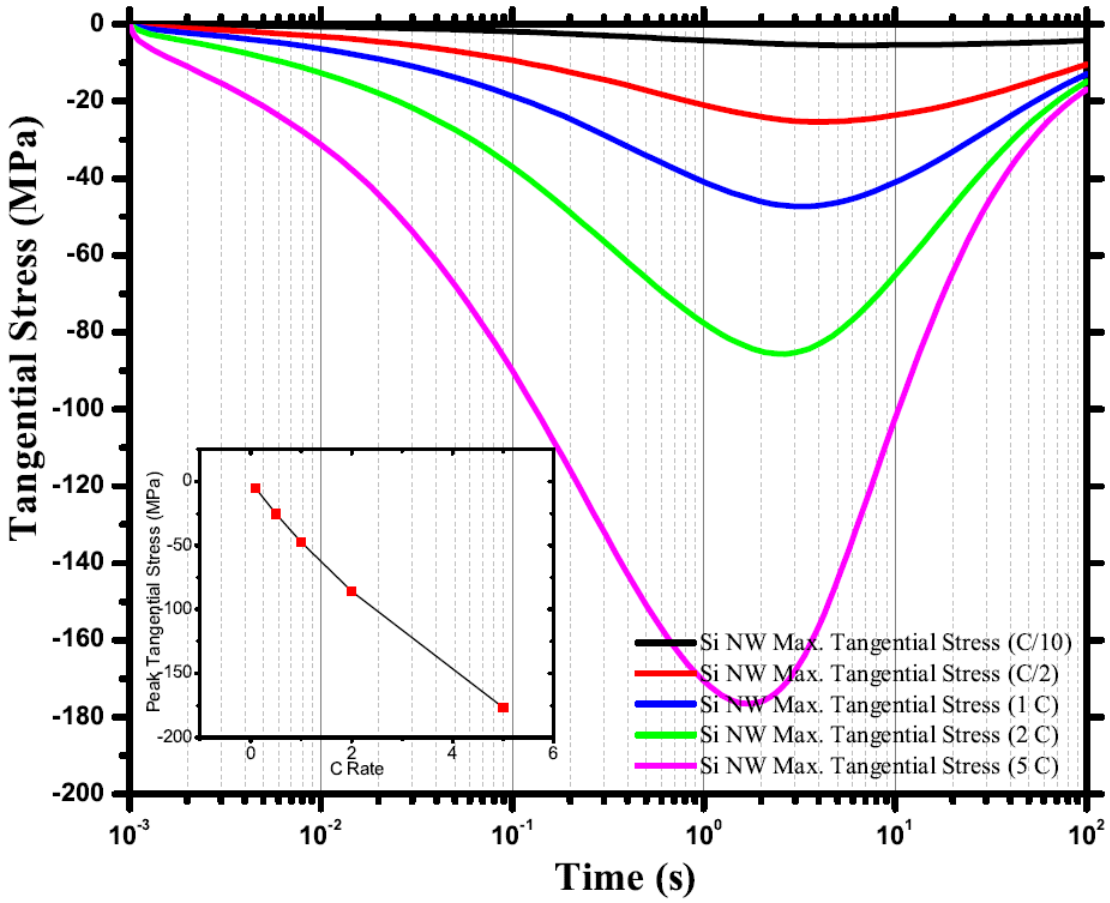

Fig. 3-9. Evolution of maximum tangential stresses as a function of lithiation rates

3.7 Effect of Si NW radius

Figs. 3-10 and 3-11 show the effect of Si NW radius on the evolution of maximum radial and tangential stresses with time for 1-h lithiation rate. The 1-h lithiation rate (C rate) for the Si NW radii of 50, 100, 200, 300 and 500 nm corresponds to a current density of 0.0208, 0.0415 and 0.0826, 0.0826, and 0.1251 mA/cm^2 respectively.

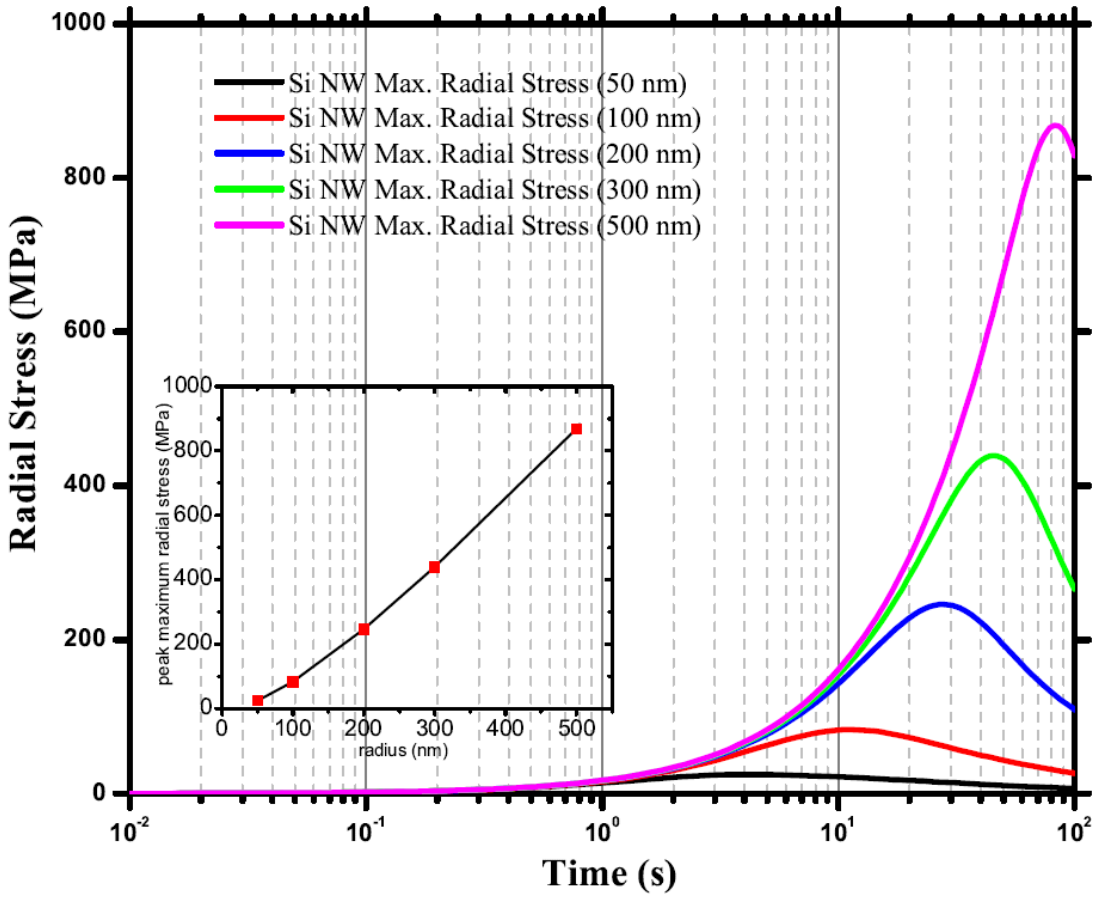

Fig. 3-10. Evolution of maximum radial stresses as a function of radius of the Si NW

The increased surface current density explains the higher radial and tangential stresses observed in structures with larger radii. Also, the increased current densities (for larger radius), shift the peak maximum stresses to longer times, which is contrary to the effect observed at higher current densities for constant radius (Figs. 3-10 and 3-11). This behavior suggests that the increase in the current density (for larger radius structures) is not large enough to counter the longer diffusion length, which in turn delays the time for maximum stresses to develop. Consequently, the contribution from pressure induced flux takes a longer time to offset the diffusion dominated flux for nanowires with larger radius. Further, since the stress values for particles of larger radius are at any time higher than that for the particles with smaller radius, the latter is preferred especially

for high rate applications. While smaller particles are not preferred due to lower compressed density and higher exposed surface area to the electrolyte, they clearly offer an advantage from a mechanical stand point. Design of optimal particle size should however be considered based on the energy and power requirements for specific applications.

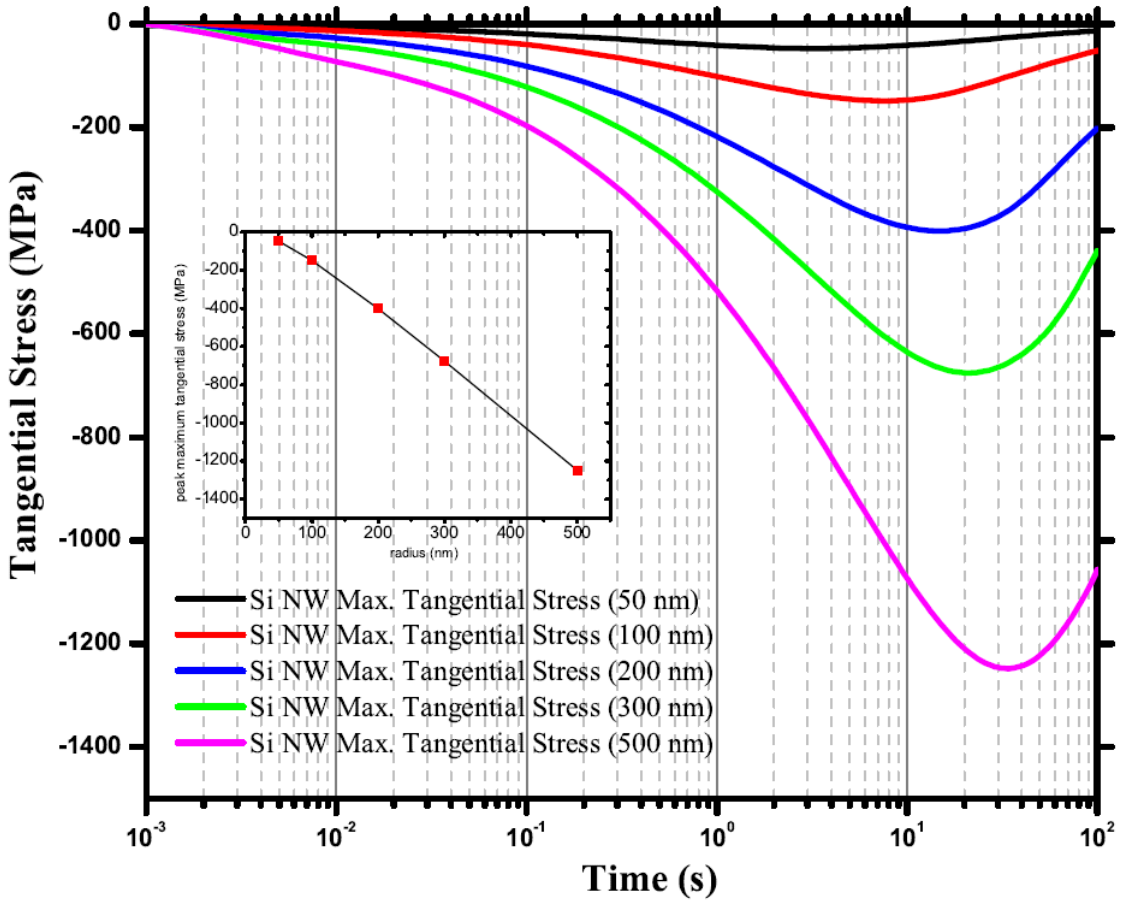

Fig. 3-11. Evolution of maximum tangential stresses as a function of radius of the Si NW

List of Symbols

c = concentration of species, c_S, c_{LiS} or c_T, mol/m^3

N_{LiS} = flux of species c_S, or c_{LiS}, mol/m^3

x = mole fraction of species, x_S or x_{LiS}

Δz = insertion coefficient of Li in $Li_{\Delta z}Si_{\frac{1}{\Delta x}}$

Δx = maximum number of moles of Li that can alloy per mole of Si

t = time, s

r = radial coordinate, m

θ = tangential coordinate, deg

z = axial coordinate, m

v = velocity of species, v_S or v_{LiS}, m/s

$v^{\diamond}$ = molar average velocity, m/s

$D_{LiS,S}$ = binary diffusion coefficient of Li in LiS, m^2/s

α_{LiS} = thermodynamic factor

M = molar mass of species, M_S or M_{LiS}, g/mol

F = Faraday's constant, C/g.equiv

R = universal gas constant, J/mol.K

T = temperature, K

s_i = stoichiometric coefficient

$\dot{V}$ = partial molar volume of species, $\dot{V}_{LiS}$ or $\dot{V}_S$, m^3/mol

ξ = expansion factor

ρ = density of $Li_{\Delta z}Si_{\frac{1}{\Delta x}}$, g/m^3

p = thermodynamic pressure, N/m^2

u = displacement vector field

u, v, w = dispacement in r, θ and z coordinates, m

n = unit outward normal vector, m

i_{app} = current density related to outer surface of the Si NW, A/m^2

R_{NW} = radius of the nanowire, a function of time, m

H = height of the nanowire or Cu current collector, m

τ = stress tensor matrix

σ = stress components of stress tensor matrix, N/m^2

E = strain tensor matrix

ε = strain components of strain tensor matrix

λ,μ = Lame's constants, N/m^2

E = Young's modulus, N/m^2

ν = Poisson's ratio

Chapter 4

Efficient reformulation of solid-phase diffusion in electrochemical-mechanical coupled models for lithium-ion batteries- effect of intercalation induced stresses

4.1 Introduction

Electrochemical power sources are expected to play a vital role in the future in automobiles, power storage, military, mobile, and space applications. Lithium-ion chemistry has been identified as a good candidate for high-power/high-energy secondary batteries. Progress has been made towards modeling and understanding of lithium-ion batteries using physics based first principles models which typically solve electrolyte concentration, electrolyte potential, solid-state potential and solid-state concentration in the porous electrodes [10,79] as well as electrolyte concentration and electrolyte potential in the separator. These models are represented by coupled nonlinear partial differential equations (PDEs) in 1-2 dimensions, include physics such as transport phenomena, electrochemistry and thermodynamics and are typically solved numerically which require few minutes to hours to simulate depending on the solver and schemes used.

Currently, silicon, germanium etc. are being pursued as potential anode materials for lithium-ion batteries owing to their high gravimetric (mAh/g) and volumetric capacities (mAh/L) compared

to graphite, for high energy and high power applications of the future [65] . During intercalation/de-intercalation these materials exhibit significant stress development as well as volume and density changes [40,79,82,86]. The concentration gradient inside the particle is affected due to the stress generated within the particle and cannot be captured solely by simple Fickian diffusion. Therefore, pressure induced diffusion must be included when solving for solid phase diffusion in the pseudo radial dimension r within the particle [40,79,82,86]. One of the major difficulties in the electrochemical engineering models is the inclusion of solid phase diffusion in a second dimension r which increases the complexity of the model as well as the computation time/cost to a great extent. The inclusion of pressure induced solid phase diffusion physics not only increases the complexity of the model but significantly increases the computational cost/time as it increases the number of equations to be solved in the pseudo r dimension. For every point in x for the macro-scale, pressure induced solid phase equations have to be solved in r and the number of equations depends on the discretization scheme chosen for the r dimension. Traditional discretization approaches, such as finite difference (FD), when used in the second pseudo dimension r increase the number of equations by many folds thereby making simulation of the system slower and complex.

This chapter presents a method for computationally efficient representation for pressure induced diffusion in the solid phase. The chapter discusses briefly about the model used for the study of pressure induced diffusion within the electrode particle and the simulation procedure adopted. Then, two computationally efficient representations for pressure induced solid phase diffusion are discussed. At first, a reformulation method is discussed based on the parabolic profile approximation for solid phase diffusion [96] which approximately captures the behavior for low rates and long times. Then, a robust solid phase reformulation technique based on a mixed order

finite difference (MFD) method with optimal node spacing is introduced [97]. Results from the parabolic profile approximation are compared with results from the converged solution with 45 internal node points (referred to as full order numerical solution in this chapter). Results from the MFD technique are also compared with the full-order finite difference solutions for both galvanostatic charging conditions and for current varying as a function of time which suggest that reformulation can be done without compromising on accuracy for a wide range of operating conditions.

4.2 Model equations, boundary conditions and numerical simulation

This chapter deals with a one dimensional (1D) continuum scale model that includes pressure induced diffusion in a spherical particle and predicts the stress distribution and volume expansion during charging. This is an important phenomenon to study especially for high capacity electrode materials because during lithium insertion volume expansion of the particle results in strain differential between the inner and outer regions which increases the rate of insertion and therefore develops stress within the particle. This model has been presented in details in Christensen et.al. [40] The model accounts for lithium transport, solid mechanics, lithium transport-induced stresses, and volume expansion. Next the model equations and boundary conditions in non-dimensionalized form are briefly reviewed [40]. For the model, the electrode material is treated as a binary system i.e. a host material occupied with lithium (*LiS*) and pure host material (*S*). Table 4-1 presents the dimensionless independent and dependent variables in the system along with their definitions. The equations and boundary conditions for the model were non-dimensionalized accordingly and are presented in Table 4-2. Therefore, there are 8 spatial and time dependent variables along with the moving boundary, $\chi(\tau)$ (particle radius).

Independent Variables	Definition
τ	Dimensionless time
ξ	Dimensionless radial distance w.r.t. moving boundary
Dependent Variables	**Definition**
$x_{LiS}(\xi,\tau)$	Mole fraction of species *LiS*,
$u(\xi,\tau)$	Lattice displacement
$N_{LiS}(\xi,\tau)$	Flux of species *LiS*
$N_S(\xi,\tau)$	Flux of species *S*
$\theta(\xi,\tau)$	Total concentration
$\sigma_r(\xi,\tau)$	Stress in radial direction
$\sigma_t(\xi,\tau)$	Stress in tangential direction
$\pi(\xi,\tau)$	Thermodynamic pressure
$w(\xi,\tau)$	Dummy variable used to simplify the equations
$\chi(\tau)$	Particle radius

Table 4-1. List of dimensionless independent and dependent variables for the model

The system of governing equations and boundary conditions generates a set of highly coupled and non-linear equations.

Sr. No	$\xi = 0$	$0 < \xi < 1$	$\xi = 1$	Comments
1	$N_{LiS}(\xi,\tau) = 0$	$\frac{\partial}{\partial\tau}\left(\theta(\xi,\tau)x_{LiS}(\xi,\tau)\right) - \xi\left(\frac{d}{d\tau}\chi(\tau)\right)\frac{\partial}{\partial\xi}\left(\theta(\xi,\tau)x_{LiS}(\xi,\tau)\right) + \frac{\frac{\partial}{\partial\xi}\left(\xi^2 N_{LiS}(\xi,\tau)\right)}{\chi(\tau)\xi^2} = 0$		Mass balance for species *LiS* and *S*
2	$N_S(\xi,\tau) = 0$	$\frac{\partial}{\partial\tau}\left(\theta(\xi,\tau)\left(1-x_{LiS}(\xi,\tau)\right)\right) - \xi\left(\frac{d}{d\tau}\chi(\tau)\right)\frac{\partial}{\partial\xi}\left(\theta(\xi,\tau)\left(1-x_{LiS}(\xi,\tau)\right)\right) + \frac{\frac{\partial}{\partial\xi}\left(\xi^2 N_S(\xi,\tau)\right)}{\chi(\tau)\xi^2} = 0$		
3	$N_{LiS}(\xi,\tau) = x_{LiS}(\xi,\tau)\left(N_{LiS}(\xi,\tau) + N_S(\xi,\tau)\right) - \frac{\theta(\xi,\tau)}{\chi(\tau)}\left(\begin{array}{l}\alpha\frac{\partial}{\partial\xi}x_{LiS}(\xi,\tau) + \\ ex_{LiS}(\xi,\tau)\left(1+\frac{\omega}{x_{\max}} - \frac{M_b}{\theta(\xi,\tau)\left(x_{LiS}(\xi,\tau)M_b + 1 - x_{LiS}(\xi,\tau)\right)}\right)\frac{\partial}{\partial\xi}\pi(\xi,\tau)\end{array}\right)$		$\chi(\tau)^2\left(N_{LiS}(\xi,\tau) - \theta(\xi,\tau)x_{LiS}(\xi,\tau)\frac{d}{d\tau}\chi(\tau)\right) = -I$	Stefan-Maxwell equation for flux of *LiS*. The surface current flux condition is used at $\xi = 1$.
4	$\theta(\xi,\tau) = \left(1+\frac{\omega x_{LiS}(\xi,\tau)}{x_{\max}}\right)^{-1}\left(\mathrm{e}^{\frac{\sigma_r(\xi,\tau)+2\sigma_t(\xi,\tau)-3\pi(\xi,\tau)}{1+\nu}}\right)^{-1}$			Total concentration of

				species as a function of of mole fractions and stresses
5	$u(\xi,\tau)=0$	$\frac{N_{LiS}(\xi,\tau)+N_S(\xi,\tau)}{\theta(\xi,\tau)}=\frac{\frac{\partial}{\partial\tau}u(\xi,\tau)-w(\xi,\tau)\xi\frac{d}{d\tau}\chi(\tau)}{1-w(\xi,\tau)}$	$\frac{N_{LiS}(\xi,\tau)+N_S(\xi,\tau)}{\theta(\xi,\tau)}=\frac{\partial}{\partial\tau}u(\xi,\tau)$	The relationship between the total flux of the species and radial displacement
6	$\sigma_r(\xi,\tau)=w(\xi,\tau)-\frac{w(\xi,\tau)^2}{2}$	$\sigma_r(\xi,\tau)=(1-\nu)\left(w(\xi,\tau)-1/2\left(w(\xi,\tau)\right)^2\right)+2\nu\left(\frac{u(\xi,\tau)}{\xi\chi(\tau)}-1/2\frac{\left(u(\xi,\tau)\right)^2}{\xi^2\left(\chi(\tau)\right)^2}\right)$		Hooke's Law for radial and tangential stresses. At center, both are equal.
7	$\sigma_t(\xi,\tau)=w(\xi,\tau)-\frac{w(\xi,\tau)^2}{2}$	$\sigma_t(\xi,\tau)=\nu\left(w(\xi,\tau)-1/2\left(w(\xi,\tau)\right)^2\right)+\frac{u(\xi,\tau)}{\xi\chi(\tau)}-1/2\frac{\left(u(\xi,\tau)\right)^2}{\xi^2\left(\chi(\tau)\right)^2}$		

8	$\frac{\partial}{\partial \xi}\pi(\xi,\tau)=0$	$\frac{\partial}{\partial \xi}\left(\sigma_r(\xi,\tau)-\pi(\xi,\tau)\right)+2\frac{\sigma_r(\xi,\tau)-\sigma_t(\xi,\tau)}{\xi}=0$	$\sigma_r(\xi,\tau)-\pi(\xi,\tau)=0$	Momentum balance. Existence of free surface at $\xi=1$.
9	$w(\xi,\tau)=\frac{\frac{\partial}{\partial \xi}u(\xi,\tau)}{\chi(\tau)}$			Dummy variable
10	$\frac{d}{d\tau}\chi(\tau)=\frac{\partial}{\partial \tau}u(\xi,\tau)$			Moving boundary

Table 4-2. Model equations and boundary conditions in dimensionless form

A total of 45 internal node points in the radial direction *r* were used to achieve a converged solution consistent with the simulation results reported earlier by Christensen et. al. [40] An absolute error of 10^{-10} was set for the numerical integration accuracy in time. The simulations were terminated as the surface *LiS* mole fraction reached the maximum value of $x_{\max}$ .The set of dimensionless parameters used for simulation is given in Table 4-3. The dimensionless total current I for galvanostatic conditions is calculated based on the C rate and $x_{\max}$. Simulations for both high and low rates and time varying currents were performed.

Dimensionless Parameter	Value
ω, fractional expansivity	0.08
e, elatic modulus	399.5
M_b, molar mass ratio	1.09362
$x_{\max}$, maximum mole fraction for lithiation	0.6
D, ratio of diffusive to elastic energy	$8.09e-23$

Table 4-3. List of dimensionless parameters used for simulation

When converted to finite difference form, the number of equations equals $N_{\text{var}}(N+2)+1$ where N_{var} is the number of variables in the system and N is the number of internal node points in r. The time dependent moving boundary provides an additional ordinary differential equation (ODE). For example, when N = 1 internal node point is used in *r*, it results in 25 differential algebraic equations (DAEs) of which 4 are of index 2. Higher index DAEs are difficult to solve compared to pure ODEs and DAEs of index 1 [98]. Using adaptive solvers in time gives an advantage in numerical simulation in terms of efficiency, but also requires additional robustness on the choice of DAE solvers. Discussion of the difficulty of index-2 DAEs is beyond the scope of the paper.

4.3 Reformulation of pressure induced solid phase diffusion: parabolic profile approximation

A first attempt to approximate the model is to assume a parabolic polynomial profile for spatially dependent variables. In the past, [34,96] this method has shown reasonable accuracy and has been used in the macroscopic P2D battery model [10]. This approximation method for pressure induced solid phase diffusion is based on assuming profiles inside the particle as parabolic in nature and generating volume averaged equations. This method has been discussed for a radial Fickian diffusion equation previously by other authors [34,99,100]. The following section describes the step by step derivation of the approximate profiles and volume averaged equations based on this method. For demonstration purposes, we choose a representative variable from the model e.g. the flux of species LiS. Therefore, assuming parabolic profile we can write,

$$N_{LiS}(\xi,\tau) = a1_0(\tau) + a1_1(\tau)\xi + a1_2(\tau)\xi^2 \tag{4.1}$$

All the other spatial variables of the system can be expressed with similar profiles. For the simulation of such a system, we need to solve the time dependent coefficients which appear in the assumed profiles. As a first step, to eliminate one of the coefficients, a volume averaged quantity is introduced into the system. For the demonstration case considered here, $\overline{N}_{LiS}(\tau)$ is the volume averaged flux of species LiS which can be represented by

$$\overline{N}_{LiS}(\tau) = \int_0^1 3\xi^2 \left(N_{LiS}(\xi,\tau)\, d\xi \right. \tag{4.2}$$

Replacing Eq. 4.1 in Eq. 4.2 and performing the integration, the time dependent coefficient $a1_2(\tau)$ can be removed in terms of the volume averaged quantity and other coefficients as

$$a1_2(\tau) = \frac{5}{3}\left(\overline{N}_{LiS}(\tau) - \frac{3}{4} a1_1(\tau) - a1_0(\tau) \right) \tag{4.3}$$

Replacing this value in Eq. 4.1, the parabolic profile equation for $N_{LiS}(\xi,\tau)$ becomes

$$N_{LiS}(\xi,\tau) = a1_0(\tau) + a1_1(\tau)\xi + \frac{5}{3}\left(\overline{N}_{LiS}(\tau) - \frac{3}{4} a1_1(\tau) - a1_0(\tau) \right)\xi^2 \tag{4.4}$$

Now there are 2 time dependent coefficients along with the volume averaged quantity. The boundary conditions are to be used for eliminating the time dependent coefficients. Using the boundary condition for $N_{LiS}(\xi,\tau)$ at $\xi = 0$, the coefficient $a1_0(\tau)$ can be eliminated and the parabolic profile can be rewritten as

$$N_{LiS}(\xi,\tau) = a1_1(\tau)\xi + \frac{5}{3}\left(\overline{N}_{LiS}(\tau) - \frac{3}{4} a1_1(\tau) \right)\xi^2 \tag{4.5}$$

The remaining time dependent coefficient is eliminated by using the boundary condition at $\xi = 1$. It has to be noted that due to the non-linearity and implicit nature of the system, the application of boundary condition at $\xi = 1$ does not generate explicit expressions for the coefficients to be directly incorporated into the parabolic profiles. Therefore, these boundary conditions were solved as a coupled set of equations within the final system. Finally, the volume averaged quantity was evaluated by volume averaging the entire governing equation. In general, this step can be mathematically represented as

$$\int_0^1 3\xi^2 \left(GE(\xi,\tau) \right) d\xi = 0 \tag{4.6}$$

where $GE(\xi,\tau)$ is any governing equation of the system. Direct analytical integration was performed in ξ for most of the governing equations except for some (Sr. No. 3, 4 & 5 from Table 4-2). Numerical integration in ξ was performed for these particular equations using

Simpson's rule. Simulations were performed with an increasing number of integration points to verify the convergence of the solution. These mathematical steps are performed for all spatially varying quantities to generate the reformulated parabolic profile model for the simulation of pressure induced diffusion within the electrode particle.

The advantage of this method of reformulation is that it reduces the number of state variables thereby reducing number of equations which facilitates faster simulation. This method is accurate for low rates and long times. After the reformulation technique is applied, the equations are only functions of dimensionless time τ and can be solved using a time adaptive solver (DASKR) [53] with proper initialization.

The model for pressure induced diffusion has 8 dependent variables varying spatially and in time (Table 4-1). The moving radius is tracked by $\chi(\tau)$ which is a time dependent variable. Therefore, if discretized with N=1 internal node point (FD method), the total number of states is equal to $(8*3)+1=25$. For the parabolic profile, the general representation of a dependent variable is given by

$$f(\xi,\tau) = fl_0(\tau) + fl_1(\tau)\xi + fl_2(\tau)\xi^2 \tag{4.7}$$

Therefore, there are three time dependent coefficients per variable which generates 8 x 3 = 24 states for the model discussed in this paper. Taking the moving boundary variable into account, the reformulated parabolic profile pressure induced diffusion model generates 25 state variables before mathematical manipulation which is exactly similar to the case when the original model is discretized with N=1 internal node point. Therefore, it is logical to compare the parabolic profile approximation results with full-order numerical solution of the model discretized using FD method for N=1 internal node point. The dimensional surface concentration $c_{surf}(x,t)$ is the

quantity of interest because it is required by the macro-homogeneous battery model to keep track of the local current density as a function of time. Therefore, results for surface concentration are compared in Fig. 4-1 from the full-order solution and the reformulated model for a C/3 rate. Note that a low rate was chosen for this case as the parabolic profile approximation is likely to be valid only for low rates. The converged numerical solution with N=45 internal node points was chosen as the benchmark for the comparison of the results.

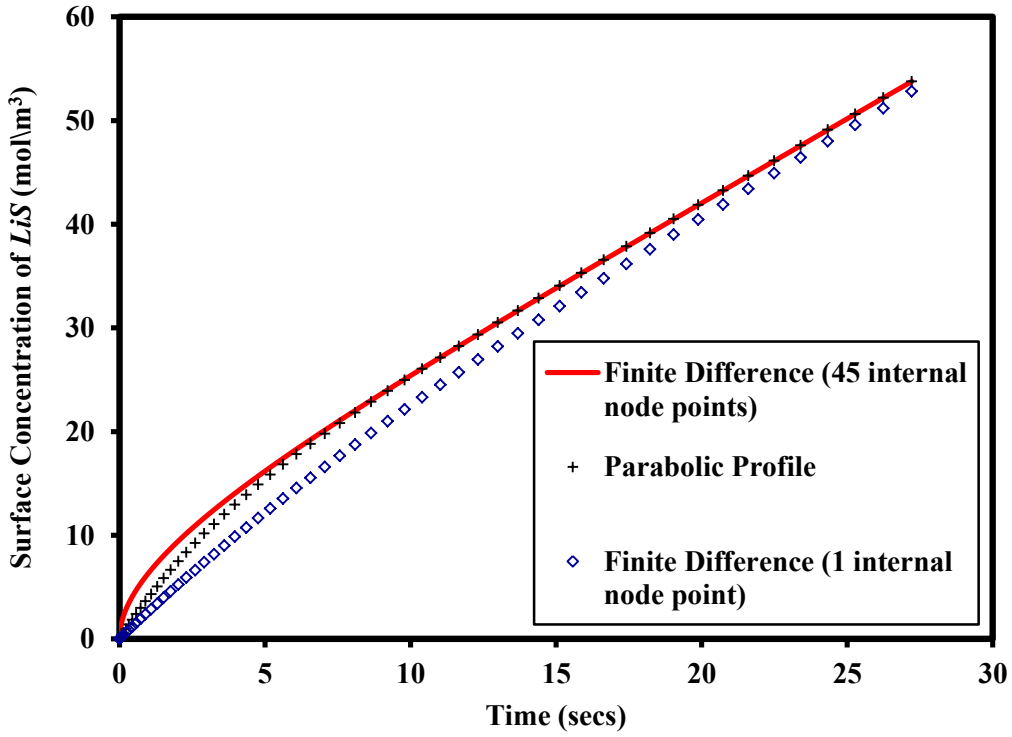

Fig. 4-1. Comparison of parabolic profile method with finite difference numerical solution with 45 and 1 equally spaced internal node points

The results of Fig. 4-1 clearly show that at short times i.e. at the start of lithiation of electrode particle, the parabolic profile approximation predicts erroneous results compared to the numerical solution with N=45 internal nodes. But the parabolic profile predictions become

reasonable at longer times. This behavior is observed because the model fails to capture the effect of the moving front depicted by steep concentration gradients at short times when lithiation initiates [40]. As time increases and lithiation continues, the effect of pressure induced diffusion decreases and the parabolic profile predicts surface concentration $c_{surf}(x,t)$ with reasonable accuracy. As expected, the FD simulation with N=1 node point gives erroneous results for both short and long times. Therefore, if we are only concerned about the accuracy of surface concentration at long times and very low rates, then the parabolic profile approximation is a good choice as it has significantly less number of states compared to the FD simulation with 45 internal node points (25 states compared to 477 states) which facilitates a reduction in the computational cost/time. In the next section, the mixed finite difference method with optimal node spacing is introduced which is robust and accurate for both short and long times. Note that volume averaging provides good enough results and conserves mass and charge at long times.

4.4 Reformulation of pressure induced solid phase diffusion: mixed finite difference approach with unequal node spacing

Finite difference method is one of the most widely used numerical techniques to solve ordinary and partial differential equations. Use of finite difference method has been the first choice for solving first principles based lithium-ion battery models. However, for full order battery models, when dealing with a second radial dimension r for discretization, the number of equations increases by many folds, thereby increasing the computational cost [4,34,97]. As mentioned previously, over 40 internal node points in r are needed to obtain a converged solution for simulation of the model. Use of such a large number of node points in the r direction will increase the number of equations by a great deal and hence, we used a mixed order finite difference approach, wherein we use less number of node points with unequal node spacing. It is

to be noted that, the macroscopic battery model requires only the lithium concentration at the surface of the particle, $c_{surf}(x,t)$, as a function of local reaction current density, $j(t)$. For this reformulation method, the node points are chosen optimally. Derivation of finite difference notations for different approximation for the derivatives is given in the following section [97,101].

Taylor series expansions at $x = x+h_{i+1}$ and $x - h_i$ are written as

$$f\left(x+h_{i+1}\right)=f\left(x\right)+\left(\frac{d}{dx}f\left(x\right)\right)h_{i+1}+\frac{1}{2}\left(\frac{d^2}{dx^2}f\left(x\right)\right){h_{i+1}}^2 \tag{4.8}$$

$$f\left(x-h_i\right)=f\left(x\right)-\left(\frac{d}{dx}f\left(x\right)\right)h_i+\frac{1}{2}\left(\frac{d^2}{dx^2}f\left(x\right)\right)h_i^2 \tag{4.9}$$

where h_i is the unequal node spacing between i^{th} and $(i-1)^{th}$ nodes in the domain. Truncating the series expansion with the required amount of accuracy and solving for the first and second order derivatives, we can obtain central finite difference formulas for the first and second order derivatives. We use an order of h^2 accuracy for all of our approximations.

$$\left(\frac{dc}{dx}\right)_{central}=\frac{-c_{i+1}h_i^2+c_ih_i^2+{h_{i+1}}^2c_{i-1}-{h_{i+1}}^2c_i}{h_{i+1}\left(h_i+h_{i+1}\right)h_i} \tag{4.10}$$

$$\left(\frac{d^2c}{dx^2}\right)_{central}=2\frac{c_{i+1}h_i-c_ih_i+h_{i+1}c_{i-1}-h_{i+1}c_i}{h_{i+1}\left(h_i+h_{i+1}\right)h_i} \tag{4.11}$$

Similarly forward and backward finite differences relations for the derivatives can be obtained, and used for boundary conditions.

$$\left(\frac{dc}{dx}\right)_{forward} = -\frac{c_{i+2}h_{i+1}^{\ 2} - h_{i+1}^{\ 2}c_{i+1} - 2h_{i+1}h_{i+2}c_{i+1} + 2h_{i+1}h_{i+2}c_i - h_{i+2}^{\ 2}c_{i+1} + h_{i+2}^{\ 2}c_i}{h_{i+2}\left(h_{i+1}+h_{i+2}\right)h_{i+1}} \tag{4.12}$$

$$\left(\frac{dc}{dx}\right)_{backward} = \frac{c_{i-2}h_i^{\ 2} - h_i^{\ 2}c_{i-1} - 2h_ih_{i-1}c_{i-1} + 2h_ih_{i-1}c_i - h_{i-1}^{\ 2}c_{i-1} + h_{i-1}^{\ 2}c_i}{h_{i-1}\left(h_i+h_{i-1}\right)h_i} \tag{4.13}$$

Fig. 4-2 presents a general methodology for obtaining efficient reformulation/representation of the pressure induced solid-phase diffusion equations in the pseudo radial r dimension within the particle.

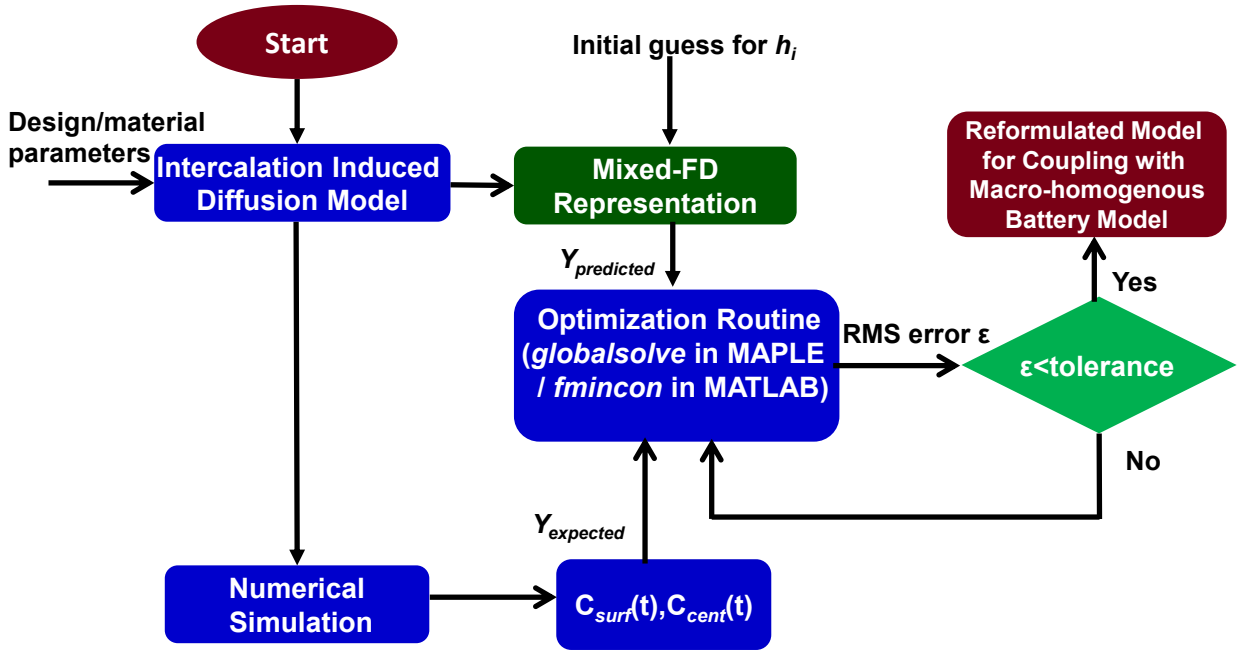

Fig. 4-2. Schematic of steps involved in mixed FD method for optimized node spacing and hence reformulation of pressure induced diffusion in solid-phase. $Y_{predicted}$ and $Y_{expected}$ are the values of the center and surface concentrations as predicted from full order numerical simulation and MFD simulation respectively

First, a Mixed-FD representation is written with $N = 5$ internal node points. For the optimization scheme, using $0.001 < h_i < 0.999$ as the constraint, the error between expected full-order numerical solution and the mixed-FD method is minimized to a set tolerance. At first, the

optimal node spacing for a lower rate of charge was found (by setting equal node spacing as initial guess). This is done because at low rates only geometry dictates the optimal node spacing (similar to primary current distribution in electrochemical systems). The optimal node spacing from low rates was used as initial guess to predict optimal node spacing for higher rates during which severe mass transfer limitations occur. The optimal node spacing obtained for higher rates was then used as initial guess to predict the best node spacing distribution for time dependent current which is reflective of spatially distributed and highly transient pore wall flux for macro-homogenous battery models. Mathematically, it can be represented as:

$$\begin{aligned} &\min_{h_i} E \\ &\text{subject to:} \\ &\frac{dy}{dt} = f(y,u,h_i) \\ &g(y,u,h_i) = 0 \\ &0.001 \le h_i \le 0.999 \end{aligned} \tag{4.14}$$

Here E is RMS error between full order numerical solution and the reformulated MFD solution, while y and u represent the differential and algebraic states in the model respectively. Numerous methods are available for solving constrained dynamic optimization problems, including (i) variational calculus, (ii) Pontryagin's maximum principle, (iii) control vector iteration, (iv) control vector parameterization, and (v) simultaneous nonlinear programming [62,102]. The control vector parameterization (CVP) [62] is a widely applied method employed in this study, due to its ease of implementation.. Typically, Jacobian based methods are sufficient for convergence [103]. For difficult/severe nonlinearities, global optimization techniques including genetic algorithms might be required for convergence and robustness [104,105] though they are likely to be very slow. For performing the multivariable optimization scheme discussed above, the inbuilt gradient based optimization algorithms in Maple's *GlobalSolve* function (Global

Optimization Toolbox) were used. Typically computational times for the simulation of optimization schemes range from minutes to hours.

One of the advantages of the MFD method is that, the radial concentration gradient is more significant near the surface compared to the center and hence, strategically placing more node points near the surface and less node points at the center can capture that behavior without increasing the fineness of the mesh everywhere. However, radial stress is maximum at the center of the particle and an optimization scheme is needed to allow for accurate prediction at the center of the particle (as opposed to arbitrarily using a finer mesh near the surface). Lesser node points in r leads to less state variables and equations and hence faster simulation for the whole battery model. The placement of these node points is important and in order to find the exact position of these node points we ran an optimization algorithm to find the best h_1, h_2, h_3, *etc.* and minimize N and the CPU time for efficient coupling with macro-homogenous models. This method is very accurate for short times/high rates/pulses; and is applicable for a wide range of operating conditions. Therefore this approach is very robust.

The model was then simulated with the optimally spaced node points using similar operating conditions and parameters which were used for full order numerical simulation using a DAE solver [53] with consistent initial values. We applied a mixed finite difference optimal node spacing approach for higher rates of galvanostatic charge and also for a time varying current case. For the mixed FD method we used 5 optimally placed internal node points in the pseudo dimension r within the particle and compared the results (dimensional surface concentration $c_{surf}(x,t)$) with full order numerical solution with 45 internal node points in r. To show the efficiency and accuracy of the optimally spaced node point method, we also compared surface concentration results for simulations with 5 equally spaced internal node points in r. We

chose high rates of charge, ranging from 2 to 10 C as the concentration gradient within the particle is more prominent for these cases. This makes it difficult to predict the surface concentration accurately with a small number of node points when not placed optimally. Figs. 4-3 to 4-6 show the comparisons between the above mentioned cases for 2, 3 5 and 10 C rates respectively.

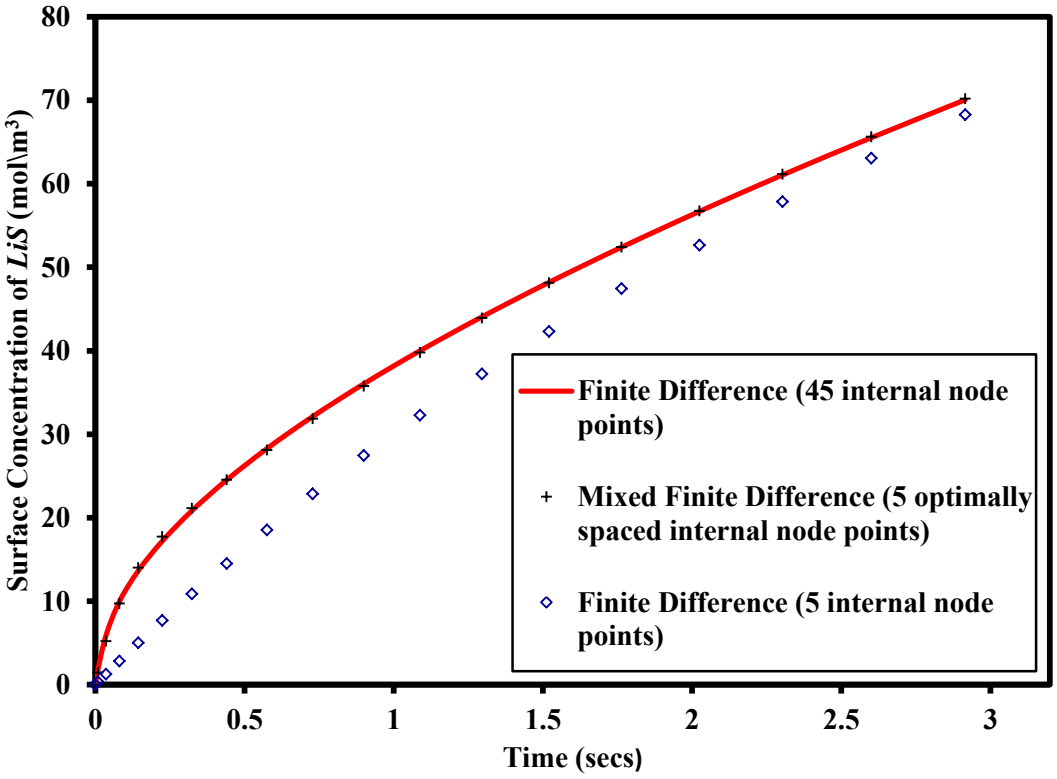

Fig. 4-3. Comparison of mixed finite difference method with 5 optimally placed internal node points with finite difference numerical solution with 45 and 5 equally spaced internal node points for a charging rate of 2C

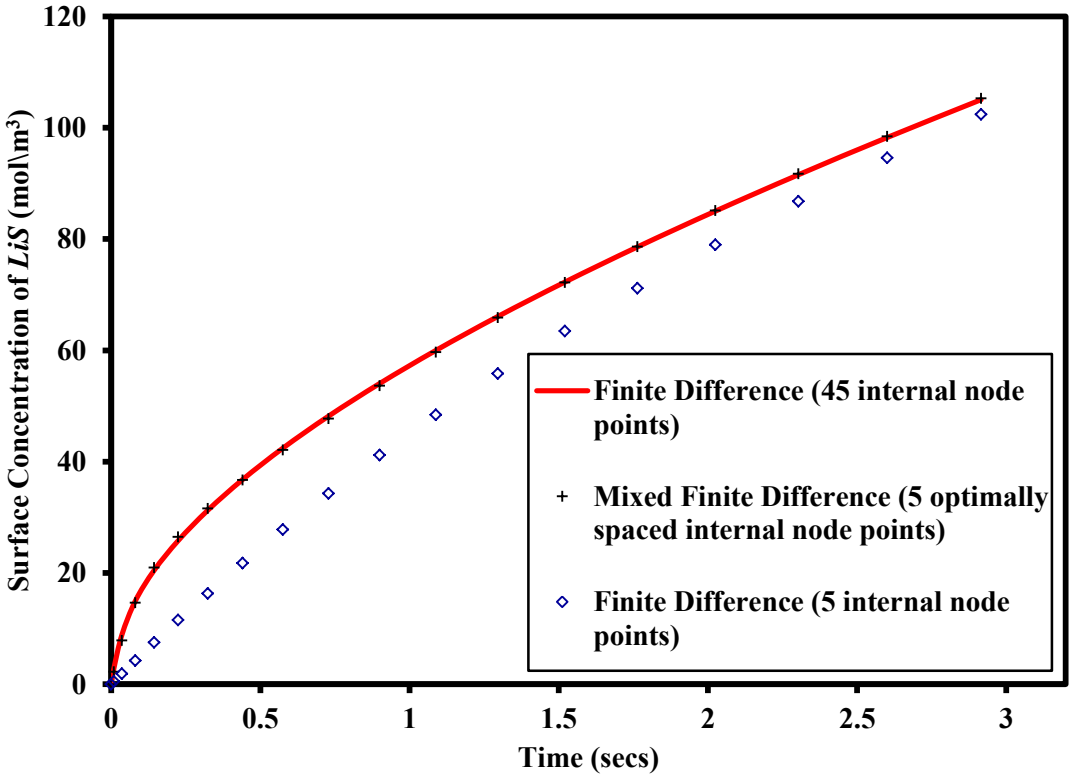

Fig. 4-4. Comparison of mixed finite difference method with 5 optimally placed internal node points with finite difference numerical solution with 45 and 5 equally spaced internal node points for a charging rate of 3C

It is to be noted that for all the plots, we compared $c_{surf}(x,t)$ for the first 2 to 3 seconds at the start of lithiation. This is because stress reaches maximum value within the first few seconds of lithiation and then decreases and finally equilibrates with time. The effect of pressure induced diffusion is thus most significant at short times [40]. This effect alters the concentration gradient within the particle significantly. Therefore, it is best to compare the results within that time frame because the efficiency and accuracy of the mixed FD model will be more visible compared to equally spaced node point simulation cases. However, the reformulated model is valid for the entire lithiation regime. From the plots it is clear that the MFD reformulated model agrees accurately with the full-order numerical solution. The results from the equal node spacing case

for low number of node points are clearly erroneous showing the importance and strategic benefits of placing the points optimally.

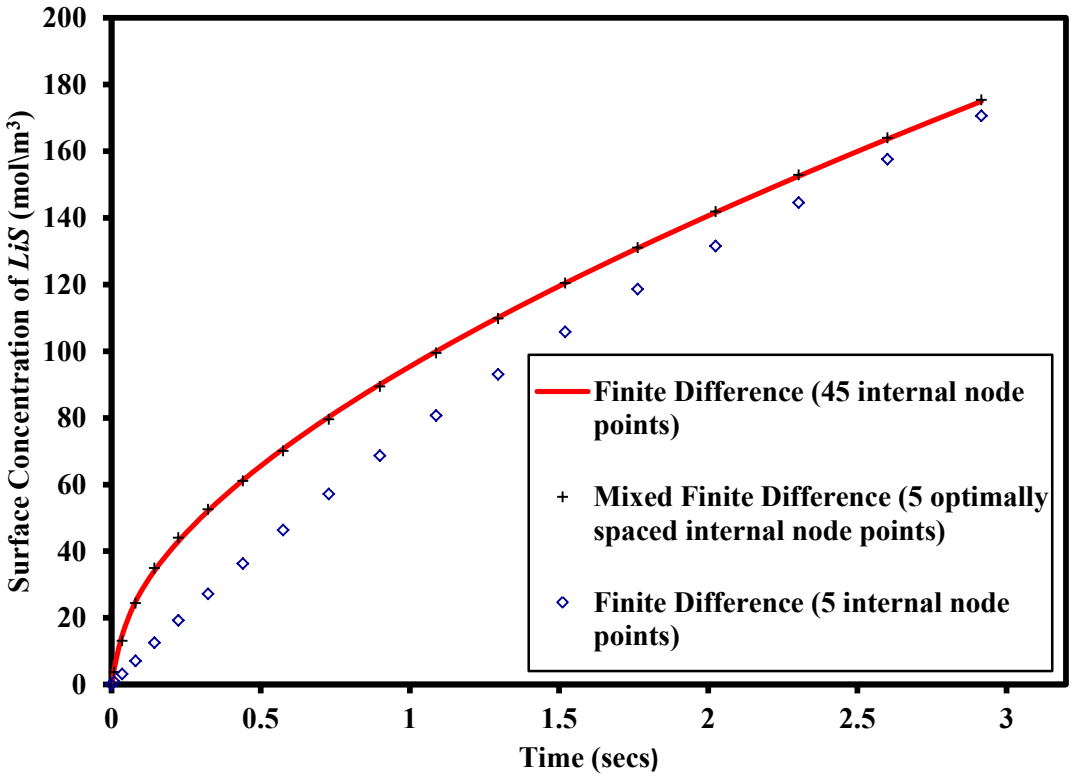

Fig. 4-5. Comparison of mixed finite difference method with 5 optimally placed internal node points with finite difference numerical solution with 45 and 5 equally spaced internal node points for a charging rate of 5C

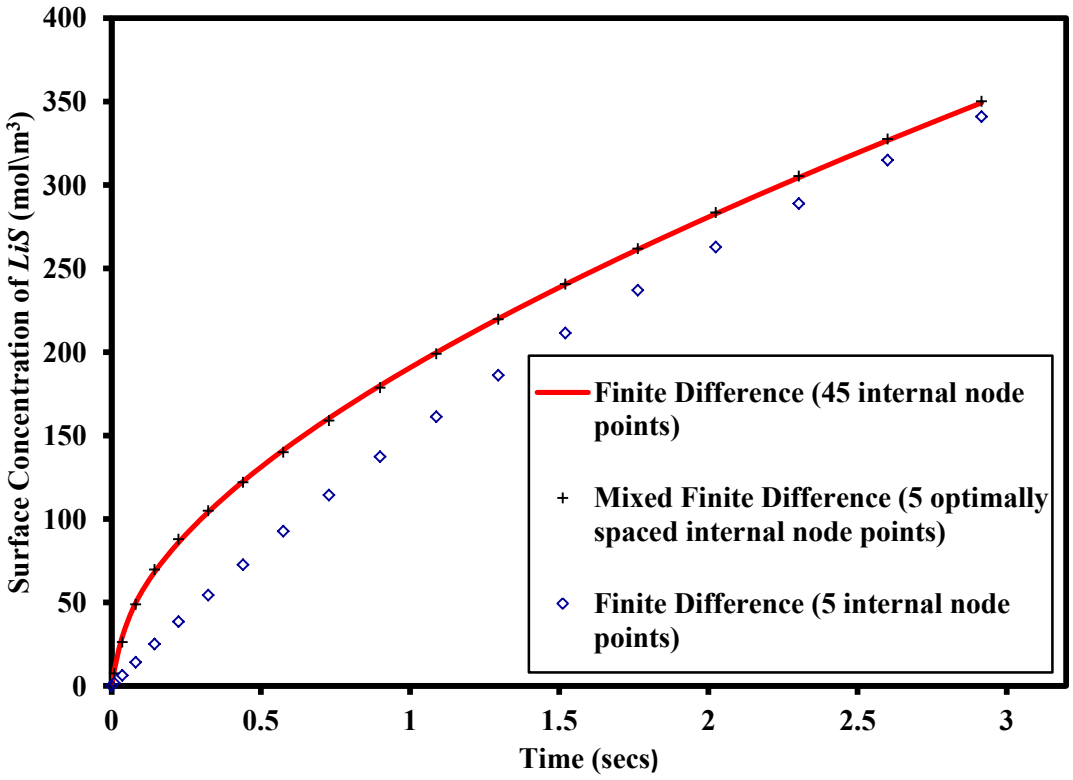

Fig. 4-6. Comparison of mixed finite difference method with 5 optimally placed internal node points with finite difference numerical solution with 45 and 5 equally spaced internal node points for a charging rate of 10C

Table 4-4 presents the values of optimized node spacing obtained in this case for different values of dimensionless current. As expected, the density of optimally placed node points increases along the radial direction *r* from the center to the surface following the direction of increment of concentration gradient within the particle.

C rate	Optimized node spacing (h_i)
2	[0.4764,0.1361,0.1699,0.1403,0.0525,0.0264]
3	[0.4762,0.1385,0.1675,0.1427,0.0505,0.0263]
5	[0.4780,0.1405,0.1629,0.1450,0.0491,0.0262]
10	[0.4779,0.1443,0.1582,0.1474,0.0478,0.0262]

Table 4-4. Optimized node spacing for different C rates for mixed finite difference reformulation method

The simulation times from the MFD method are compared with the times from full-order numerical solution with 45 internal node points in r in Table 4-5. The MFD method shows increased computational efficiency compared to full-order numerical solution as shown by the simulation times presented.

C rate	Simulation time for full-order numerical solution (s)	Simulation time for MFD reformulation (s)
2	1229.272	186.951
3	810.269	130.697
5	451.373	78.920
10	245.593	38.142

Table 4-5. Simulation times for different C rates for mixed finite difference reformulation method and full-order numerical solution with 45 equally spaced internal node points

The CPU times reported are based on simulations run on a computer using a 3.33 GHz Intel 12 core processor with 24 GB RAM . The compiled version of Maple is 10-20 times faster than the

non-compiled version. For larger number of equations, the compiled version of Maple is slower than a typical DASKR/IDA [53] call for the same number of equations as Maple does not use sparse storage methods for its DAE solvers. Nevertheless, it is clear that 1-2 orders of magnitude difference in CPU time is observed for the MFD reformulated model compared to the full-order model for the solid phase diffusion. Therefore, one can conclude that the reformulated MFD approach decreases the computational cost, and will play a key role in simulation efficiency when coupled with macroscopic battery models.

Fig. 4-7 shows the comparison of the mixed FD method, with the traditional finite difference (full-order) numerical solution with 45 and 5 equally spaced internal node points in r for dimensionless total current I varying with dimensionless time. The current applied is chosen as $I = 1 + \sin(100 * \tau)$. When the flux at the surface varies with time, then it is a real challenge to predict concentration profile accurately with less node points which is evident from the results obtained with 5 equally spaced internal nodes in r. The simulation was stopped when the surface mole fraction of LiS reached $x_{\max}$. From this figure it is clear that results obtained with the full-order numerical solution (45 equally spaced internal node points in r) can be efficiently obtained at reduced computational time with no compromise in accuracy with the mixed FD reformulated model. The optimal node spacing for the MFD simulation was [0.59, 0.15, 0.11, 0.1, 0.01, 0.02]. The simulation time taken is 8.908 seconds which is significantly less than that for the full-order numerical solution (103 seconds). This result shows the robustness of the MFD reformulation approach which can be confidently used for a large set of operating conditions.

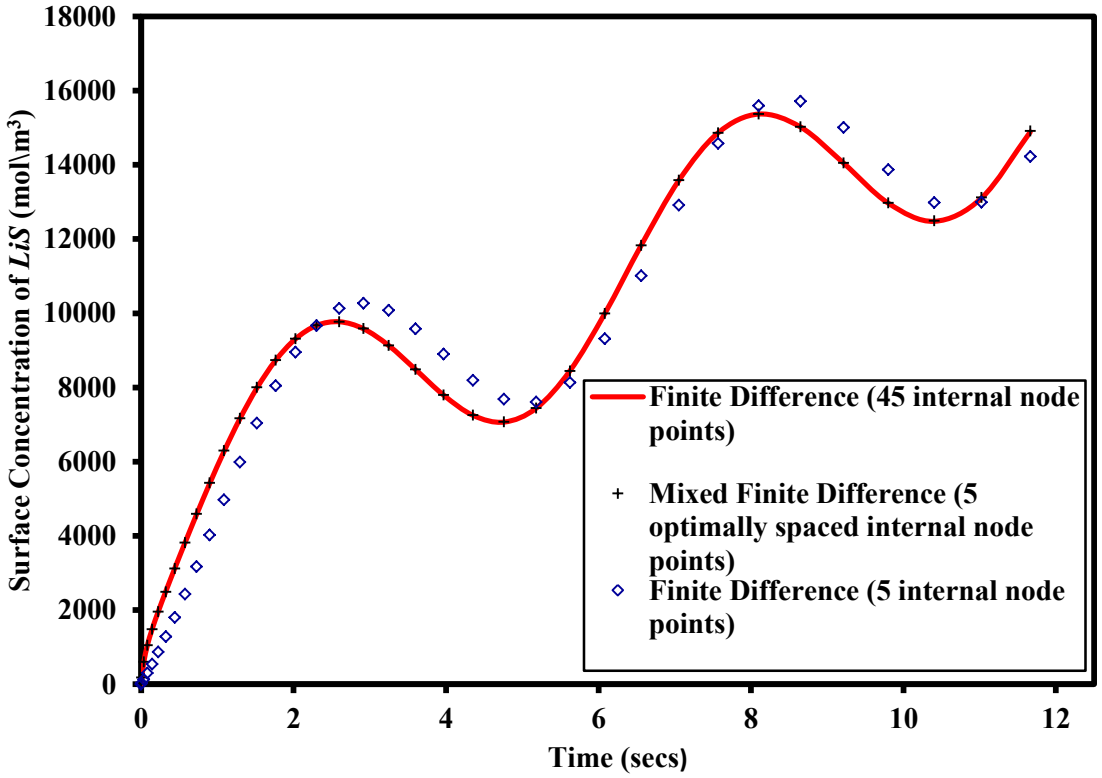

Fig. 4-7. Comparison of mixed finite difference method with 5 optimally placed internal node points with finite difference numerical solution with 45 and 5 equally spaced internal node points for current *I* varying as a function of time

For optimizing the node spacing h_i in the radial direction *r,* the error for the surface concentration $c_{surf}(x,t)$ of species *LiS* between the expected full-order numerical solution and the mixed-FD method was minimized to a set tolerance. But this approach compromises on the concentration profile at the center of the particle and therefore affects the radial stress profile at center [79]. As radial stress is maximum (tensile stress) at the center during charging, correct prediction of this quantity is important because the magnitude plays a critical role in determining the conditions for the fracture of the particle during lithium insertion. Moreover, for development of micro-macroscale electrochemical- mechanical coupled models for lithium ion batteries, the prediction of maximum radial stress becomes important. Therefore to achieve reasonable predictions for the

maximum stresses, the MFD method was modified such that the errors from both the center and surface *LiS* concentrations between expected full-order numerical solution and the mixed-FD method were minimized for optimization of node spacing . It is to be noted that unequal weights were applied to each of the individual errors and the sum of the weighted errors was assigned as the objective function to minimize with similar constraints used earlier for the optimization protocol. 5 internal node points were found to be sufficient for the model chosen. In our opinion, minimizing the error for center concentration can facilitate more accurate predictions for the maximum radial stress. Zhang et.al. [79] showed that with a slightly different and simpler stress strain modeling approach (strain splitting or thermal analogy modeling) without consideration of moving boundary and assuming constant density, both the radial and tangential stresses can be explicitly expressed as a function of average concentration and concentration at center and surface of particle. For our system, this relationship is not explicit but as both average (Faraday's law for charge conservation) and surface concentration are accurately predicted by MFD method, maximum tangential stress is always predicted accurately in the MFD approach irrespective of whether both center and surface concentrations or only surface concentration is considered for minimization of error. The maximum radial stress is more difficult to predict with approximate methods as the concentration moves towards the center. This drives our attempt to introduce the new weighted MFD method where errors for both the center and surface concentrations are minimized simultaneously.

Fig. 4-8 compares the results from the two MFD methods discussed and the full-order numerical solution with 45 internal node points in *r* for the surface concentration $c_{surf}(x,t)$ for 2C rate of charge.

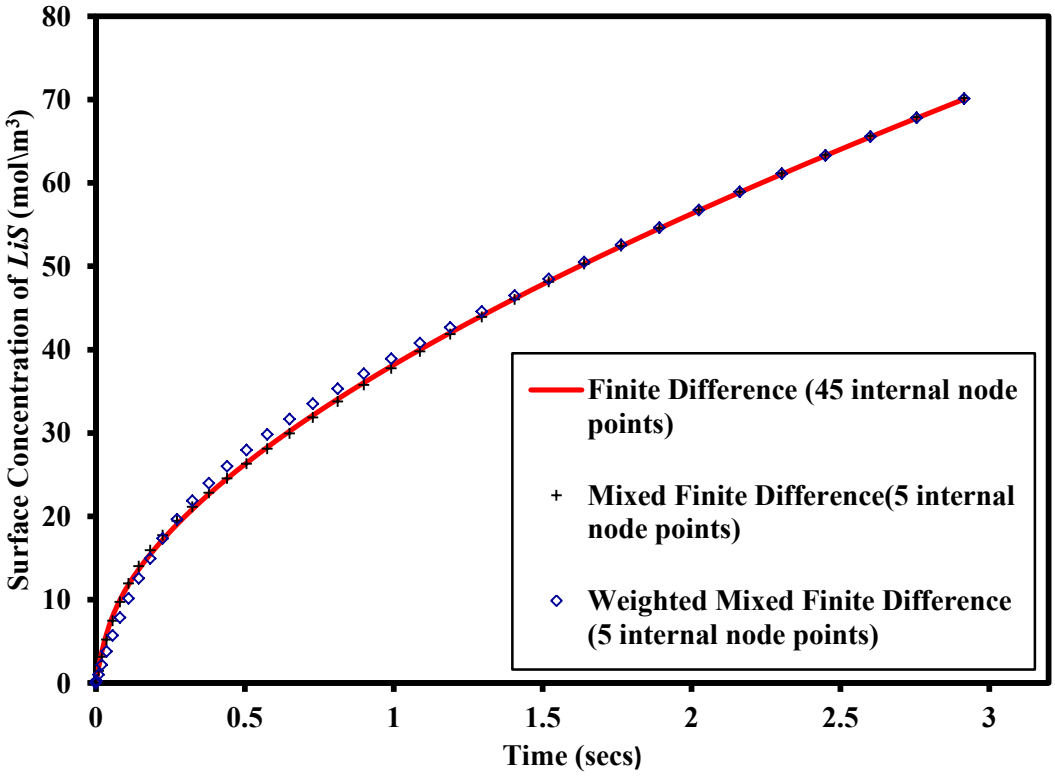

Fig. 4-8. Comparison of surface *LiS* concentration from the MFD reformulated models and full-order numerical simulation with 45 equally spaced internal node points for charging rate of 2C

It is clear from the plot, that the weighted error minimization MFD technique compromises on the surface concentration predictions slightly, especially at short times where the concentration profile has a steep gradient. The maximum radial stress profiles at the center of the particle for the MFD techniques are compared with the full-order numerical solution in Fig. 4-9 for 2C rate.

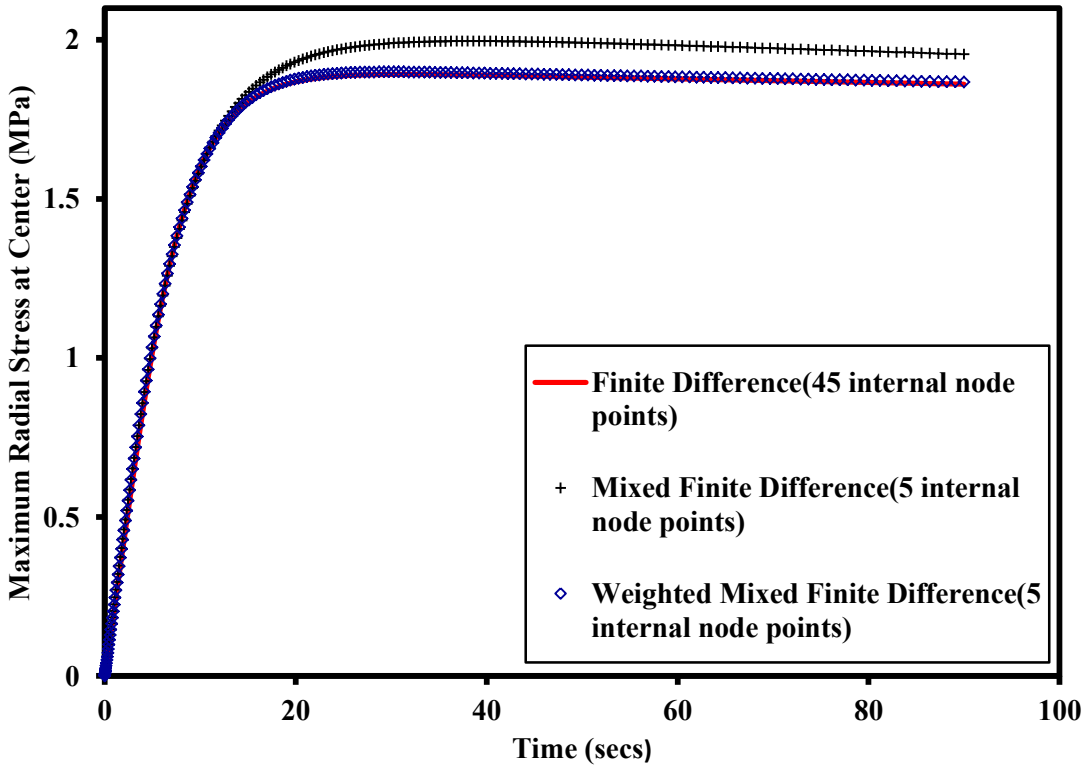

Fig. 4-9. Comparison of maximum radial stress from the MFD reformulated models and full-order numerical simulation with 45 equally spaced internal node points for charging rate of 2C

Simulation from the weighted error MFD method predicts the stress values with reasonable accuracy. But simulation results from the MFD method minimizing error for only the surface concentration, shows significant error compared to the full-order numerical solution. Fig. 4-10 shows the comparison of the maximum tangential stress profiles obtained from the two MFD methods with the full order numerical solution for 2C rate. As discussed earlier, both the MFD methods predict the maximum tangential stress at the surface with reasonable accuracy. The optimal node spacing obtained for the weighted error MFD method simulation was [0.41, 0.03, 0.28, 0.14, 0.10, 0.04].

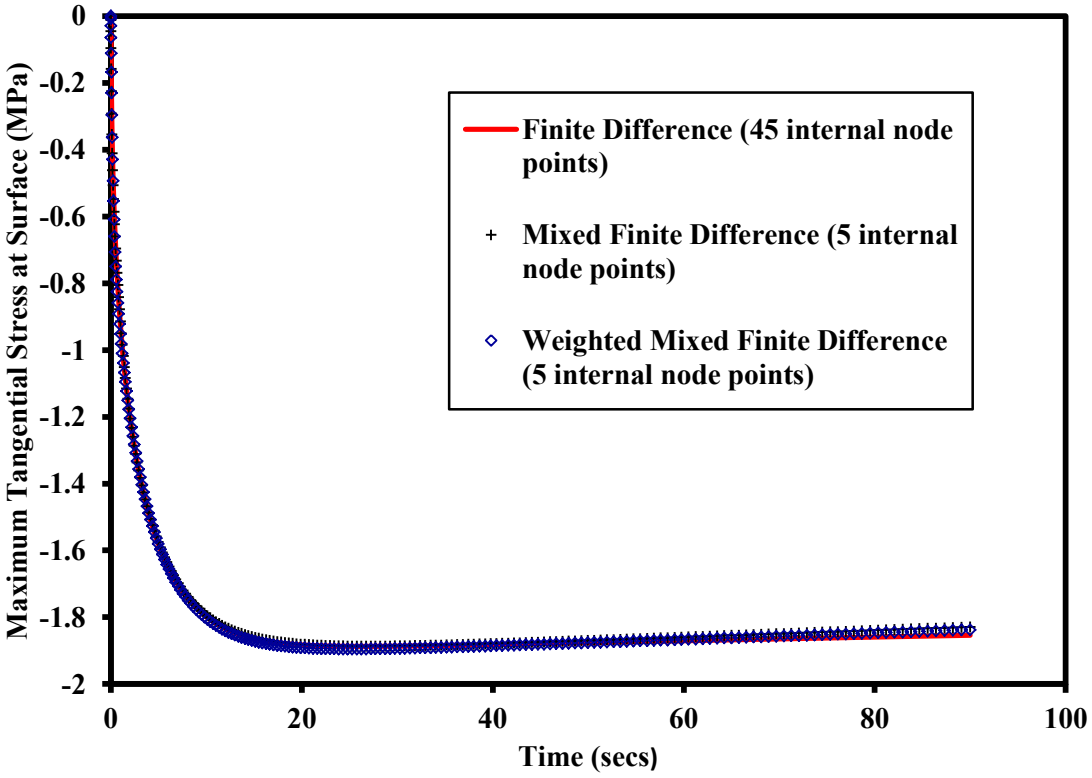

Fig. 4-10. Comparison of maximum tangential stress from the MFD reformulated models and full-order numerical simulation with 45 equally spaced internal node points for charging rate of 2C

Therefore, minimizing errors for both the center and surface concentrations simultaneously to optimize node spacing, leads to errors in the prediction of surface variables as seen from the results. It is to be noted that the weighted error MFD method is a case of multi-objective optimization and minimizing both errors with as low as 5 node points is difficult. This is the reason for which a small compromise in the surface concentration predictions is observed. In our opinion, using higher order finite difference discretization schemes (third or fourth order) or larger number of node points, this error can be remedied, but higher order approximations can induce instability in numerical simulation. As our final aim is to reduce computational cost, obtaining reasonably accurate predictions with minimum number of node points is our priority.

4.5 Generality of the proposed mixed finite difference approach

The results discussed from both the MFD approaches in the previous section were derived for isotropic graphite as the electrode particle material. At present, for high energy/power applications, novel materials like silicon are emerging as the suitable candidates for state-of-art electrodes. An attempt was made to verify the generality of the MFD approach by using the optimal node spacing obtained for graphite to predict the surface concentration and stress profiles for silicon. Simulations were performed for a spherical particle of silicon of 50 nm radius for a 1 C rate of charge. The optimal node spacing obtained from the weighted MFD method discussed earlier was used to predict the silicon profiles.

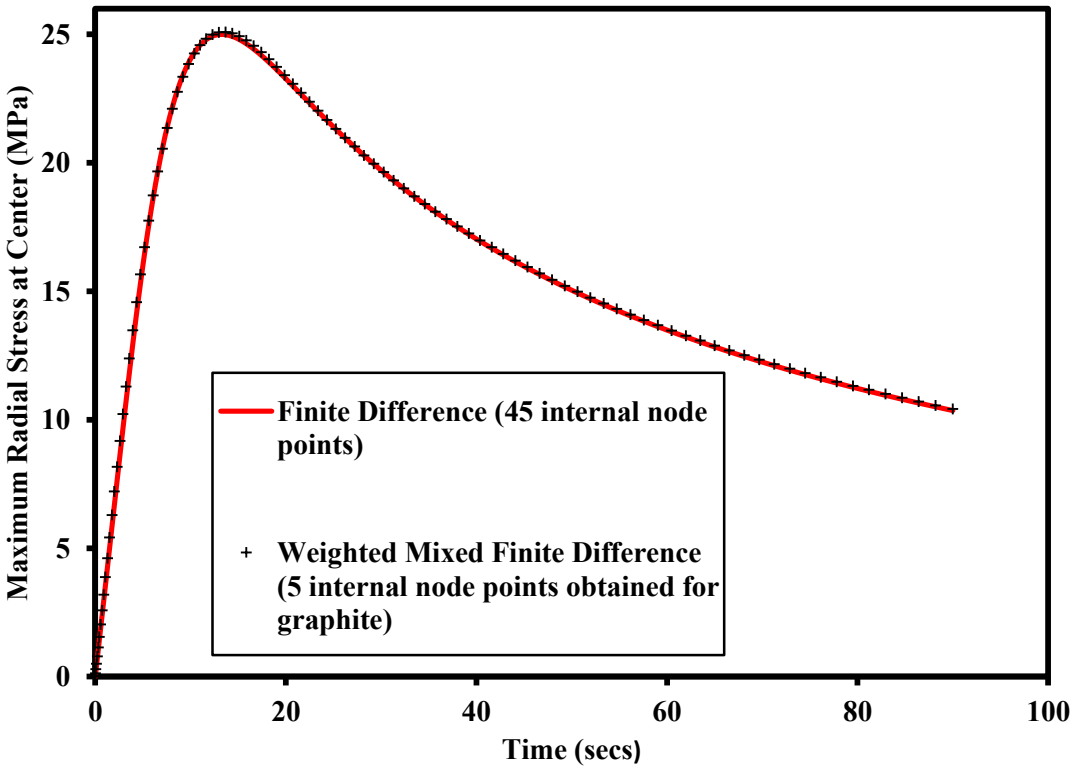

Fig. 4-11. Comparison of maximum radial stress from the weighted MFD reformulated models and full-order numerical simulation with 45 equally spaced internal node points for charging rate of 1C for silicon using optimal node spacing derived for graphite

Fig. 4-11 and 4-12 show the comparison of the maximum radial and tangential stress profiles predicted by the weighted MFD approach with the full order numerical solution. It is evident from the plots that the MFD simulation using optimal node spacing corresponding to graphite predicts the stress profiles with reasonable accuracy for silicon. Although it is advisable to derive a separate set of optimal node spacing for a specific material, this study proves the generality and robustness of the proposed MFD approach.

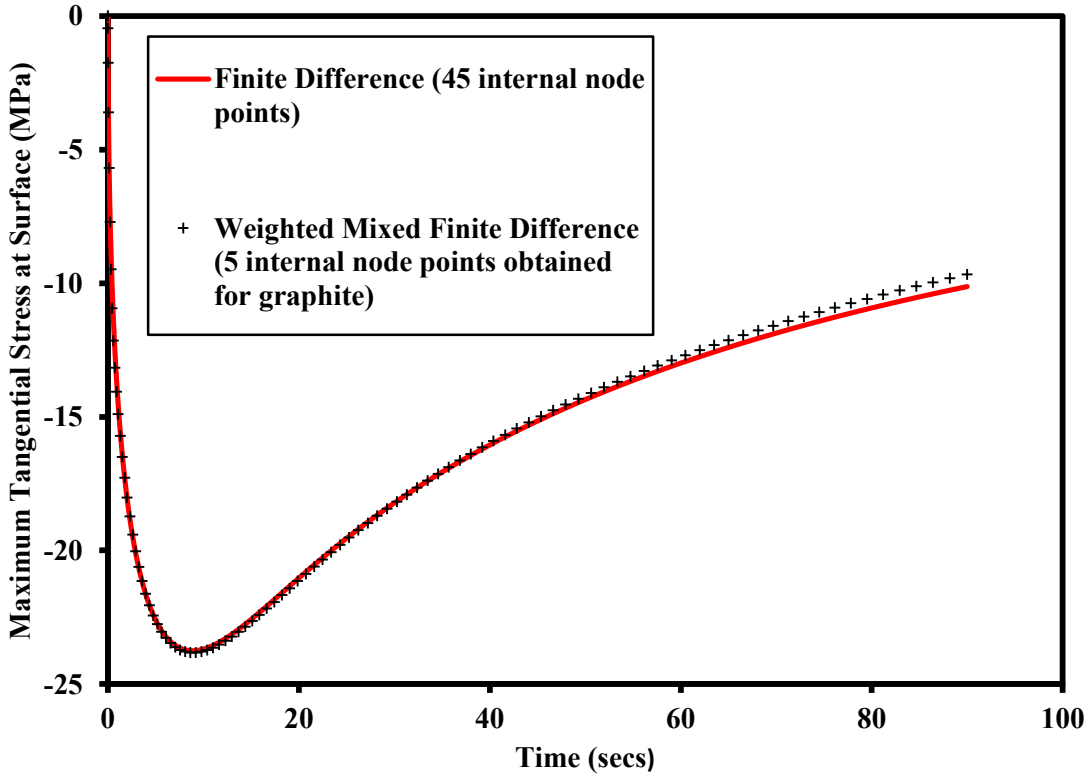

Fig. 4-12. Comparison of maximum tangential stress from the weighted MFD reformulated models and full-order numerical simulation with 45 equally spaced internal node points for charging rate of 1C for silicon using optimal node spacing derived for graphite

List of symbols

$r =$ dimensional radial distance within the particle (m)

$t =$ dimensional time (secs)

$\xi =$ dimensionless radial distance within the particle

$\tau =$ dimensionless time

$x_{LiS}(\xi,\tau) =$ dimensionless mole fraction of species LiS

$u(\xi,\tau) =$ dimensionless lattice displacement

$N_{LiS}(\xi,\tau) =$ dimensionless flux of species LiS

$N_S(\xi,\tau) =$ dimensionless flux of species S

$\theta(\xi,\tau) =$ dimensionless total concentration of binary species

$\sigma_r(\xi,\tau) =$ dimensionless radial stress

$\sigma_t(\xi,\tau) =$ dimensionless tangential stress

$\pi(\xi,\tau) =$ dimensionless pressure

$\chi(\tau) =$ dimensionless time varying particle radius

$\omega =$ fractional expansivity

$M_b =$ dimensionless molar mass ratio of binary species $= \dfrac{M_{LiS}}{M_S}$

$M_i =$ molar mass of species $i,\ i = LiS, S$

$x_{\max} =$ maximum mole fraction for lithiation

$e =$ dimensionless elastic modulus $= \dfrac{EM_S}{\rho_s^{\,0} RT(1+\nu)(1-2\nu)}$

$E =$ Young's modulus

$\nu =$ Poisson's ratio

$R =$ universal gas constant

$T =$ temperature

$\rho_s^{\,0} =$ density of pure unlithiated host

$D =$ dimensionless ratio of diffusive to elastic energy $= \dfrac{D_{LiS,S}\rho_s^{\,0}(1+\nu)(1-2\nu)}{R_0^{\,2}E}$

$D_{LiS,S} =$ binary diffusion coefficient

$R_0 =$ initial particle radius

$I =$ dimensionless current $= \dfrac{I_p M_S}{4\pi R_0 F D_{LiS,S}\rho_s^{\,0}}$

$I_p =$ applied current

$F =$ Faraday constant

$N =$ number of internal node points

$N_{\text{var}} =$ number of variables in system

$\overline{N}_{LiS}(\xi,\tau) =$ dimensionless volume averaged flux of LiS

$c_{surf}(x,t) =$ dimensional surface concentration of LiS (mol/m^3)

$j(t) =$ dimensional local reaction current density (A/m^2)

$h_i =$ optimal node spacing in radial direction

$LiS =$ host material occupied with lithium

$S =$ pure host material

Chapter 5

Conclusions and future directives

5.1 Conclusions from optimization of design variables

Smart and efficient design of lithium ion batteries is desired to achieve enhanced performance and operational safety for use in advanced high power/energy devices of future. Motivated by the achievement of this goal, simultaneous multi-parameter optimization of battery design parameters using a physics-based porous electrode theory model was implemented for the efficient design of porous electrodes that are commonly used in advanced secondary batteries. Use of an orthogonal collocation-based reformulated model with increased computational efficiency facilitated the implementation. The results indicate that the simultaneous optimization of electrode design parameters can result in a significant improvement in energy drawn from a battery. This study can be extended to the optimal design of state-of-the-art batteries for minimizing the temperature gradient across a cell for safe operation and prevention of thermal runaway. The adopted approach has applications in better design of batteries that can meet energy and power requirements for emerging applications in vehicles, satellites, and in the military. This procedure can also be extended to optimize other objectives such as maximizing the available discharge capacity given size constraints, rather than time constraints.

The analysis is based on a pseudo 2D macro-homogeneous model. Recent advances in the literature include multiscale models. Optimization based on those models will give results that will increase the utility of the proposed approach. However, note that as of today, dependency on having a fit for open circuit potential limits the applications of these new multi-scale models.

5.2. Conclusions from stress modeling for Si anodes for lithium-ion batteries

Stress development is a major factor behind capacity fade for lithium ion batteries as it causes fracture and loss of active materials in electrodes specially for high energy capacity materials like silicon, germanium etc. Therefore detailed fundamental study of stress development in electrodes as a result of lithium intercalation is required to understand and resolve the existing issues. This is the motivation behind this particular study.

A 2-d transient numerical model to simulate the stress development due to electrochemical lithiation of Si NW was developed. The model predicts non-uniform volumetric strain along the length of the Si NW, with regions of maximum expansion at the top of the Si NW and almost no expansion close to the Cu CC interface. Results indicate that the magnitude of the stress components are very high at the Si NW/Cu CC interface, compared to the stresses developed far away from the interface. The stress evolution with time is strongly dependent on the relative magnitudes of chemical and the pressure diffusion fluxes. The maximum stresses occur during the time when the flux is dominated by the chemical diffusion term, i.e. ~ 1 - 10 s for the rates and radius chosen for the simulations. Increase in radius of the nanowire and increase in lithiation rates develop larger radial and tangential stresses. Further, the peak maximum stresses occur at shorter times with increase in lithiation rates, while it occurs at longer times with increase in the radius of the nanowire.

5.3 Conclusions from solid phase reformulation of pressure induced diffusion

Use of lithium-ion batteries is increasing for various applications including high power/energy demanding applications. For ensuring safety during operation and better cycle life, smarter control of such systems is required. Real time control requires efficient simulation of lithium ion battery models in real time. This particular requirement motivated the development of two efficient reformulation techniques for pressure induced solid phase diffusion within a lithium ion battery active material particle. The parabolic profile reformulation method was developed based on assuming parabolic profiles for dependent variables in the radial dimension r within the particle and generating volume averaged equations. The mixed finite difference reformulation approach is based on using lesser number of optimally spaced node points in radial dimension r within the particle. Both of the methods reduce the number of states compared to full-order numerical solution using large number of node points and therefore reduce computational cost/time. The parabolic profile reformulation method is accurate for low rates and long times. The mixed finite difference approach is an accurate and robust method for low/high rates, short/long times and can be used with confidence for a wide range of operating conditions. Moreover, the generality of the MFD approach was shown when the node spacing obtained for graphite was used for predicting silicon stress profiles with reasonable accuracy. The effect of reformulated models will be most significant when they are coupled with the macroscopic battery models

5.4. Future directives

Lithium ion batteries are being extensively used for products ranging from consumer electronics to electric vehicles. The demand is increasing and to ensure operational safety, reduced costs and

increased cycle life, better design and improving control strategies during operation are the key tools. Therefore model based fundamental and applied studies for lithium ion batteries are very important to achieve these final goals. Target of achieving these goals influenced the modeling and simulation problems tackled in the thesis.

The design of battery architecture presented in the thesis can be further enriched and made more usable for industrial implementation by including other parameters like particle radius, separator thickness etc. for optimization. Moreover, thermal and stress-strain (solid mechanics) physics can be added to the model used for optimization purpose which can lead to better and more meaningful results. A two dimensional model can be also implemented which would take in to account the tab and current collector dimensions and use them as additional optimization parameters.

Concentration dependent diffusion coefficient, phase transitions between amorphous and crystalline silicon, non-ideality of solution, plastic deformation are some of the parameters and physics neglected during development of the 2 D model for studying stress development in Si nanowire. Including these in the models will improve the predictability and give us more insight into the phenomena occurring. The model can be used to study other nanostructures like Si nanotubes, core-shell structures to determine the best structure with respect to minimum stress developed for use as anode in lithium ion battery. Other reformulation techniques can be used and implemented for solid phase pressure induced diffusion within the active material particle. As finite difference based methods are not inherently conserving by nature, exploring finite volume based methods are important. Moreover, coupling of this particle level reformulated model with the macro-homogenous model [10] and reformulated models [36,37] will be beneficial for real time control and optimization purposes [38] for batteries.

These set of fundamental and applied studies are important for better control and utilization of batteries. The results from these studies can lead to the development of a new battery management system based on very fast models capable of predicting states in batteries accurately and efficiently and respond with quick control decisions.

References

[1] T. Nguyen, R. Savinell, in: The Electrochemical Society Interface, The Electrochemical Society, New Jersey, USA, 2010, pp. 54-56.

[2] B. Dunn, H. Kamath, J.-M. Tarascon, in: Science, 2011, pp. 928-935.

[3] J. Newman, K.E. Thomas, H. Hafezi, D.R. Wheeler, J. Power Sources, 119 (2003) 838-843.

[4] V. Ramadesigan, P.W. Northrop, S. De, S. Santhanagopalan, R.D. Braatz, V.R. Subramanian, J. Electrochem. Soc., 159 (2012) R31-R45.

[5] D. Zhang, B.N. Popov, R.E. White, J. Electrochem. Soc., 147 (2000) 831-838.

[6] M. Doyle, J. Newman, Electrochim. Acta, 40 (1995) 2191-2196.

[7] M. Doyle, J. Newman, J. Power Sources, 54 (1995) 46-51.

[8] J. Newman, J. Electrochem. Soc., 142 (1995) 97-101.

[9] V. Ramadesigan, R.N. Methekar, F. Latinwo, R.D. Braatz, V.R. Subramanian, J. Electrochem. Soc., 157 (2010) A1328-A1334.

[10] M. Doyle, T.F. Fuller, J. Newman, J. Electrochem. Soc., 140 (1993) 1526-1533.

[11] S. Al Hallaj, H. Maleki, J.S. Hong, J.R. Selman, J. Power Sources, 83 (1999) 1-8.

[12] D. Bernardi, E. Pawlikowski, J. Newman, J. Electrochem. Soc., 132 (1985) 5-12.

[13] Y. Chen, J.W. Evans, J. Electrochem. Soc., 140 (1993) 1833-1838.

[14] Y.F. Chen, J.W. Evans, J. Electrochem. Soc., 141 (1994) 2947-2955.

[15] T.I. Evans, R.E. White, J. Electrochem. Soc., 136 (1989) 2145-2152.

[16] W.B. Gu, C.Y. Wang, in: S. Surampudi, R.A. Marsh, Z. Ogumi, J. Prakash (Eds.) Lithium Batteries, The Electrochemical Society Proceedings Series, Pennington, NJ, 2000, pp. 748.

[17] V. Srinivasan, C.Y. Wang, J. Electrochem. Soc., 150 (2003) A98-A106.

[18] J. Newman, W. Tiedemann, J. Electrochem. Soc., 142 (1995) 1054-1057.

[19] S.C. Chen, C.C. Wan, Y.Y. Wang, J. Power Sources, 140 (2005) 111-124.

[20] J. Lee, K.W. Choi, N.P. Yao, C.C. Christianson, J. Electrochem. Soc., 133 (1986) 1286-1291.

[21] G.-H. Kim, K. Smith, ECS Meeting Abstracts, 802 (2008) 1295.

[22] R.E. Gerver, in: Mechanical Engineering, The University of Texas at Austin, Austin, TX, 2009.

[23] J.P. Meyers, M. Doyle, R.M. Darling, J. Newman, J. Electrochem. Soc., 147 (2000) 2930-2940.

[24] D.E. Stephenson, E.M. Hartman, J.N. Harb, D.R. Wheeler, J. Electrochem. Soc., 154 (2007) A1146-A1155.

[25] T.O. Drews, E.G. Webb, D.L. Ma, J. Alameda, R.D. Braatz, R.C. Alkire, AIChE J., 50 (2004) 226-240.

[26] A. Van der Ven, G. Ceder, Electrochem. Solid St., 3 (2000) 301-304.

[27] J. Bhattacharya, A. Van der Ven, Phys. Rev. B, 81 (2010) 104304.

[28] R.N. Methekar, P.W.C. Northrop, K.J. Chen, R.D. Braatz, V.R. Subramanian, J. Electrochem. Soc., 158 (2011) A363-A370.

[29] K. Leung, J.L. Budzien, Phys. Chem. Chem. Phys., 12 (2010) 6583-6586.

[30] W.Q. Li, S.H. Garofalini, Solid State Ionics, 166 (2004) 365-373.

[31] Y. Qi, H. Guo, L.G. Hector, A. Timmons, J. Electrochem. Soc., 157 (2010) A558-A566.

[32] K. Tasaki, K. Kanda, S. Nakamura, M. Ue, J. Electrochem. Soc., 150 (2003) A1628-A1636.

[33] A. Varma, M. Morbidelli, Mathematical Methods in Chemical Engineering, Oxford Univ. Press, New York, NY [u.a.], 1997.

[34] V.R. Subramanian, V.D. Diwakar, D. Tapriyal, J. Electrochem. Soc., 152 (2005) A2002-A2008.

[35] L. Cai, R.E. White, J. Electrochem. Soc., 156 (2009) A154-A161.

[36] V.R. Subramanian, V. Boovaragavan, V. Ramadesigan, M. Arabandi, J. Electrochem. Soc., 156 (2009) A260-A271.

[37] P.W.C. Northrop, V. Ramadesigan, S. De, V.R. Subramanian, J. Electrochem. Soc., 158 (2011) A1461-A1477.

[38] S. De, P.W.C. Northrop, V. Ramadesigan, V.R. Subramanian, J. Power Sources, 227 (2013) 161-170.

[39] P. Arora, R.E. White, M. Doyle, J. Electrochem. Soc., 145 (1998) 3647-3667.

[40] J. Christensen, J. Newman, J. Solid State Electrochem., 10 (2006) 293-319.

[41] C.M. Doyle, in: Dept. Chem. Eng., University of California, Berkeley, CA, 1995.

[42] V. Srinivasan, J. Newman, J. Electrochem. Soc., 151 (2004) A1530-A1538.

[43] J. Christensen, V. Srinivasan, J. Newman, J. Electrochem. Soc., 153 (2006) A560-A565.

[44] S. Stewart, P. Albertus, V. Srinivasan, I. Plitz, N. Pereira, G. Amatucci, J. Newman, J. Electrochem. Soc., 155 (2008) A253-A261.

[45] T.F. Fuller, M. Doyle, J. Newman, J. Electrochem. Soc., 141 (1994) 982-990.

[46] T.F. Fuller, M. Doyle, J. Newman, J. Electrochem. Soc., 141 (1994) 1-10.

[47] M. Doyle, J. Newman, A.S. Gozdz, C.N. Schmutz, J.M. Tarascon, J. Electrochem. Soc., 143 (1996) 1890-1903.

[48] K.E. Thomas, J. Newman, J. Electrochem. Soc., 150 (2003) A176-A192.

[49] P. Arora, M. Doyle, A.S. Gozdz, R.E. White, J. Newman, J. Power Sources, 88 (2000) 219-231.

[50] P. Ramadass, B. Haran, R. White, B.N. Popov, J. Power Sources, 123 (2003) 230-240.

[51] P. Ramadass, B. Haran, P.M. Gomadam, R. White, B.N. Popov, J. Electrochem. Soc., 151 (2004) A196-A203.

[52] G. Ning, R.E. White, B.N. Popov, Electrochim. Acta, 51 (2006) 2012-2022.

[53] G.G. Botte, V.R. Subramanian, R.E. White, Electrochim. Acta, 45 (2000) 2595-2609.

[54] P.M. Gomadam, J.W. Weidner, R.A. Dougal, R.E. White, J. Power Sources, 110 (2002) 267-284.

[55] S. Santhanagopalan, Q. Guo, P. Ramadass, R.E. White, J. Power Sources, 156 (2006) 620-628.

[56] J. Newman, W. Tiedemann, AIChE J., 21 (1975) 25-41.

[57] G.L. Plett, J. Power Sources, 134 (2004) 252-261.

[58] G.L. Plett, J. Power Sources, 134 (2004) 262-276.

[59] J.C. Forman, S. Bashash, J.L. Stein, H.K. Fathy, J. Electrochem. Soc., 158 (2011) A93-A101.

[60] S. Golmon, K. Maute, M.L. Dunn, ECS Meeting Abstracts, 1101 (2011) 513.

[61] W. Du, N. Xue, A. Gupta, A.M. Sastry, J.R. Martins, W. Shyy, Acta Mech. Sinica, 29 (2013) 335-347.

[62] S. Kameswaran, L.T. Biegler, Comput. Chem. Eng., 30 (2006) 1560-1575.

[63] A. Mitsos, B. Chachuat, P.I. Barton, J. Global Optimization, 45 (2009) 63-93.

[64] R.N. Methekar, V. Ramadesigan, J.C. Pirkle Jr, V.R. Subramanian, Comput. Chem. Eng., 35 (2011) 2227-2234.

[65] V.L. Chevrier, J.R. Dahn, J. Electrochem. Soc., 156 (2009) A454-A458.

[66] L.Y. Beaulieu, K.W. Eberman, R.L. Turner, L.J. Krause, J.R. Dahna, Electrochem. Solid State Lett., 4 (2001) A137-A140.

[67] M.N. Obrovac, L. Christensen, Electrochem. Solid State Lett., 7 (2004) A93-A96.

[68] C.K. Chan, H. Peng, G. Liu, K. McIlwrath, X.F. Zhang, R.A. Huggins, Y. Cui, Nat. Nano, 3 (2008) 31-35.

[69] L.F. Cui, R. Ruffo, C.K. Chan, H. Peng, Y. Cui, Nano Lett., 9 (2009) 491-495.

[70] A. Magasinski, P. Dixon, B. Hertzberg, A. Kvit, J. Ayala, G. Yushin, Nat. Mater., 9 (2010) 353-358.

[71] G. Sikha, B.N. Popov, R.E. White, J. Electrochem. Soc., 151 (2004) A1104-A1114.

[72] K. Kumaresan, G. Sikha, R.E. White, J. Electrochem. Soc., 155 (2008) A164-A171.

[73] W.B. Gu, C.Y. Wang, J. Electrochem. Soc., 147 (2000) 2910-2922.

[74] S. Prussin, J. Appl. Phys., 32 (1961) 1876-1881.

[75] C. Wang, X. Cheng, A.M. Sastry, S.B. Choi, J. Eng. Mater. Technol.-Trans. ASME, 121 (1999) 503-513.

[76] W.L. Wang, S. Lee, J.R. Chen, J. Appl. Phys., 91 (2002) 9584-9590.

[77] S. Lee, W.L. Wang, J.R. Chen, Mater. Chem. Phys., 64 (2000) 123-130.

[78] S.C. Ko, C.T. Hu, Y.T. Chou, Comput. Mater. Contin., 28 (2012) 165-179.

[79] X. Zhang, W. Shyy, A.M. Sastry, J. Electrochem. Soc., 154 (2007) A910-A916.

[80] M.W. Verbrugge, Y.T. Cheng, J. Electrochem. Soc., 156 (2009) A927-A937.

[81] Y.T. Cheng, M.W. Verbrugge, J. Power Sources, 190 (2009) 453-460.

[82] S. Renganathan, G. Sikha, S. Santhanagopalan, R.E. White, J. Electrochem. Soc., 157 (2010) A155-A163.

[83] R. Deshpande, Y.T. Cheng, M.W. Verbrugge, J. Power Sources, 195 (2010) 5081-5088.

[84] R. Deshpande, Y.T. Cheng, M.W. Verbrugge, A. Timmons, J. Electrochem. Soc., 158 (2011) A718-A724.

[85] M. Zhu, J. Park, A.M. Sastry, J. Electrochem. Soc., 159 (2012) A492-A498.

[86] J. Christensen, J. Newman, J. Electrochem. Soc., 153 (2006) A1019-A1030.

[87] J. Christensen, J. Electrochem. Soc., 157 (2010) A366-A380.

[88] R. Chandrasekaran, A. Magasinski, G. Yushin, T.F. Fuller, J. Electrochem. Soc., 157 (2010) A1139-A1151.

[89] R. Chandrasekaran, T.F. Fuller, J. Electrochem. Soc., 158 (2011) A859-A871.

[90] Y.F. Gao, M. Zhou, J. Appl. Phys., 109 (2011) 014310.

[91] C.J. Wen, R.A. Huggins, J. Solid State Chem., 37 (1981) 271-278.

[92] M.N. Obrovac, L. Christensen, D.B. Le, J.R. Dahn, J. Electrochem. Soc., 154 (2007) A849-A855.

[93] P. Limthongkul, Y.I. Jang, N.J. Dudney, Y.M. Chiang, Acta Mater., 51 (2003) 1103-1113.

[94] D. Larcher, S. Beattie, M. Morcrette, K. Edström, J.C. Jumas, J.M. Tarascon, J. Mater. Chem., 17 (2007) 3759-3772.

[95] J.C. Slattery, Advanced Transport Phenomena, Cambridge Univ. Press, Cambridge [u.a.], 1999.

[96] V.R. Subramanian, J.A. Ritter, R.E. White, J. Electrochem. Soc., 148 (2001) E444-E449.

[97] V. Ramadesigan, V. Boovaragavan, J.C. Pirkle, V.R. Subramanian, J. Electrochem. Soc., 157 (2010) A854-A860.

[98] L.R. Petzold, S.L.V. Campbell, K.E. Brennan, Numerical Solution of Initial-Value Problems in Differential-Algebraic Equations, SIAM Press, Philadelphia, PA, 1996.

[99] C.Y. Wang, W.B. Gu, B.Y. Liaw, J. Electrochem. Soc., 145 (1998) 3407-3417.

[100] K. Jagannathan, J. Electrochem. Soc., 156 (2009) A1028-A1033.

[101] K. Smith, C.Y. Wang, J. Power Sources, 161 (2006) 628-639.

[102] L.T. Biegler, Chem. Eng. Process, 46 (2007) 1043-1053.

[103] Y. Bard, Nonlinear Parameter Estimation, Academic Press, New York, 1974.

[104] W.R. Esposito, C.A. Floudas, Ind. Eng. Chem. Res., 39 (2000) 1291-1310.

[105] A. Flores-Tlacuahuac, S.T. Moreno, L.T. Biegler, Ind. Eng. Chem. Res., 47 (2008) 2643-2655.